Energy level alignment mechanisms at inorganic-organic semiconductor interfaces investigated with photoelectron spectroscopy

Dissertation

Zur Erlangung des akademischen Grades
doctor rerum naturalium
(Dr. rer. nat.)
im Fach Physik
eingereicht an der

Mathematisch-Naturwissenschaftlichen Fakultät
der Humboldt-Universität zu Berlin
von

Herr M. Sc. Physik Thorsten Schultz

Präsident der Humboldt-Universität zu Berlin
Prof. Dr.-Ing. Sabine Kunst

Dekan der Mathematisch-Naturwissenschaftlichen Fakultät
Prof. Dr. Elmar Kulke

Gutachter:
1. Prof. Norbert Koch
2. Prof. Emil List-Kratovchil
3. Prof. Satoshi Kera

Tag der mündlichen Prüfung: 05.12.2018

Abstract

Hybrid inorganic/organic systems (HIOS) have attracted a lot of interest for fundamental studies and novel (opto)-electronic devices during the past decade. HIOS combine the outstanding electrical properties of inorganic materials with the flexibility of organic compounds. For developing efficient devices, an understanding and control of the energy level alignment (ELA) at the hybrid interface is of paramount importance. Nowadays a key technique for investigating ELA is photoelectron spectroscopy, which is also the main technique used in this work.

Firstly, it is demonstrated how surfaces with non-uniform local work function influence the measurement results obtained by ultraviolet photoelectron spectroscopy (UPS). As the dimensions of devices become smaller and smaller, it is essential to understand the influence of microscopic features on the results obtained by an often applied technique like UPS. For this purpose, model systems of linearly patterned substrates, having work function differences of more than 1 eV, are produced. Reference Kelvin-Probe force microscopy measurements are conducted, which quantify the local work function difference. By comparing the measured results with calculations, it is found that the electrostatic potential above the surface leads to an additional energy barrier for electrons above low work function areas, shifting the secondary electron cut-off (SECO) to higher kinetic energies in UPS (*averaging effect*). The influence of pattern size and measurement conditions (applied electric field) on the SECO is shown theoretically and experimentally. Furthermore, it is demonstrated that a heterogeneous substrate leads to an underestimation of the ionization energy of subsequently deposited molecules.

In the second part it is shown how thin organic donor/acceptor interlayers can be employed to manipulate the ELA between prototypical inorganic (GaN, Si) and organic (α-NPD) semiconductors. The work function of the inorganic substrate can be tuned between 2.2-6.0 eV and the hole injection barrier to α-NPD accordingly between <0.5 and 3.1 eV. The influence of gap states within the inorganic band gap on the band bending change upon molecular acceptor deposition is investigated in detail and a model is proposed, which describes the pinning of the inorganic energy levels as a function of surface state density. It is further shown experimentally, by investigating ZnO with different doping concentrations, that the bulk doping concentration of the inorganic semiconductor has only little effect on the energetic alignment.

Finally, the ELA of the transition metal dichalcogenide (TMDC) monolayer WSe_2 with the organic acceptor molecule $C_{60}F_{48}$ is investigated. TMDC monolayers are a novel class of materials with many interesting properties, like a direct band gap or a large spin-orbit splitting. Using STM and STS measurements, it is revealed that the $C_{60}F_{48}$ forms domains on WSe_2 in the sub-monolayer regime and that the energy levels of WSe_2 change tremendously between covered and uncovered areas. This goes along with results from UPS, where new features can be observed in the valence region, corresponding to covered WSe_2. These new features at lower binding energy and an increase in work function indicate the coexistence of undoped and p-doped regions in WSe_2 at sub-monolayer $C_{60}F_{48}$ coverages. By evaluating the potential change as a function of distance from a $C_{60}F_{48}$ edge in STS, it is possible to derive a value for the Thomas-Fermi screening length of WSe_2 of about 2 nm in this heterostructure. It is further demonstrated how the efficiency of a WSe_2 transistor is enhanced after p-doping with $C_{60}F_{48}$.

Keywords:

hybrid inorganic organic systems, energy-level alignment, interfaces, photoelectron spectroscopy, TMDCs

Zusammenfassung

Hybride anorganische/organische Systeme (HIOS) sind von großem Interesse für Grundlagenforschung und neue (opto)-elektronische Bauteile. Sie verbinden die herausragenden elektronischen Eigenschaften von anorganischen Halbleitern mit der Flexibilität von organischen Materialien. Um effiziente Bauteile zu entwickeln, ist ein Verständnis der Energielevelanordnung (ELA) an der Grenzfläche von entscheidender Bedeutung. Eine heutzutage häufig genutzte Technik zu deren Bestimmung ist die Photoelektronenspektroskopie, welche auch Hauptmethode dieser Arbeit ist.

Zuerst wird demonstriert, wie Oberflächen mit heterogener Austrittsarbeit die Resultate von ultravioletter Photoelektronenspektroskopie (UPS) beeinflussen. Da die Dimensionen von Bauteilen immer kleiner werden, ist es essentiell, die Auswirkungen mikroskopischer Merkmale auf eine makroskopische Messtechnik wie UPS zu verstehen. Dafür wurden Modellsysteme mit Streifenmustern und Austrittsarbeitsunterschieden von über 1 eV hergestellt. Als Referenzmessung wurde die Raster-Kelvin-Mikroskopie verwendet. Durch den Vergleich experimenteller Daten mit Berechnungen zeigt sich, dass das lokale elektrostatische Potential oberhalb der Oberfläche zur Ausbildung einer zusätzlichen Energiebarriere für Elektronen über Bereichen mit niedriger Austrittsarbeit führt, was die gemessene Sekundärelektronenkante zu höheren kinetischen Energien verschiebt. Der Einfluss von Streifengröße und experimentellen Parametern wird theoretisch und experimentell gezeigt. Weiterhin wird demonstriert, dass heterogene Substrate zu einer Unterschätzung der mit UPS gemessenen Ionisationsenergie von nachfolgend aufgedampften Molekülen führen.

Im zweiten Teil dieser Arbeit wird gezeigt, wie man dünne organische Donator/Akzeptor Zwischenschichten nutzen kann, um die ELA zwischen typischen anorganischen (GaN, Si) und organischen (α-NPD) Halbleitern zu kontrollieren. Die Austrittsarbeit von anorganischen Substraten lässt sich so zwischen 2.2-6.0 eV variieren. Dementsprechend kann man die Lochbarriere zwischen <0.5-3.1 eV einstellen. Der Einfluss von Zuständen in der Bandlücke des anorganischen Halbleiters auf die Bandverbiegung nach Abscheidung von organischen Akzeptoren wird im Detail untersucht und es wird ein Model vorgeschlagen, welches das Pinning des Fermi-Niveaus an diesen Zuständen beschreibt. Es wird weiterhin experimentell gezeigt, dass die Dotierung des anorganischen Halbleiters (ZnO) kaum Einfluss auf die ELA hat. Erst bei sehr hohen Dotierkonzentrationen nimmt die Bandverbiegungsänderung ab.

Im letzten Teil der Arbeit wird die ELA zwischen dem Übergangsmetall-Dichalcogenid (TMDC) WSe_2 und dem organischen Akzeptor $C_{60}F_{48}$ untersucht. TMDCs haben die besondere Eigenschaft, bei Reduzierung ihrer Dicke zu einer Monolage ihre Bandlücke von indirekt zu direkt zu ändern. Mit Hilfe von STM und STS Messungen wurde gezeigt, dass $C_{60}F_{48}$ geschlossene Domänen auf WSe_2 bei Bedeckung mit Submonolagen bildet und dass sich die Energielevel von WSe_2 nach der Bedeckung mit $C_{60}F_{48}$ drastisch ändern. Neue Peaks im Valenzspektrum (UPS), welche von mit $C_{60}F_{48}$ bedecktem WSe_2 stammen, bestätigen diese Beobachtungen. Die Peaks bei niedrigerer Bindungsenergie und eine Verschiebung der Sekundärelektronenkante zu höheren kinetischen Energien lassen auf die Präsenz von undotierten und p-dotieren Domänen schließen. Durch Auswerten der Potentialänderung als Funktion des Abstandes von einer $C_{60}F_{48}$ Kante im STS konnte die Thomas-Fermi-Abschirmlänge von WSe_2 in dieser Heterostruktur zu etwa 2 nm bestimmt

werden. Zusätzlich wurden die verbesserten Eigenschaften eines WSe_2 Transistors nach Dotierung mit $C_{60}F_{48}$ demonstriert.

Schlagwörter:

Hybride anorganische/organische Systeme, Energielevelanordnung, Grenzflächen, Photoelektronenspektroskopie, TMDCs

Contents

Abbreviations

HIOS	hybrid inorganic/organic systems
ELA	energy level alignment
UPS	ultraviolet photoelectron spectroscopy
SECO	secondary electron cut-off
TMDC	transition metal dichalcogenide
LCAO	linear combination of atomic orbital
DFT	density functional theory
HOMO	highest occupied molecular orbital
LUMO	lowest unoccupied molecular orbital
EA	electron affinity
IE	ionization energy
CBM	conduction band minimum
VBM	valence band maximum
PES	photoelectron spectroscopy
XPS	x-ray photoelectron spectroscopy
FWHM	full width at half maximum
AFM	atomic force microscopy
KPFM	Kelvin probe force microscopy
AM-KPFM	amplitude modulated KPFM
FM-KPFM	frequency modulated KPFM
STM/STS	Scanning Tunneling Microcopy / Spectroscopy
LEED	low energy electron diffraction
CSH	1-hexadecanethiol
FSH	1H,1H,2H,2H-perfluorodecanethiol
MOCVD	metal-organic chemical vapor deposition
SAM	self-assembled monolayer
DCD	differential charge density

Physical constants

symbol	name	value
e	elementary charge	$1.6021766208 \cdot 10^{-19}$ C
k_B	Boltzmann constant	$1.38064852 \cdot 10^{-23}$ J·K^{-1}
$\hbar$	reduced Planck constant	$1.054\ 571\ 8 \cdot 10^{-34}$ J·s
ε_0	vacuum permittivity	$8.854\ 187\ 817 \cdot 10^{-12}$ F·m^{-1}
m_0	electron mass	$9.109\ 383\ 56 \cdot 10^{-31}$ kg

1 Introduction

Since the first patent of the field-effect transistor by Lilienfeld in 1930 [1] and the production of the first working transistor by Shockley at Bell labs in 1947, inorganic semiconductors, like silicon and germanium, are the driving force in the development of opto-electronic devices. They still dominate the market due to their high mobilities and established ways to produce them with high purity. However, with the first organic field effect transistor produced by Koezuka *et al.* in 1987 [2], the interest in organic semiconductors as an alternative or supplementation to inorganic semiconductors has grown strongly. With their excellent light-matter coupling and the flexibility to adjust their properties by chemical synthesis almost at will, they already outperformed their inorganic counterpart in some areas, like display technology. Naturally, the idea emerged to combine both material classes in a hybrid manner, thereby pushing their advantages and compensating their individual drawbacks. Recently, devices with enhanced light emitting [3], gas sensing [4] and energy storing [5] properties based on hybrid device structures have been proposed and one promising class of materials for solar cell technology, hybrid perovskites [6], is based on a combination of inorganic and organic materials.

Whenever combining two or more materials in a device structure, no matter whether it is a solar cell or a light emitting diode, the energy levels at the interfaces play a major role for the functionality and efficiency of the final device. Therefore, knowing the energetic alignment between two materials and, even better, being able to predict them in advance, is indispensable for designing efficient device structures. A lot of work has been conducted during the last two decades to understand the energy level alignment between metals and organic semiconductors [7,8], as they are present at charge injection/extraction contacts in many devices. Effects like *interface dipole*, *pushback-effect* or *Fermi-level pinning* have been well-investigated in this context. Hybrid interfaces comprising of inorganic and organic semiconductors have also been studied recently, probably with the most extensive studies on zinc oxide [9]. The effect of *band bending* plays an important role for these kind of interfaces. An inorganic semiconductor with similar properties as zinc oxide, and therefore with equal potential application for hybrid devices, is gallium nitride. Yet another emerging class of interesting materials in the recent years are two dimensional inorganic semiconductors, especially transition metal dicalchogenides (TMDCs). Therefore this

thesis focuses on the energy level alignment between GaN, Si (3D), WSe_2 (2D) and small organic molecules.

One of the most frequently used techniques to study energetic properties at surfaces and interfaces is photoelectron spectroscopy. In combination with incremental deposition of organic molecules on inorganic substrates, this technique enables direct observation of the energetic developments at such hybrid interfaces. Although the interpretation of ultraviolet photoelectron spectroscopy data, e.g. to obtain the work function of a sample, is straightforward in the case of homogeneous surfaces, the signal interpretation for heterogeneous surfaces is more involved and barely investigated in literature. However, with the emergence of nanostructured devices (like quantum dots) a solid understanding of data interpretation of such an important technique is mandatory. Therefore this thesis is divided in the following way:

In chapter two, the fundamentals of inorganic and organic semiconductors are described along with the energy level alignment at several different classes of interfaces. The following chapter three describes the theoretical principles of the employed measurement techniques, namely photoelectron spectroscopy and scanning probe microscopy, and data evaluation procedures. In chapter four the experimental equipment and materials are described in detail. The results of this thesis are discussed in chapter five. The first section 5.1 investigates the influence of heterogeneous work function surfaces on the results obtained by UPS and the origin of multiple secondary electron cut-offs. The role of the electrostatic potential formed between the sample surface and the analyzer on the UPS results is evaluated with the help of Kelvin-probe force microscopy and theoretical calculations. Its impact on the determination of the ionization energy of subsequently deposited molecules is also investigated. Section 5.2 scrutinizes in detail the energy level alignment between bulk inorganic semiconductors (GaN, ZnO, Si) and strong organic acceptor molecules with focus on the influence of inorganic doping concentration and surface states density. Furthermore, the possible tuning of the energy level alignment between GaN, Si and α-NPD, a commonly used organic semiconductor, with the help of thin organic acceptor or donor interlayers is explored. In the last section 5.3 of this chapter the changes in energy levels of the 2D TMDC WSe_2 after deposition of the strong organic acceptor molecules $C_{60}F_{48}$ are investigated, using a combined approach of scanning tunneling microscopy/spectroscopy, density functional theory, photoelectron spectroscopy

and device characteristics. The Thomas-Fermi screening length of WSe_2, an important parameter for the design of devices, is obtained experimentally for the first time for such a system. The last part of this work, chapter six, closes with a summary and an outlook.

2 Fundamentals

2.1 Electronic Properties

2.1.1 Inorganic Semiconductors

Inorganic semiconductors form a band structure, which is the result of a periodic potential U, with $U(\boldsymbol{r}) = U(\boldsymbol{r} + \boldsymbol{R})$, created by the regular arrangement of the ion cores in a crystal lattice. Schrödinger's equation for an electron with mass m_0 in such a periodic potential is given by

$$H\Psi(\boldsymbol{r}) = \left(-\frac{\hbar^2}{2m_0}\nabla^2 + U(\boldsymbol{r})\right)\Psi(\boldsymbol{r}) = E\Psi(\boldsymbol{r}). \tag{1}$$

According to Bloch's theorem [10] all eigenstates Ψ of such a one-particle Hamiltonian can be written as a product of plane waves and a lattice-periodic function, the so-called Bloch function $u_{n\boldsymbol{k}}(\boldsymbol{r})$:

$$\Psi_{n\boldsymbol{k}}(\boldsymbol{r}) = Ae^{i\boldsymbol{k}\boldsymbol{r}}u_{n\boldsymbol{k}}(\boldsymbol{r}) \tag{2}$$

Here n is a quantum number and $\boldsymbol{k}$ is a wave vector. Under these conditions, the energy eigenvalues $E_n(\boldsymbol{k}) = E_n(\boldsymbol{k} + \boldsymbol{G})$ are periodic in reciprocal space, with $\boldsymbol{G}$ being a reciprocal lattice vector. There are several special cases for the potential U, like the free electron empty lattice approximation ($U \equiv 0$) [11] or the Kronig-Penney model [12]. Here the solution of a general wave equation for electrons in a periodic potential, based on [13,14], is presented.

A general periodic potential Ucan be represented as a Fourier series with reciprocal lattice vectors:

$$U(\boldsymbol{r}) = \sum_{\boldsymbol{G}} U_{\boldsymbol{G}}e^{i\boldsymbol{G}\boldsymbol{r}}. \tag{3}$$

The wave function Ψ can then be written as a Fourier series over all allowed Bloch wavevectors $\boldsymbol{K}$:

$$\Psi(\boldsymbol{r}) = \sum_{\boldsymbol{K}} C_{\boldsymbol{K}} e^{i\boldsymbol{K}\boldsymbol{r}}. \tag{4}$$

With this the kinetic and potential energies in the Schrödinger equation (1) become

$$\nabla^2\Psi = \sum_{\boldsymbol{K}} \boldsymbol{K}^2 C_{\boldsymbol{K}} e^{i\boldsymbol{K}\boldsymbol{r}}, \tag{5}$$

$$U\Psi = \sum_{\boldsymbol{G}} \sum_{\boldsymbol{K}\prime} U_{\boldsymbol{G}} C_{\boldsymbol{K}\prime-\boldsymbol{G}} e^{i\boldsymbol{K}\prime\boldsymbol{r}}, \tag{6}$$

with $\boldsymbol{K}' = \boldsymbol{K} + \boldsymbol{G}$. Schrödinger's equation can then be rewritten as a system of algebraic equations:

$$(\lambda_{\boldsymbol{K}} - E)C_{\boldsymbol{K}} + \sum_{\boldsymbol{G}} U_{\boldsymbol{G}} C_{\boldsymbol{K}-\boldsymbol{G}} = 0, \tag{7}$$

with $\lambda_{\boldsymbol{K}} = \hbar^2\boldsymbol{K}^2/(2m_0)$. To obtain approximated solutions at the zone boundaries one assumes that the potential energy has only non-vanishing Fourier coefficients U for the shortest reciprocal lattice vector $\boldsymbol{G}$ and that $U_{\boldsymbol{G}} = U_{-\boldsymbol{G}}$. As a result the one-dimensional potential has the form $U(x) = 2U\cos(Gx)$. In the vincinity of $\boldsymbol{K} = \boldsymbol{G}/2$ the kinetic energy is the same for $\boldsymbol{K} = \pm\boldsymbol{G}/2$, i.e. $\lambda_{\boldsymbol{K}} = \lambda_{\boldsymbol{K}-\boldsymbol{G}} = \lambda = (\frac{\hbar^2}{2m_0})(\frac{G^2}{4})$. For the coefficient vector $\begin{pmatrix} C_{\boldsymbol{G}/2} \\ C_{-\boldsymbol{G}/2} \end{pmatrix}$ the determinant is

$$\begin{vmatrix} \lambda - E & U \\ U & \lambda - E \end{vmatrix} = (\lambda - E)^2 - U^2 = 0 \tag{8}$$

and thus at $\boldsymbol{K} = \pm\boldsymbol{G}/2$ the energy values are

$$E_{\pm} = \lambda \pm U = \left(\frac{\hbar^2}{2m_0}\right)\left(\frac{G^2}{4}\right) \pm U. \tag{9}$$

A splitting of the size $E_+ - E_- = 2U$ occurs with the center of the energy gap depending on $\lambda_{\boldsymbol{K}}$. In the vicinity of the zone boundary equation (8) changes to

$$\begin{vmatrix} \lambda_{\boldsymbol{K}} - E & U \\ U & \lambda_{\boldsymbol{K}-\boldsymbol{G}} - E \end{vmatrix} = 0 \tag{10}$$

and with this one finds

$$E_{\pm} = \frac{1}{2}(\lambda_{\boldsymbol{K}} + \lambda_{\boldsymbol{K}-\boldsymbol{G}}) \pm \left[\frac{1}{4}(\lambda_{\boldsymbol{K}} + \lambda_{\boldsymbol{K}-\boldsymbol{G}})^2 + U^2\right]^{\frac{1}{2}}. \tag{11}$$

With $\widehat{\boldsymbol{K}} = \boldsymbol{K} - \boldsymbol{G}/2$ and $\lambda = (\frac{\hbar^2}{2m_0})(\frac{G^2}{4})$ one can rewrite equation (11) to

$$E_{\pm}(\widehat{\boldsymbol{K}}) = \frac{\hbar^2}{2m_0}\left(\frac{1}{4}\boldsymbol{G}^2 + \boldsymbol{K}^2\right) \pm \left[4\lambda\frac{\hbar^2\boldsymbol{K}^2}{2m_0} + U^2\right]^{1/2} \tag{12}$$

and develop this for small $\widehat{\boldsymbol{K}}$ with $\hbar^2\boldsymbol{G}\widehat{\boldsymbol{K}}/(2m_0) \ll |U|$. The energy is then approximately given by:

$$E_{\pm}(\widehat{\boldsymbol{K}}) \approx \lambda \pm U + \frac{\hbar^2\widehat{\boldsymbol{K}}^2}{2m_0}\left(1 \pm \frac{2\lambda}{U}\right). \tag{13}$$

This yields a parabolic energy dispersion at the band maxima/minima, which is often used as a good approximation when discussing semiconductor properties. The curvature is given by

$$m^* = m\frac{1}{1 \pm 2\lambda/U} \approx \pm m_0\frac{U}{2\lambda}, \tag{14}$$

where m^* can be related to the effective particle mass, which is in general a tensor function and given by

$$(m^{*-1})_{ij} = \frac{1}{\hbar^2}\frac{\partial^2 E}{\partial k_i \partial k_j}. \tag{15}$$

2.1.2 Organic Semiconductors

The energy levels of small molecule organic semiconductors are derived from the hybridization of the carbon atoms [15,16]. In its single atomic state carbon has two 1s electrons, two 2s electrons and two 2p electrons. However, in all molecular assemblies the energy gained by forming four covalent bonds is

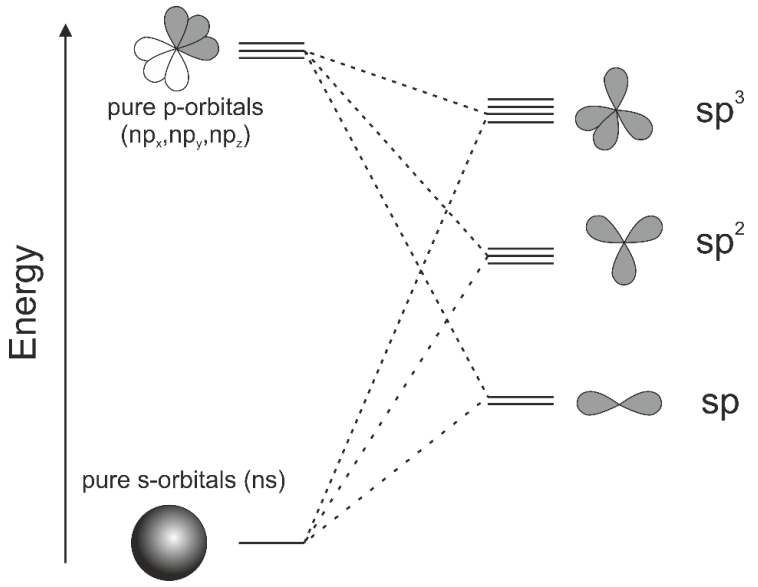

Figure 1: Illustration of pure s-orbitals, pure p-orbitals and the hybrid orbitals sp, sp^2 and sp^3 in carbon. The sp orbitals exhibit an angle of 180°, the sp^2 orbitals an angle of 120° and the sp^3 orbitals an angle of 109.5°. The carbon hybridization is the reason for the semiconducting properties of small organic molecules.

higher than the energy required to promote one 2s electron into a 2p state. The resulting single 2s electron forms new hybrid orbitals with the 2p electrons, which is usually referred to as *hybridization*. Depending on whether the 2s electron mixes with one, two or all three 2p electrons this is denoted as sp, sp^2 or sp^3 hybridization, respectively. The corresponding orbitals and their formation from pure s- and p-orbitals are illustrated in Figure 1.

These orbitals are considered *atomic* orbitals ϕ. To obtain the energy levels of organic molecules one needs to derive *molecular* orbitals ψ from them. This is achieved by a linear combination of the atomic orbitals (LCAO), a method first published by John Lennard-Jones in 1929 [17]. The method assumes that all n molecular orbitals can be expressed by a linear combination of all n atomic orbitals of the molecule:

$$\psi_i = \sum_{k=1}^{n} c_{i,k}\phi_k \tag{16}$$

Depending on the sign of the coefficients $c_{i,k}$ the molecular orbitals can be either bonding (constructive interference; enhanced charge density between atoms) or anti-bonding (destructive interference; reduced charge density between atoms). Also depending on the location of the charge density, the orbitals are either called σ-orbitals (spatial probability of electrons is centered around the axis joining two atoms) or π-orbitals (spatial probability of electrons is found above and below the axis connecting two atoms). The energy levels

of a molecule can be found by solving the Schrödinger equation (1). Different methods have been suggested to calculate the molecular orbitals, among which the Hückel-method [18–21] and density functional theory (DFT) [22,23] are nowadays most widely-used.

The orbitals of single molecules have discrete energy levels, from which the highest occupied molecular orbital (HOMO) and the lowest unoccupied molecular orbital (LUMO) are the most important ones in determining an organic semiconductors properties, as their energetic difference for example determines the electrical band gap of the semiconductor. Intermolecular interactions in an organic solid lead to a decrease of the energy gap due to depolarization by neighboring molecules and a broadening of the molecular energy levels, which is typically of Gaussian shape. If the intermolecular interactions are very strong, like for example in many polymers, the energy levels broaden even further and finally form bands. These mechanisms are schematically shown in Figure 2.

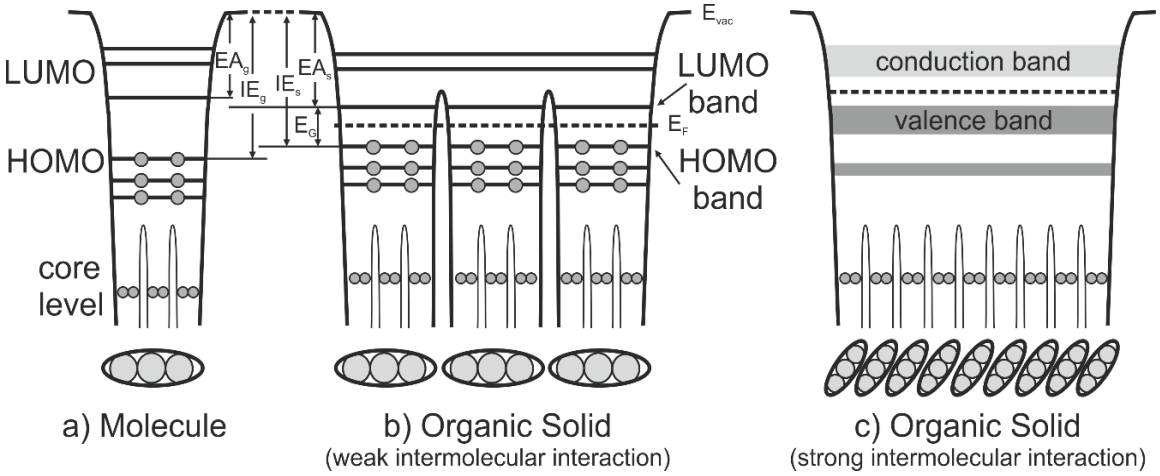

Figure 2: Change of molecular energy levels in an organic solid due to intermolecular interactions. a) Isolated molecule, with electron affinity EA_g and ionization energy IE_g. b) The depolarization by surrounding molecules leads to an increase of the electron affinity EA_s, a decrease of the ionization energy IE_s and with this to a decrease of the energy gap E_G and a broadening of the energy levels. c) In the case of strong intermolecular interaction, as often the case for polymers, the broadening leads to the formation of energy bands. Adapted from [24].

2.2 Density of States

A material property directly related to the measured signal in photoelectron spectroscopy measurements is the density of states $D(\tilde{E})$. This is the number of available states at a certain energy $\tilde{E}$ and it is related to the dispersion relation $E(\vec{k})$ by [13]

$$D(\tilde{E}) = 2 \oint_{A(\tilde{E})} \frac{\mathrm{d}^2 A}{(2\pi/L)^3} \frac{1}{\left|\nabla_{\vec{k}} E(\vec{k})\right|} . \tag{17}$$

Here $(2\pi/L)^3$ is the $\vec{k}$-space volume for one state and the surface integral runs over an isoenergy surface $A(\tilde{E})$ with $E(\vec{k}) = \tilde{E}$. At band extrema and saddle points the gradient $\left|\nabla_{\vec{k}} E(\vec{k})\right|$ becomes zero. The derivative of the density of sates diverges, although the density of states does not necessarily, but takes a finite value in three dimensions. These points are called van-Hove singularities.

For the band edges of an inorganic semiconductor, where the effective mass approximation is valid and the dispersion is a quadratic function of $\vec{k}$ (see equation (13)), the densities of states per unit volume in three dimensions are evaluated from equation (17) to be

$$D_V(E) = \frac{(2m_h^*)^{\frac{3}{2}}}{2\pi^2\hbar^3}\sqrt{E_{VBM} - E} \quad , \quad D_C(E) = \frac{(2m_e^*)^{\frac{3}{2}}}{2\pi^2\hbar^3}\sqrt{E - E_{CBM}} . \tag{18}$$

$D_V(E)$ is the density of states below the valence band maximum (E_{VBM}) and $D_C(E)$ is the density of states above the conduction band minimum (E_{CBM}). They depend on the effective masses of holes and electrons, respectively, and are therefore usually not equal. Nevertheless, the density of states becomes zero both directly above E_{VBM} and below E_{CBM}, respectively.

Since the energy levels of organic semiconductors have a rather discrete character than a band character, the density of states of organic molecules is usually also assumed to consist of discrete contributions. It is typically represented by a Gaussian distribution, a Lorentzian distribution or a mixture of both for each energy level [24]. The density of states for inorganic and organic semiconductors is schematically shown in Figure 3. However, these representations are only valid for ideal solids. In real solids the presence of defects, surface states or disorder can introduce additional density of states inside the gap. This can either be discrete, like in the case of surface or defect states, or extend from the band edges into the gap in the case of disorder [25].

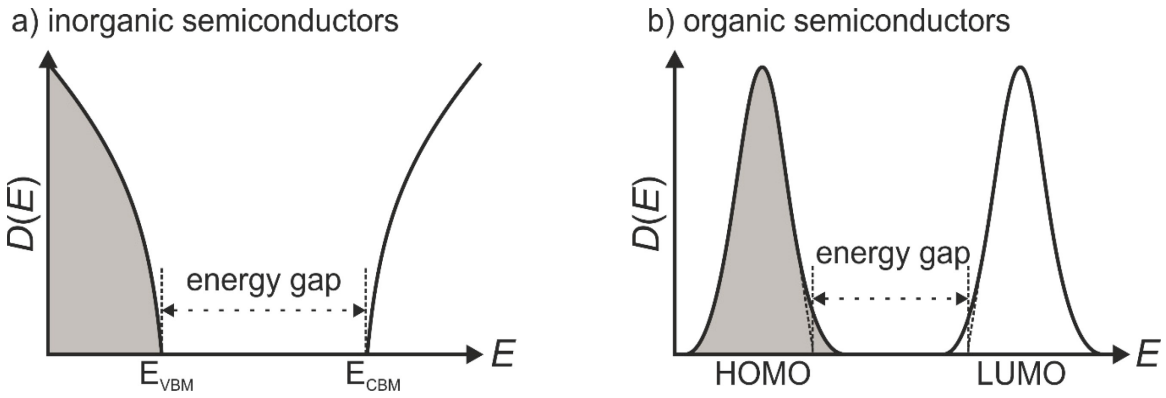

Figure 3: Schematic density of states $D(E)$ as a function of energy E for a) inorganic semiconductors (3D) and b) organic semiconductors. For inorganic semiconductors the density of states increases proportional to $\sqrt{E}$ close to the band edges, whereas the density of states of organic semiconductors is more discrete. The individual energy levels are typically represented by a Voigt-distribution. The energy gap is typically defined by a linear extrapolation to the onset of these distributions. The illustrated densities of states are only valid for ideal solids, defects and disorder in real solids can introduce states within the gap.

2.3 Doping

2.3.1 Inorganic Semiconductors

The intrinsic free carrier concentration of inorganic semiconductors depends on their band gap E_G and on the temperature and is rather low ($9.65 \cdot 10^9$ cm^{-3} at 300 K in the case of silicon [26]). Therefore pure semiconductors are typically bad conductors. To make use of them in electronic devices one needs to be able to control their conductivity over a wide range. This is achieved by introducing elements with different valency into the semiconductor lattice, which is known as intentional or extrinsic doping. Lattice defects, like vacancies or interstitials, can also lead to an increase in charge carrier density and are referred to as unintentional or intrinsic doping. The principle of extrinsic doping shall be explained in this section using the example of silicon [13,27].

A silicon atom has four valence electrons and therefore forms four covalent bonds to its neighboring silicon atoms. If one silicon atom is replaced by an atom with a higher valency, like arsenic or phosphor, the substituent has one extra electron after forming the four bonds to the neighboring silicon atoms. If this electron is ionized, a free electron is present in the lattice, while the dopant remains positively charged. Therefore these substituents are called donors, since they donate one electron into the conduction band of the semiconductor. The atomistic ionization energy of dopants is quite high (several eV), however, it is lowered by

screening of the surrounding media with a dielectric constant of ε_r and by renormalization of the effective mass m^* due to the periodic potential of the lattice. Similar considerations are valid if one silicon atom is replaced by an atom with lower valency, like boron or aluminum. To form the four covalent bonds to the neighboring silicon atoms, these substituents accept an electron from the valence band, leaving behind an extra hole in the valence band. Therefore these kind of substituents are called acceptors. Doping concentrations in inorganic semiconductors can be found in a wide range, going from 10^{13} cm^{-3} (ultra-low doping) to 10^{21} cm^{-3} (degenerate doping), where technically relevant concentrations in silicon are in the range of 10^{14}-10^{19} cm^{-3}.

The binding energy $E_b^{D/A}$ of donors or acceptors can be approximated by the scaled hydrogen ionization energy [13]:

$$E_b^{D/A} = \frac{m^*}{m_0}\frac{1}{\varepsilon_r^2}\frac{m_0 e^4}{2(4\pi\varepsilon_0\hbar)^2} \tag{19}$$

The first fraction is usually $1/10$ and the second fraction $1/100$ for many inorganic semiconductors and the ionization energy of a hydrogen atom (third fraction) is 13.6 eV. Therefore the binding energy of donors and acceptors in inorganic semiconductors is typically in the range of a few ten meV (referenced to the conduction or valence band edges, respectively).

The occupation of dopants as a function of Fermi-level position E_F inside the semiconductor is given by Fermi-Dirac-statistics [14]. With this the concentration of positively charged donors N_D^+ is calculated by

$$N_D^+ = N_D \cdot \big(1 - f(E_D)\big) = \frac{N_D}{1 + e^{\frac{E_F - E_D}{k_B T}}}, \tag{20}$$

where N_D is the total concentration of donors, f is the Fermi function and $E_D = E_C - E_b^D$. Analogously the concentration of negatively charged acceptors can be calculated by

$$N_A^- = N_A \cdot f(E_A) = \frac{N_A}{1 + e^{\frac{E_A - E_F}{k_B T}}}, \tag{21}$$

where N_A is the total concentration of acceptors and $E_A = E_V + E_b^A$. Although there are positively and negatively charged ions inside the semiconductor, the semiconductor itself

must remain neutral. For this also the intrinsically created holes p and electrons n need to be considered and the *charge neutrality equation* in its most general form is then given by

$$-n + p - N_A^- + N_D^+ = 0, \tag{22}$$

where the intrinsic electron and hole concentrations are calculated by

$$n = N_C \cdot \exp\left(\frac{E_F - E_C}{k_B T}\right) \tag{23}$$

and

$$p = N_V \cdot \exp\left(\frac{E_V - E_F}{k_B T}\right), \tag{24}$$

respectively. Here N_C and N_V are the conduction (valence) band edge densities, respectively. They are given by

$$N_{C/V} = 2\left(\frac{m_{e/h}^* k_B T}{2\pi\hbar^2}\right)^2. \tag{25}$$

Inserting equations (20), (21), (23) and (24) into the charge neutrality equation (22) it is written as

$$-N_C \cdot \exp\left(\frac{E_F - E_C}{k_B T}\right) + N_V \cdot \exp\left(\frac{E_V - E_F}{k_B T}\right) - \frac{N_A}{1 + e^{\frac{E_A - E_F}{k_B T}}} + \frac{N_D}{1 + e^{\frac{E_F - E_D}{k_B T}}} = 0. \tag{26}$$

This equation can only be solved numerically and is used within this thesis to determine the Fermi-level position within the bulk of the inorganic semiconductors.

2.3.2 Organic Semiconductors

Similar to inorganic semiconductors the conductivity of organic semiconductors can be increased by incorporation of impurities into the organic semiconductor matrix [15,16]. For doping to take place the ionization energy (electron affinity) of the donor (acceptor) needs to be lower (higher) than the electron affinity (ionization energy) of the host material. This is schematically shown in Figure 4. This makes doping of organic semiconductors much more difficult than doping of inorganic semiconductors, since typically employed organic semiconductors have electron affinities of 2.5-3.5 eV and ionization energies of 5-6 eV [28–30], which necessitates acceptors with very high electron affinities and donors with very low ionization energies, respectively. Especially the later ones are hard to obtain, since molecules with low ionization energies are typically not stable in air [31]. In the case of p-doping an electron is transferred from the host material to the acceptor, whereas in the case of n-doping an electron is transferred from the donor to the host. A so called polaron is formed. This increases the hopping transport, which is the dominant transport mechanism in most organic semiconductors [32]. However, the doping efficiency in organic semiconductors is very small compared to inorganic semiconductors [33]. Therefore doping concentrations in the range of a few percent are often needed to achieve desired conductivity values.

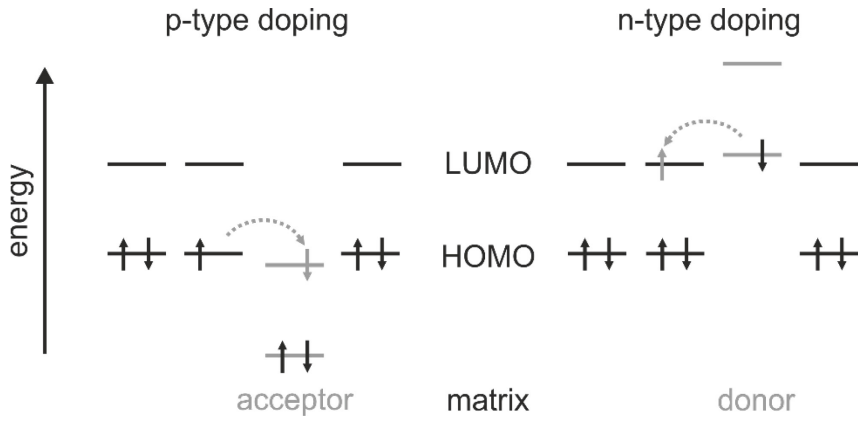

Figure 4: Principle of doping in organic semiconductors. An electron is transferred from a host molecule to an acceptor molecule (p-doping) if $EA_{acceptor} \geq IE_{host}$ or from a donor molecule to a host molecule (n-doping) if $IE_{donor} \leq EA_{host}$.

2.3.3 Interface Doping, Integer Charge Transfer vs. Hybridization

The above mentioned kinds of doping are both regarding the bulk of the semiconductors. However, also at interfaces charge transfer can take place, which leads to doping of the semiconductor only in the vicinity of the interface. This effect is therefore called *interface doping* and is often used to improve carrier injection/extraction at electrode interfaces [35,36]. The charge transfer takes place if the HOMO (LUMO) level of the organic semiconductor lies energetically above (below) the Fermi-level of the substrate. It can be differentiated between two types of charge transfer, depending on the interaction between the molecules and the substrate [34]. In the case of strong interaction, hybridization between the frontier orbitals of the molecule and the substrate takes place and the transferred charge is distributed equally between all molecules. This can be observed e.g. as a partially filled LUMO at the Fermi-level in UPS measurements and has particularly been seen for atomically clean metal surfaces [37,38]. When the substrate/organic interaction is weak, like in the case of atomically inert substrates or a decoupling from the metal by ultrathin buffer layers [39], the frontier orbitals cannot hybridize and integer charged molecules will coexist next to neutral molecules. It has only been recently achieved to capture these different effects by density functional theory calculations [34], as integer charge transfer requires large unit cells and is therefore computationally expensive. In Figure 5 the difference between the two scenarios is shown schematically for electron accepting molecules.

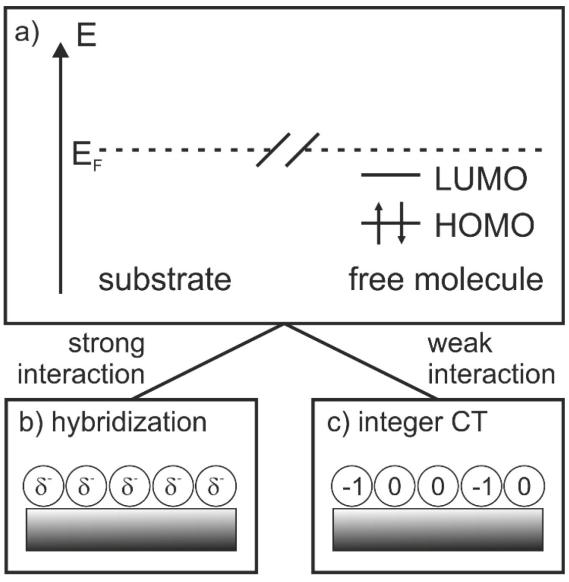

Figure 5: Schematic illustration of the difference between hybridization and integer charge transfer for electron accepting molecules. a) Energetic situation before contact. The LUMO level of the molecule needs to be positioned below the Fermi-level of the substrate for charge transfer. b) For strong substrate/molecule interaction the molecular frontier orbitals hybridize and get all equally charged. c) In the case of weak substrate/molecule interaction some integer charged molecules coexist together with neutral molecules. Adapted from [34].

2.4 Energy Level Alignment

In this section the principal phenomena that can occur at interfaces, regarding the energetic alignment, are introduced. Two important terms in this context, *interface dipole* and *band bending*, are introduced and discussed on four exemplarily interfaces.

Band bending describes the spatially extended change in potential of a semiconductor near a surface or an interface [40]. Inside the bulk of a semiconductor charge neutrality is valid and the energy bands (conduction and valence band) are flat. At a surface or interface charge neutrality does not necessarily need to be valid anymore. According to Poisson-equation

$$\Delta V(z) = -\frac{\rho(z)}{\varepsilon\varepsilon_0} \tag{27}$$

a local charge distribution $\rho(z)$ leads to a change in the local potential $V(z)$. If the change in potential occurs between two materials in a spatially abrupt manner, due to the rearrangement or transfer of charge, it is typically called formation of an interface dipole.

2.4.1 Metal – Inorganic Semiconductor Interface

The standard example of a situation demonstrating band bending is the formation of a Schottky-contact at a metal-inorganic semiconductor interface. This is exemplarily shown in Figure 6 for an n-type semiconductor. The following explanations hold in the analogous way for a p-type semiconductor. The parameters used to describe the energy level alignment of a semiconductor at an interface are its work function Φ_S, defined as the difference between vacuum level E_{vac} and Fermi-level E_F, and its electron affinity EA (ionization energy IE) for an n-type (p-type) semiconductor, which is the difference

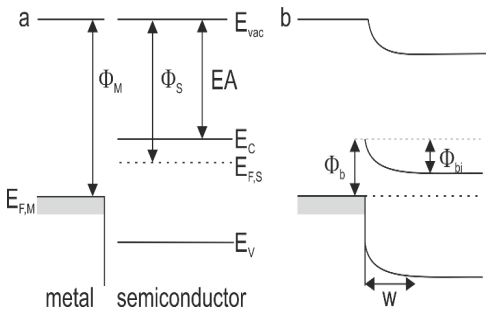

Figure 6: Formation of a metal / n-type semiconductor contact. Shown are the energy levels a) before contact and b) after contact. An electron flow from the semiconductor to the metal leads to the formation of a space charge region inside the semiconductor. $\Phi_{M/S}$ denotes the respective work functions, E_F the Fermi-level, $E_{C/V}$ conduction/valence band, E_{vac} the vacuum level, EA the electron affinity, Φ_b the barrier height, Φ_{bi} the built-in potential and w the extension of the space charge region.

between E_{vac} and the conduction (valence) band. When the semiconductor is brought into contact with a metal the difference in work functions determines whether a rectifying Schottky-contact or an ohmic contact is formed. If the work function of the metal Φ_M is larger than the work function of the semiconductor Φ_S (as shown in Figure 6) electrons will flow from the semiconductor to the metal until the Fermi-level throughout the whole heterostructure is constant. This will lead to a depletion of electrons in the surface region of the semiconductor and positively charged, spatially fixed donors remain. This static charge leads to an upward bending of the semiconductor energy bands according to equation (27). The result is the formation of a potential barrier Φ_b between metal and semiconductor, given by $\Phi_b=\Phi_M$-EA, and a built-in potential Φ_{bi} inside the semiconductor, given by $\Phi_{bi}=\Phi_M$-EA-eV_n, where V_n is the difference between conduction band and Fermi-level in the bulk of the semiconductor. The width w of the depletion region is usually calculated using full-depletion approximation [13]. This assumes that within a certain length w away from the interface all donors are ionized, otherwise they are neutral. The resulting potential V(x) decreases quadratically with distance to the interface.

2.4.2 Metal – Organic Semiconductor Interface

It has just been recently discussed by Oezehlt *et al.* that the energy level alignment of metal electrodes and organic semiconductors can be described completely by Poisson-equation and Fermi-statistics and depends mainly on the density of states of the organic frontier orbital levels [24]. The density of states of an organic semiconductors frontier orbital levels $D_{H/L}(E)$ can be generally described by a Voigt-profile. Depending on the molecule, Gaussian or Lorentzian contributions can predominate. The density of states of a metal on the other hand is described by a Fermi-distribution $f(E)$ (compare equation (21)). If organic semiconductor and metal are brought into contact, besides the well-known push-back or pillow effect [41,42], which decreases the work function of clean metals due to charge rearrangement of the charge density spilling out of the metal surface, a charge transfer might occur, depending on the values of metal work function and ionization potential or electron affinity of the organic semiconductor. The transferred charge will lead to a change of the electrostatic potential $V(z)$ inside the organic semiconductor according to Poisson-equation (27). For a given potential the charge density of the organic semiconductor $\rho(z)$ can be calculated following Fermi-Dirac-statistics and is given by

where n is the density of molecules. The first integral yields the number of holes in the HOMO and the second integral the number of electrons in the LUMO at each position z. This redistribution of charge will then again lead to a change in the potential, so that

$$\rho(z) = e \cdot n \cdot \left\{ \int_{-\infty}^{\infty} \big(1 - f(E)\big) \cdot D_H\big(E + eV(z)\big) dE - \int_{-\infty}^{\infty} f(E) \cdot D_L\big(E + eV(z)\big) dE \right\}, \tag{28}$$

equations (27) and (28) need to be solved iteratively until no further change in the charge distribution and potential occur, considering the boundary conditions $V(0) = 0$ and $V'(d) = 0$, where d is the film thickness of the organic semiconductor. These ensure that there are no discontinuities in the potential at the metal-organic interface and that the electric field vanishes outside the organic layer. An exemplary initial condition together with the final results for a metal with an effective work function of 5.3 eV and a 30 nm layer of standing pentacene are shown in Figure 7 and Figure 8. The charge distribution of holes inside the pentacene layer is shown in Figure 8 a) and demonstrates that most of the charge is concentrated within the first few layers of the organic semiconductor, which is also observed in experiment [43–45]. Figure 8 b) demonstrates how the transition from interface dipole (abrupt potential drop at the interface) to band bending (extended potential change within the organic layer) depends on the shape of the DOS of the organic semiconductor, which can also be observed in experiment. While Alq_3 on clean silver

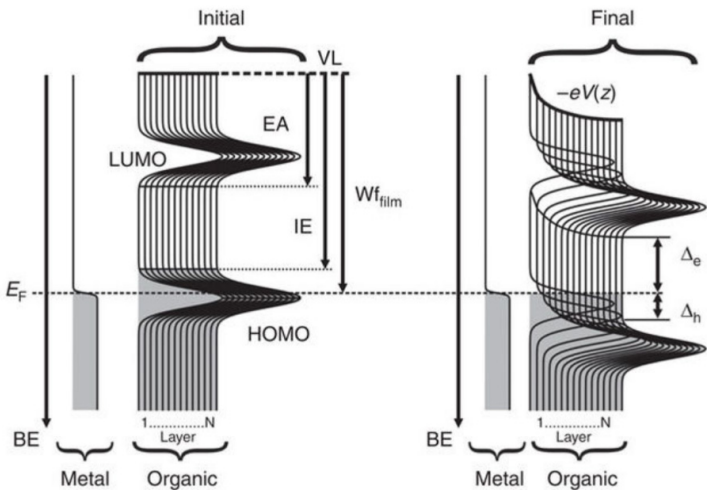

Figure 7: Exemplary illustration of energy level alignment at an organic/metal interface. Shown are the initial conditions and the final results of the calculations described in section 2.4.2. The charge transfer leads to a potential drop inside the organic semiconductor. Adapted from [25].

shows a distinct interface dipole [46] with a potential drop across the first molecular layer, C_{60} on thermally evaporated MoO_x on the other hand shows an extended band bending region over several tens of nm [47]. Finally Figure 8 c) shows the electron injection barrier Δ_e (Φ-EA) and hole injection barrier Δ_h (IE-Φ) as a function of effective metal work function. Both properties show a "Z-shape" [48,49]. As long as the work function of the underlying metal is positioned well within the gap of the organic semiconductor, the organic film simply adapts the substrate work function (vacuum level alignment) and both hole and electron barrier exhibit a linear dependence on the substrate work function. Once the substrate work function falls below or exceeds a certain work function (Φ^- or Φ^+) the work function of the organic film ends up at a fixed value a few hundred meV above the EA or below the IE of the organic semiconductor. This is called LUMO-level or HOMO-level pinning, respectively. It was shown that this pinning emerges naturally and is not connected with certain quantum-mechanical states present in the gap of the organic semiconductor, often referred to as polaron levels or "integer charge-transfer" states [50]. The described electrostatic effects and calculations can be further extended to include temperature dependence or the presence of states tailoring into the gap [51].

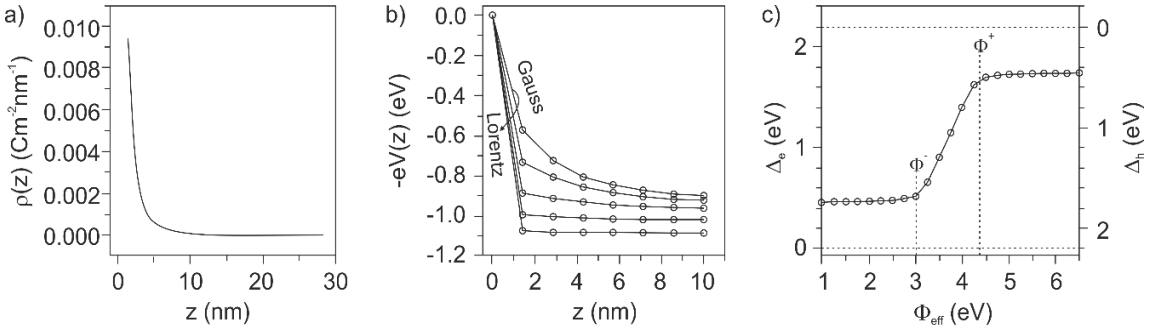

Figure 8: Results for a 30 nm layer of standing pentacene on a metal with an effective work function of 5.3 eV. a) Hole density within the pentacene layer, demonstrating that charge transfer is mainly restricted to the first layer. b) Potential distribution within the organic layer for different shapes of the organic DOS, demonstrating a transition from band bending (pure Gaussian) to interface dipole (pure Lorentzian). c) Electron Δ_e and hole Δ_h injection barriers as a function of effective metal work function, demonstrating a Z-shape with HOMO and LUMO level pinning at Φ^+ and Φ^-, respectively. Adapted from [25].

2.4.3 Inorganic Semiconductor - Organic Semiconductor Interfaces

In inorganic-organic semiconductor heterojunctions a combination of interface dipole formation and band bending in both semiconductors can occur. The pillow effect is usually

negligible for this materials, as their electron density is much lower compared to metals (typically ≥ 5 orders of magnitude) and with this the spill-out of charge density outside the surface leads to a much smaller surface dipole [52]. The most striking differences to metal/organic semiconductor interfaces are the possibility to induce different doping concentrations inside the bulk of inorganic semiconductor and the possible presence of surface states at the inorganic semiconductor surface, which can induce additional density of states inside the band gap of the inorganic semiconductor.

2.4.4 Inorganic Semiconductor – Vacuum Interface: The Role of Surface States

The periodicity of a semiconductor crystal lattice leads to its band structure with a certain energy gap as described in section 2.1.1. At a surface, however, this periodicity is broken. This leads to the emergence of new states, depending on the surface termination, from which some can lie energetically inside the semiconductor band gap. These are so called "gap states" or generally "surface states". Pioneer work in this field has been done by *Tamm*, *Shockley* and *Bardeen* between 1932 and 1947 [53–55]. The whole semiconductor, including the surface, must fulfill the condition of charge neutrality:

$$Q_{SS} + Q_{SC} = 0 \tag{29}$$

The charge accumulated in the surface states Q_{SS} must be compensated by counter charges in the space charge region inside the semiconductor Q_{SC}. In space charge approximation [13], which assumes all donors or acceptors to be ionized up to a certain depth w, the charge in the depletion region is given by

$$Q_{SC} = \pm\sqrt{2\varepsilon\varepsilon_0 e N_{D/A} V_{BB}}\,, \tag{30}$$

where V_{BB} is the total magnitude of band bending. Mobile charge carriers are neglected, it's assumed that all charge stems from the ionized impurities. The concentration of charged surface states, given a total amount of surface states N_{SS} at a concrete energy E_{SS}, is given by Fermi-Dirac-statistics

$$Q_{SS} = \mp \frac{eN_{SS}}{1 + \exp\left(\frac{\pm[(E_{SS} \pm V_{BB}) - E_F]}{k_B T}\right)}, \tag{31}$$

where the upper sign applies for acceptor-type surface states and upward band bending and the lower sign for donor-type surface states and downward band bending. E_F is the Fermi-level position within the bulk of the semiconductor, which can be determined from equation (26). Putting equations (30) and (31) into equation (29) this can be solved numerically for V_{BB} for a given surface state density and doping concentration. It should be mentioned here that surface states of acceptor-type only lead to band bending for n-doped semiconductors, whereas surface states of donor-type only lead to band bending on p-doped semiconductors. As an example the calculated band bending as a function of surface state density is shown in Figure 9 for n-doped silicon with different doping concentrations and a fictive surface state density at midgap position. Once the surface state density exceeds a certain concentration, the band bending increases rapidly, while it increases much less if the surface state density is further increased (region indicated by dashed lines). This phenomenon is known as *pinning of the Fermi-level at semiconductor surface states*. It is the reason for the deviation of barrier heights at metal-semiconductor contacts from the Schottky-Mott rule [53]. The surface state density plays also an important role for the energetic alignment to organic semiconductors, as shown in section 5.2. For higher doping concentrations, a higher amount of surface states is necessary to induce Fermi-level pinning. Also the magnitude of the band bending increases slightly, because the Fermi-level in the bulk is located closer to the conduction band and therefore energetically further away from the surface states.

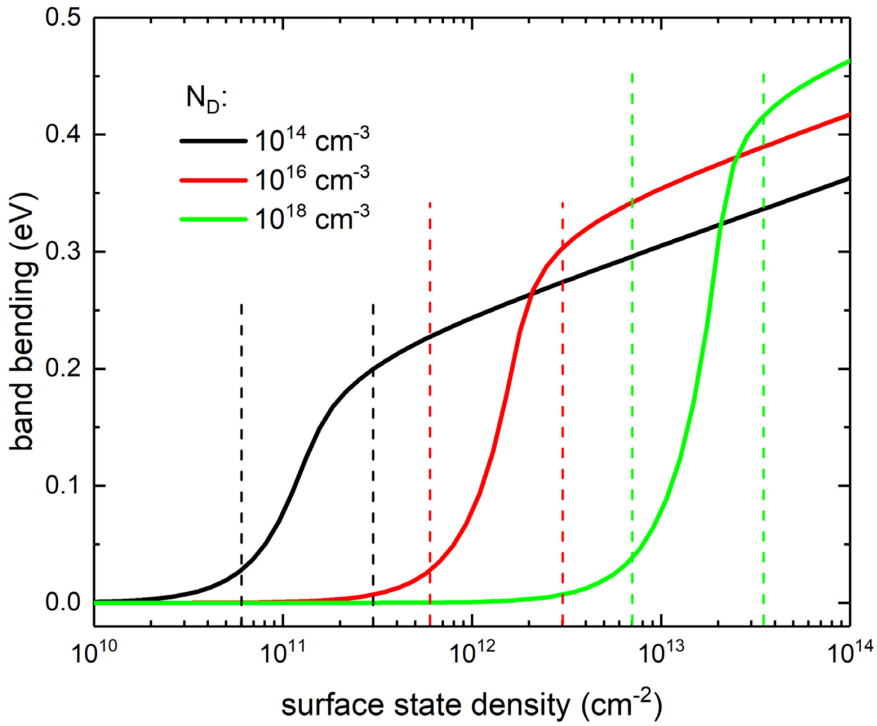

Figure 9: Band bending as a function of surface state density for n-type silicon with different doping concentrations and fictional acceptor surface states at midgap position. Over a certain critical surface state density the band bending increases rapidly. This phenomenon is known as *pinning of the Fermi-level at semiconductor surface states*.

3 Experimental Methods

In this chapter the experimental methods used in this work to characterize the inorganic and organic materials, as well as the energy level alignment at the interfaces, are introduced. Here the main focus is on the theoretical background and the working principle of the particular measurements. The experimental setups are described in detail in chapter 4.

3.1 Photoelectron Spectroscopy

Photoelectron spectroscopy (PES) is a widely used technique to investigate the electronic structure of occupied states in all kind of materials nowadays. It is based on the photoelectric effect, first described by Einstein in 1905 [56]. An incoming photon excites an electron into the vacuum, if its energy hv is larger than the sum of the binding energy of the electron E_B and the samples work function Φ_s. The excess energy can be measured as kinetic energy E_k by an energy analyzer with work function Φ_d and is given by

$$E_k = hv - E_B - \Phi_d \,. \tag{32}$$

The photoemission process can be described quantum mechanically correct in a one-step emission process, including Fermi's golden rule, proper initial and final states and the dipole operator for the interaction of the electron and the incoming light. However, this problem is very hard to solve. Therefore a phenomenological, more intuitive three-step model is often applied to describe the photoemission process [57]. The models are schematically shown in Figure 10. The three step model includes the following steps:

1. optical excitation of the electron within the solid
2. transport of the excited electron to the surface
3. escape of the electron into the vacuum

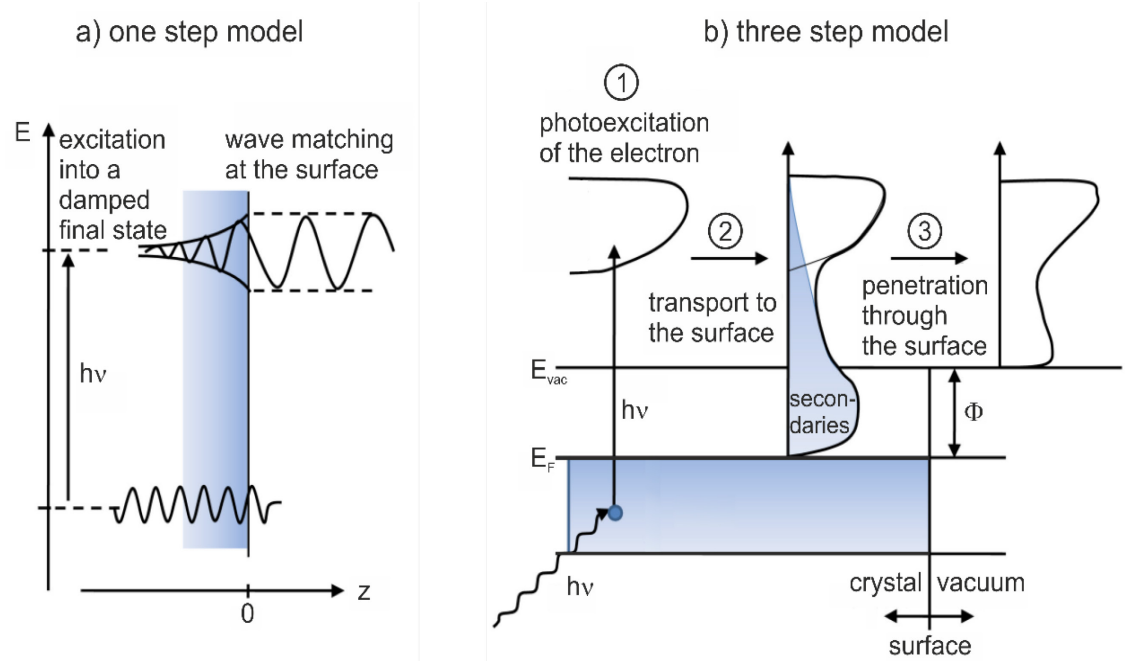

Figure 10: Comparison between one step and three step model in photoemission. a) In the one step model a Bloch wave electron is excited into a wave that propagates freely in the vacuum but decays away from the surface into the solid. b) In the three step model this process is divided into three steps: 1) the photoexcitation of the electron inside the material, 2) the transport of the excited electron to the surface, involving scattering and the production of secondary electrons and 3) the penetration of the electron through the surface into the vacuum.

3.1.1 Photoemission Process: the Three-Step Model

1. Photoexcitation of electrons

In the first step the probability w of photoexciting an electron from an initial system with N electrons (described by the wave function Ψ_i and energy E_i) into a final system with N-1 electrons (described by the wave function Ψ_f and energy E_f) is given by Fermi's golden rule [57]. In dipole approximation (radiation wavelength is large compared to the excited volume) w is given by

$$w \propto \frac{2\pi}{\hbar}\left|\langle\Psi_f|H|\Psi_i\rangle\right|^2 \delta(E_f - E_i - h\nu), \tag{33}$$

where H is the Hamiltonian operator and $\langle\Psi_f|H|\Psi_i\rangle$ the transition matrix element. In the simplest approximation, known as *Koopmans' theorem* [58], it is assumed that the ionization process does not impact the wave function of the remaining electrons. Only in

this case the measured binding energy corresponds to the binding energy of the undisturbed system. However, in reality the kinetic energy of the excited electron will be reduced by the coulomb interaction with the remaining photo-hole. Furthermore, the system will react to the presence of the photo-hole and try to minimize its energy by relaxation and screening.

2. Transport of the electrons to the surface

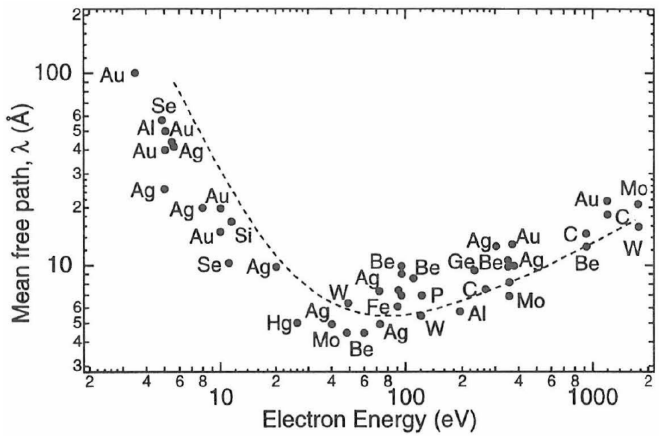

Figure 11: Energy dependence of the inelastic mean free path λ for electrons in a solid. It is material independent and therefore also known as *universal curve*. Adapted from [59]. λ is in the order of a few nm, making photoelectron spectroscopy a very surface sensitive technique.

On their way to the surface the excited electrons can undergo inelastic scattering, which will lead to a reduction of their kinetic energy. By this they lose their specific information (binding energy of the initial orbital) and contribute to the background, if they retain enough energy to leave the sample. The intensity of primary electrons I_0 decays exponentially as a function of travelled distance and can be described by the *Lambert-Beer law* $I(d) = I_0 e^{-d/\lambda(E)}$, where $\lambda(E)$ is the distance after which the intensity of an electron beam is decayed to $1/e$ and is called inelastic mean free path (IMFP) [60]. The energy dependence of the IMFP is independent of the material, yielding the so called *universal curve* shown in Figure 11. Considering that the value of the IMFP is in the range of a few nm for most kinetic energies it becomes clear that photoelectron spectroscopy is a very surface sensitive technique. The IMFP can be calculated by different approximations, e.g. the one given by *Seah and Dench* [61]:

$$\lambda(E) \approx \frac{143nm \cdot eV^2}{E^2} + \sqrt{0.003 \frac{nm^2}{eV} \cdot E} \tag{34}$$

3. Penetration of the electrons through the surface

Due to translational symmetry parallel to the surface an electron must maintain its parallel momentum component $k_{||}$ when leaving a solid [57]. It is related to its kinetic energy by $|\vec{k}_{||}| = \sin(\alpha) \cdot \sqrt{2m_0 E_k/\hbar}$, where α is the emission angle with respect to the surface normal. Its perpendicular momentum component $\vec{k}_{\perp}$, however, might change due to the change in potential at the surface. It can still be calculated by solving $E_k = \frac{\hbar}{2m}\left[\left(\vec{k}_{||}\right)^2 + \left(\vec{k}_{\perp}\right)^2\right]$. These relationships are exploited in angle-resolved photoelectron spectroscopy (ARPES). After the electron has successfully escaped the solid and overcome the work function of the sample it is collected by the analyzer and its kinetic energy is measured. For this its kinetic energy must be larger than the difference between the work function of the sample Φ_s and the work function of the detector Φ_d. Sample and detector are electrically connected and have therefore a common Fermi-level. This is schematically shown in Figure 12. Secondary electrons, which can barely overcome the work function of the sample, have in principle zero kinetic energy. To make sure that those electrons can reach the detector, and with this yield direct information about Φ_s, a negative bias of typically a few volts is applied between the sample and the detector when measuring the secondary electron cut-off (SECO).

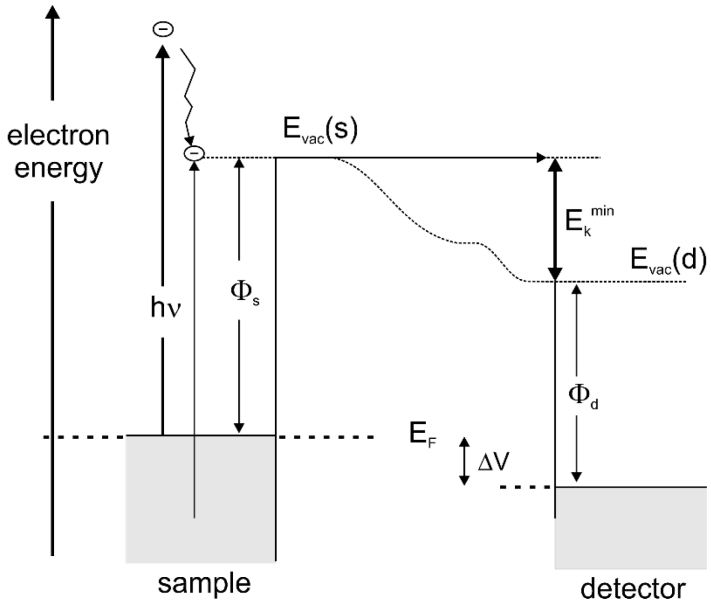

Figure 12: Working principle of photoelectron spectroscopy. An incoming photon with energy $h\nu$ excites an electron from the sample into the vacuum, where its kinetic energy is measured by an energy analyzer. Sample and detector have the same Fermi-Level E_F, but different work functions Φ_s and Φ_d. The minimum kinetic energy E_k^{min} of the SECO is a direct measure of Φ_s. Usually a negative bias ΔV is applied when measuring the SECO, lowering the vacuum and Fermi level at the detector.

3.1.2 Energy Distribution Curves and Characteristic Parameters Obtained by PES

Photoemission experiments are typically divided into two types, depending on the excitation energy and the type of states under investigation. On the one hand there is ultraviolet photoelectron spectroscopy (UPS), where the excitation energy is in the range of 10-100 eV. On the other hand there is x-ray photoemission spectroscopy (XPS), where the excitation energy is typically in the range of 1000 eV. Higher energies, in the range of several keV, are employed in hard x-ray photoelectron spectroscopy (HAXPES) experiments, but should not be discussed here.

Ultraviolet photoemission spectroscopy (UPS)

UPS is usually used to investigate the electronic states within the valence region of a material, with binding energies typically between 0 and 12 eV. A typical lab source for UPS measurements is a He discharge lamp, with a characteristic photon energy hv of 21.21 eV. The advantage of this type of light source is a very good energy resolution (full width at half maximum of the photons is only around 8 meV) and a high flux. Therefore very fine features in the valence or HOMO region, respectively, can be resolved. A typical energy distribution curve (EDC) of a thin organic layer deposited on top of a metal is shown in Figure 13. The kinetic energy of electrons originating from the Fermi-level (E_F) of a metal is typically used to determine the work function of the detector. The width of the Fermi-level is further used to determine the energy resolution of the analyzer. This is described in detail in section 4.2. The kinetic energy of the secondary electron cut-off (SECO) onset gives direct information about the work function Φ_s of the sample, if the sample work function is homogeneous. The consequences of heterogeneities on the SECO shape and details about a more evolved analysis are discussed in section 5.1. For organic or inorganic semiconductors usually the binding energy of the HOMO onset E_B^{HOMO} or of the valence band maximum E_B^{VBM} are of interest, as they for example determine the hole injection barrier Δ_h between the semiconductor and the metal below. They are further used to determine the ionization energy IE of a material by adding it to its work function:

$$IE = \Phi_s + E_B^{HOMO/VBM} \tag{35}$$

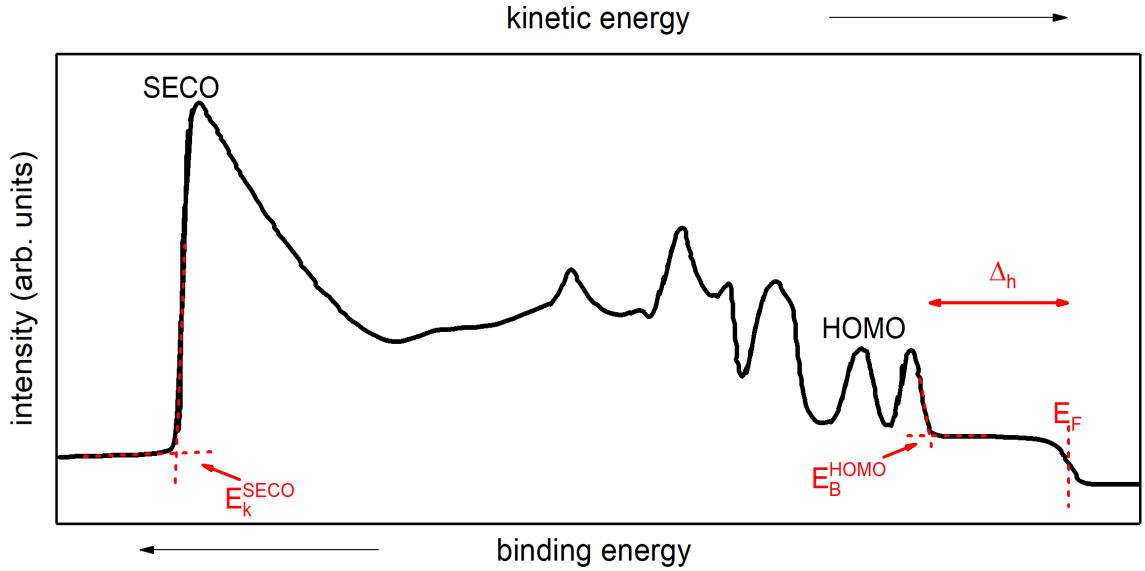

Figure 13: Typical energy distribution curve (EDC) obtained by UPS measurements of a thin organic layer deposited onto a metal. Characteristic values (red) which can be obtained from this curve are: the kinetic energy of the SECO (E_k^{SECO}), which is a direct measure of the sample work function; the kinetic energy of electrons emitted from the metal Fermi-level (E_F), which is used to calibrate the work function of the analyzer; the binding energy of the HOMO onset, which can be used to determine the hole injection barrier Δ_h.

X-ray photoemission spectroscopy (XPS)

The photon sources typically used in XPS are the characteristic x-ray emission lines of either Mg K_α (1253.6 eV) or Al K_α (1486.6 eV). For improved resolution and to avoid satellite peaks a monochromator can be used. The aim of XPS is the investigation of core levels of a sample, to obtain information about chemical composition, different charge states or changes in band bending. Each element has characteristic emission lines, which allow for the identification and quantification of the different contributions. For this purpose usually a *survey* or *wide range* scan is recorded first, as exemplarily shown Figure 14 a) for dirty gold (black) and sputter-cleaned gold (red). In the survey spectrum of dirty gold, carbon and oxygen contaminations can be identified, which were removed after sputter-cleaning. For quantification and identification of different chemical states narrow scans are performed, as shown in Figure 14 b) for the Au4f region. For this the pass energy of the analyzer is typically decreased compared to a survey spectrum, to achieve better resolution.

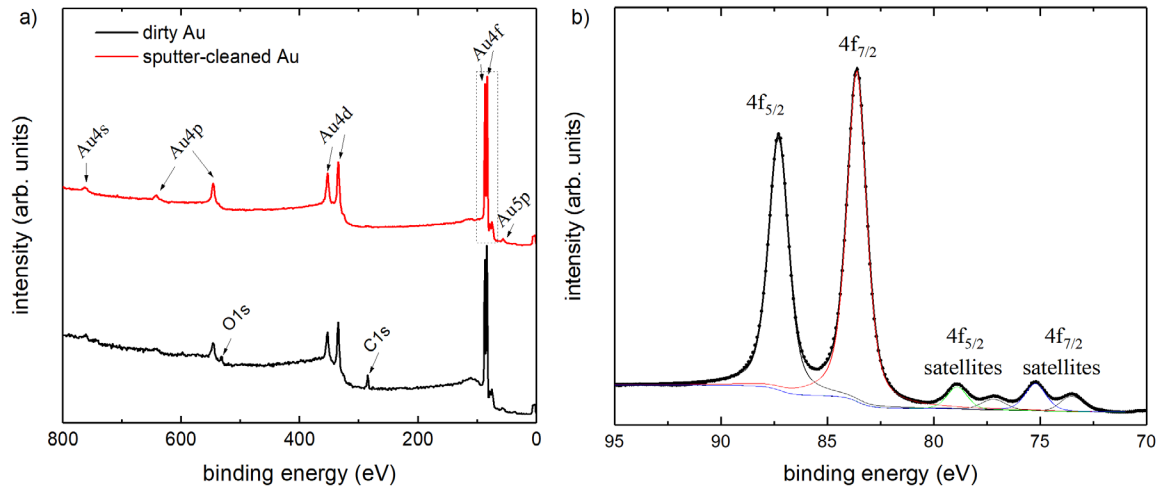

Figure 14: XPS results of a Au single crystal. a) Survey scans of dirty Au (black), showing carbon and oxygen contaminations, and sputter-cleaned Au (red). b) Narrow scan of the Au4f region, as indicated by the rectangle in a), including Shirley-background and peak fits.

a) Shirley background

The scattering of electrons on their way to the surface, as described in section 3.1, leads to an increase of the signal intensity at the higher binding energy side of a main peak, as photoelectrons lose some of their kinetic energy in the scattering process. Most often used in XPS evaluation to describe this process is the empirical *Shirley* background in its iterative form [57,62–64]. It is calculated iteratively by

$$S_i(E) = k \int_E^{\infty} \left(j(E') - S_{i-1}(E') \right) dE', \tag{36}$$

where k is a fitting constant, j(E) is the intensity measured at energy E and S_i is the calculated background. The initial guess S_0 is simply the intensity before the peak and the background converges after a few iterations. It implies that the background intensity is proportional to the integrated intensity of the spectrum. A Shirley background was applied to the Au4f spectrum in Figure 14 b) (grey line). It can be seen that the background increases after each peak.

b) Peak shapes

The natural energy distribution ΔE of XPS core levels is connected to the limited life-time Δt of the core hole state via the uncertainty principle $\Delta E \cdot \Delta t \geq \hbar/2$. Since the core hole state decays exponentially in time, the natural energy distribution of a XPS peak is of Lorentzian shape [65]. However, this intrinsic signal is altered by the energy distribution

of the excitation source and the energy analyzer, which are typically of Gaussian shape. Therefore the measured signal is a convolution of both functions, which is known as Voigt-function and given by

$$V(E) = \int_{-\infty}^{\infty} \frac{e^{-E'^2/(2\sigma)^2}}{\sigma\sqrt{2\pi}} \frac{\gamma}{\pi((E-E')^2+\gamma^2)} dE' , \qquad (37)$$

where σ is the width of the Gaussian distribution and γ is the width of the Lorentzian distribution. The full widths at half maximum (FWHM) are given by $\mathrm{FWHM_G} = 2\sigma\sqrt{2\ln(2)}$, $\mathrm{FWHM_L} = 2\gamma$ and $\mathrm{FWHM_V} = 0.5346 \cdot \mathrm{FWHM_L} + \sqrt{0.2166 \cdot \mathrm{FWHM_L^2} + \mathrm{FWHM_G^2}}$ [66]. Two Voigt profiles with different fractions of Gaussian and Lorentzian contributions are shown together with a pure Gaussian and a pure Lorentzian peak in Figure 15. They all have the same FWHM for comparison. In XPS core level peaks of oxides or at high binding energy tend to have more Gaussian character, whereas metallic peaks or peaks at lower binding energies tend to be more of Lorentzian like shape.

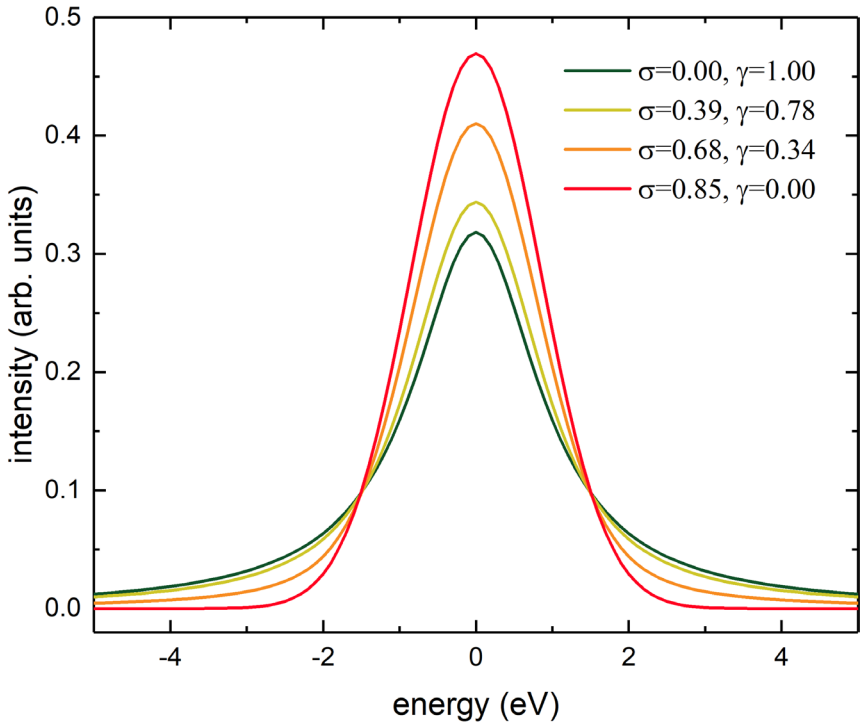

Figure 15: Voigt-profiles with different fractions of Gaussian σ and Lorentzian γ contribution. The limiting cases of a pure Gaussian (red) and a pure Lorentzian (green) are shown for comparison. All peaks have a full width at half maximum of 2 eV.

c) Elemental quantification

Since the number of emitted electrons of a XPS peak is directly proportional to the number of the respective atoms n, XPS can also be used as a quantitative technique. For a homogeneous sample the number of electrons per second I for a specific peak is given by [67]

$$I = nf\sigma\Theta y\lambda AT, \tag{38}$$

where f is the x-ray flux in photons/(cm^{2}s), σ is the photoelectric cross-section for the atomic orbital of interest in cm^2, Θ is an angular efficiency factor for the instrumental arrangement based on the angle between the photon path and the detected electrons, y is the efficiency in the photoelectric process for formation of photoelectrons of the normal photoelectron energy, λ is the mean free path of the electron as discussed in section 0, A is the area of the sample from which photoelectrons are detected and T is the detection efficiency for electrons emitted from the sample. For a given experimental setup and core level peak the parameters $f, \sigma, \Theta, y, \lambda, A$ and T are usually considered constant and grouped together to an *atomic sensitivity factor* S. A list of atomic sensitivity factors is usually provided by the manufacturer of a XPS setup. The concentration c_x of each element can then be calculated as

$$c_x = \frac{n_x}{\sum_i n_i} = \frac{I_x/S_x}{\sum_i I_i/S_i}. \tag{39}$$

For I_i the integrated peak area usually yields more reliable results than simply taking the peak height. By carefully conducted measurements and an adequate data analysis, including background subtraction as described earlier, a quantification with a precision of a few percent is possible [68].

3.2 Scanning Probe Microscopy

3.2.1 Atomic Force Microscopy

One of the main techniques nowadays to investigate the topography of surfaces, even down to atomic resolution, is *Atomic Force Microscopy* (AFM) [69]. It uses the attractive and repulsive forces between the sample surface and a sharp tip to obtain a height image of the surface. The effective forces can be described by the Lenard-Jones potential, shown in Figure 16 a). Far away from the sample surface the tip does not feel any forces. When the tip approaches the surface, attractive forces, like Van-der Waals or permanent dipole-dipole interactions, appear. If the tip is further approached to the surface, strong repelling forces set in due to repulsion of the atomic nuclei and the Pauli exclusion principle [70]. At a distance r_m both forces are in equilibrium. The AFM used in this work is based on the new Peak Force Tapping™ mode developed by Bruker in 2012 [71]. At each measurement spot the system measures a force-distance curve by approaching and departing the surface with a frequency of 2 kHz. The force thereby acting on the tip is shown in Figure 16 b). The maximum repulsive force (point C) is used as a feedback signal to control the z-Piezo and to keep a constant distance to the surface. As with conventional AFM modes (contact, tapping) this force is measured via the deflection of the cantilever, by measuring the reflection of a laser from the cantilever onto a four segment photodetector.

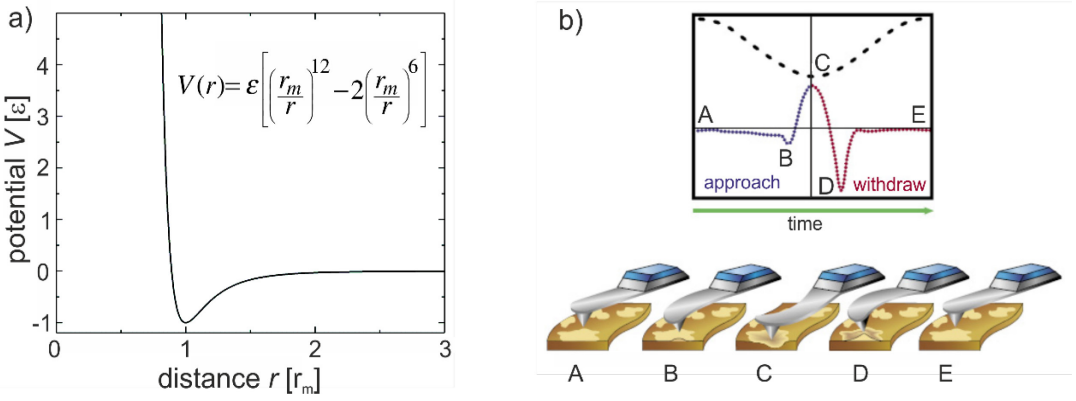

Figure 16: Working principle of atomic force microscopy (AFM). a) Lennard-Jones potential, with r_m being the distance where attractive and repulsive forces are equal. b) Working principle of Bruker's Peak Force Tapping™ mode [71].

3.2.2 Kelvin-Probe Force Microscopy

Kelvin-Probe Force Microscopy (KPFM) is a combination of the macroscopic Kelvin probe with an AFM [72]. Like the Kelvin probe, this technique is used to determine the work function difference between a sample surface and the applied tip. When a conductive tip and the sample are brought into electrical contact by a back contact their Fermi-levels will align. This leads to a flow of charges and the development of a contact potential difference eV_{CPD} between tip and sample, as schematically depicted in Figure 17 a) and b). For KPFM measurements an electric bias $V(t) = V_{DC} + V_{AC} \cdot sin(\omega t)$ is applied at the tip with a frequency ω of a few kHz. This leads to an electrostatic force acting on the tip, which can be divided into three different frequency components:

$$F_{\mathrm{DC}} = \frac{\mathrm{d}C}{\mathrm{d}z}\left[\frac{1}{2}(V_{\mathrm{DC}} - V_{\mathrm{CPD}})^2 + \frac{1}{4}V_{\mathrm{AC}}^2\right] \tag{40}$$

$$F_{\omega} = \frac{\mathrm{d}C}{\mathrm{d}z}(V_{\mathrm{DC}} - V_{\mathrm{CPD}})V_{\mathrm{AC}}\sin(\omega t) \tag{41}$$

$$F_{2\omega} = -\frac{1}{4}\frac{\mathrm{d}C}{\mathrm{d}z}V_{\mathrm{AC}}^2\cos(\omega t) \tag{42}$$

The same forces act at frequencies close to the resonance frequency of the cantilever ω_0. For KPFM measurements either the force F_{ω} (amplitude modulated, AM-KPFM) or the force gradient $\frac{\partial F_{\omega_0 \pm \omega}}{\partial z}$ (frequency modulated, FM-KPFM) is observed. In this work only FM-KPFM is used due to its better resolution [73]. The applied DC voltage V_{DC} is varied until $\frac{\partial F_{\omega_0 \pm \omega}}{\partial z}$ becomes zero. In this case the applied bias corresponds directly to the contact potential difference V_{CPD}. KPFM measurements are mostly conducted in *lift mode*. Here the topography is measured in a first scan in Peak Force Tapping™ mode (see section 3.2). In a second scan the tip is lifted from the surface and the topography is retraced at a constant distance without mechanically driving the cantilever. During this second scan a potential profile is obtained. This allows for decoupling of topography and electrostatic properties and reduces crosstalk.

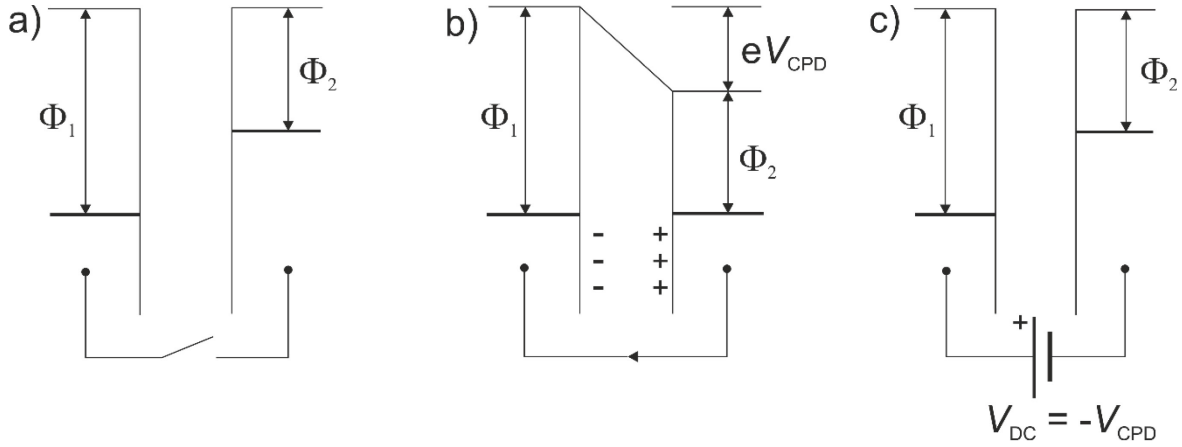

Figure 17: Schematic working principle of KPFM. a) Before sample and tip are brought in contact by a back contact they usually have different work functions Φ_1 and Φ_2. b) When a contact is established, charges flow from the low work function material to the high work function material and accumulate at the surfaces. This leads to the formation of a contact potential difference eV_{CPD}. c) The V_{CPD} is nullified by applying an equal, opposite bias V_{DC}.

3.2.3 Scanning Tunneling Microscopy/Spectroscopy

Another microscopy technique to obtain atomic resolution of objects is *scanning tunneling microscopy* (STM) [74]. It is based on the fact that electrons tend to tunnel from the sample surface to the tip through vacuum, if a bias is applied between sample and tip and their distance is very small. These tunneled electrons are measured as a current by the electronics and produce the feedback signal during a measurement. The distance between sample and tip is typically chosen in a way that attractive and repulsive forces acting on the tip compensate each other (r_m in Figure 16 a)). All STM measurements in this study were conducted in constant current mode, which means that the height at each measurement point is varied by a piezo in a way that a constant tunneling current is measured. In this way height images are obtained. By varying the applied bias at a certain measurement spot and measuring the change in current dI/dV, scanning tunneling spectroscopy (STS) spectra are obtained. In this way the local density of states can be measured, as the tunneling current is directly proportional to it.

4 Materials and Experimental Setup

4.1 Materials and Sample Preparation

4.1.1 Bilinear Arrays

For the measurements in section 5.1 samples with a stripe like pattern were produced. Large stripe sizes (500 µm and 250 µm) were produced by first flash evaporating aluminum on glass substrates out of a coil. Afterwards gold was evaporated on the aluminum using shadow masks (500-500 µm Au-Al and 250-200 µm Au-Al), usually used to obtain contact fingers for electrical measurements. Both evaporations were carried out with a base pressure of 10^{-6} mbar. The samples were exposed to air between the evaporations and afterwards.

Smaller stripe sizes (~2 µm) were obtained by microcontact printing, which was originally developed as an alternative technology to photolithography [75]. The process is schematically illustrated in Figure 18. A structured composite polydimethylsiloxane (h-PDMS [76,77]) stamp is immersed in a 0.1 mM solution of 1-hexadecanethiol (CSH) for 1 h. Then, the stamp is blown dry and manually brought into contact with a substrate comprising a thin evaporated Au film for 50 s. Only where the stamp is in contact with the substrate, CSH molecules diffuse from the stamp to the Au electrode and self-assemble. After detachment of the stamp the substrate was rinsed with ethanol, toluene and 2-propanol to remove any loosely attached molecules [78]. In a second step the remaining Au lines are backfilled by immersing the sample in a 10 mM solution of 1H,1H,2H,2H-perfluorodecanethiol (FSH) for 1 h [79]. Finally the samples were rinsed again in ethanol, toluene, 2-propanol and blown dry. This yields symmetric bilinear arrays. Asymmetric arrays were obtained by the same procedure, but using a longer stamping time of 10 min. This is most probably due to some diffusion of CSH [80–82].

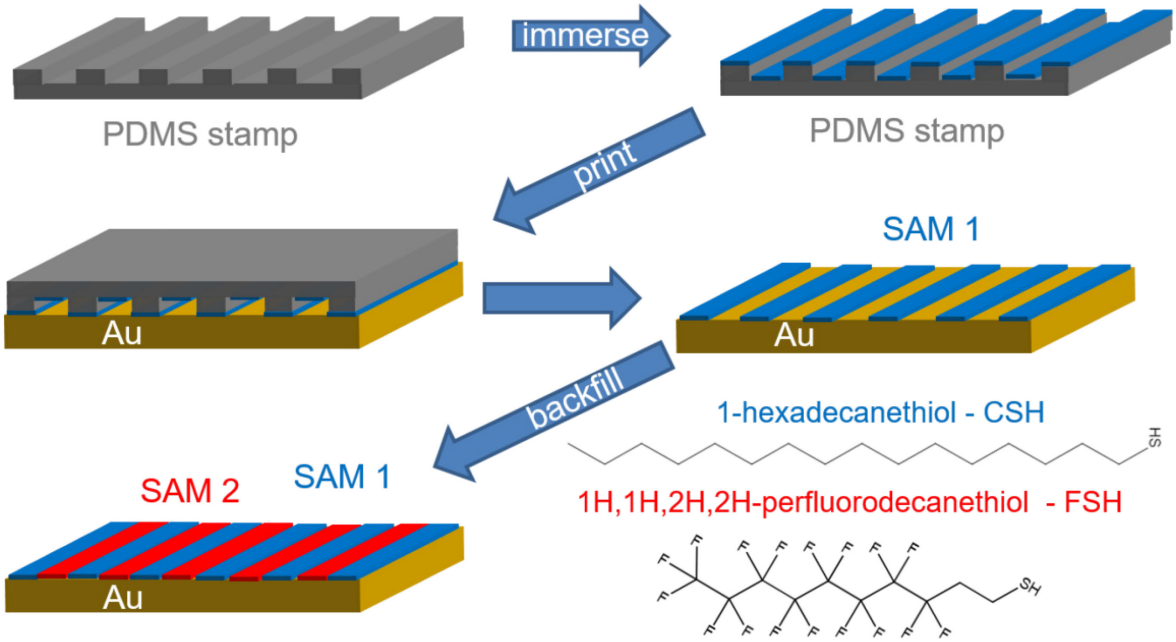

Figure 18: Schematic illustration of microcontact printing. The PDMS stamp is immersed in a solution of CSH and pressed on an Au substrate. Afterwards the remaining Au is backfilled by putting the sample in a solution of FSH.

4.1.2 Inorganic Semiconductors

Gallium Nitride

Gallium Nitride (GaN) is a group III-V inorganic semiconductor. In this work Ga-terminated (0001) samples were used, which were purchased from the company *Novagan* and grown by metal-organic chemical vapor deposition (MOCVD). GaN grows in a wurtzite structure with lattice parameters of $a = 3.18$ Å and $c = 5.18$ Å [83]. GaN is a direct semiconductor with a band gap of 3.4 eV at the Γ-point. Undoped and Mg-doped (p-type) samples were investigated in this thesis. The doping concentration was determined by electrochemical C-V measurements [84], conducted at the Ferdinand Braun Institute. Doping concentrations of $3 \cdot 10^{15}$ donors/cm^3 (undoped) and $1 \cdot 10^{19}$ acceptors/cm^3 (Mg-doped) were found, respectively.

To study and understand fundamental phenomena taking place at interfaces it is important that these interfaces are reasonably clean. Fortunately XPS is a superb technique for investigating the cleanness of surfaces. In this section the results of different cleaning procedures are demonstrated and compared.

In Figure 19 a) - d) the survey spectra and the O1s, C1s and Ga3d spectra for GaN samples, which were only cleaned ex-situ with acetone and isopropanol for 10 min each, are shown (black curves). It is obvious that the surface is covered by a lot of carbon and oxygen. Also the peaks are shifted to higher binding energies with comparison to literature [85–87], which is an indication for charging of the sample. Already after a mild annealing in vacuum at 500° C for 1 h the amount of carbon and oxygen is decreased and the peaks are shifted to lower binding energies (not shown). Further annealing did not remove the oxygen and carbon completely. Sputtering with argon, as already successfully applied for the cleaning of ZnO surfaces [88], was able to remove the carbon but did not significantly change the oxygen concentration. Furthermore it yielded a non-stoichiometric ratio of Ga to N of $n_{\mathrm{Ga}}/n_{\mathrm{N}} = 3/2$ due to preferential sputtering of nitrogen [85], because nitrogen atoms are always sputtered singly but Ga atoms are always sputtered in pairs with nitrogen [89]. The best preparation method was found to be according to Mishra et al. [90]. After ex-situ cleaning with acetone and isopropanol the samples were put in a 20% HCl-solution for 10 min. This breaks oxygen bonds and passivates the remaining dangling bonds with Cl. A three step in-situ annealing at 650 °C, 750 °C and 700 °C for 1 h, 1.5 h and 1 h, respectively, and additional sputtering with nitrogen (0.5 kV, $1 \cdot 10^{-5}$ mbar, 20 min) between the annealing steps yielded almost perfectly clean surfaces with good stoichiometry. The results are shown in Figure 19 a) – d) and summarized in e). The resulting surfaces showed also good order as determined by a hexagonal low energy electron diffraction (LEED) pattern.

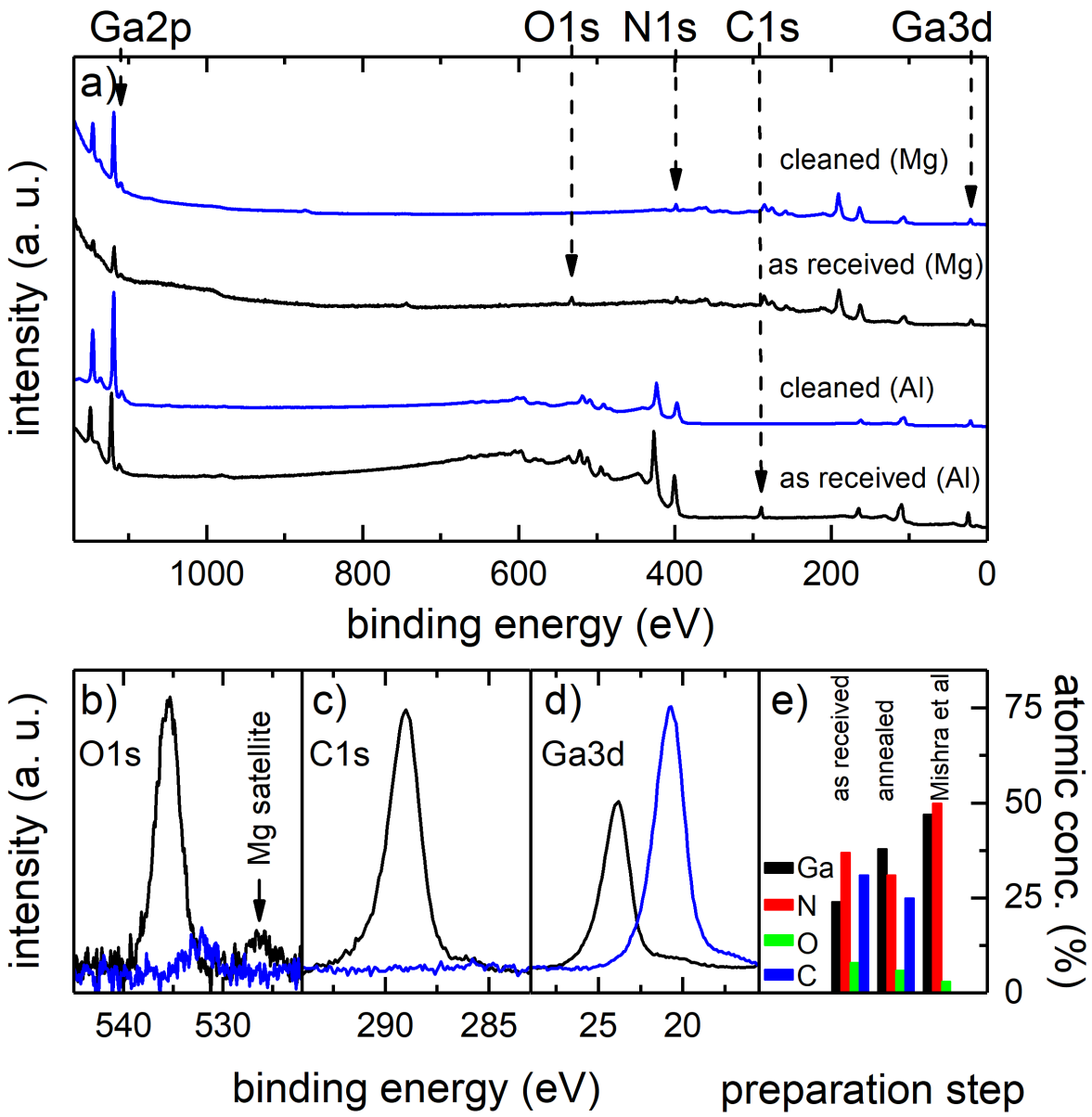

Figure 19: Overview of GaN cleaning processes. a) Survey spectra of just ex-situ treated samples and cleaned samples as described in the text recorded with aluminum and magnesium anode to consider Auger peaks. Important peaks used in this thesis are labeled. b)-d) show the O1s, C1s and Ga3d peaks, respectively. The peaks of the only ex-situ treated samples are rigidly shifted to higher binding energies, which is an indication for sample charging. After cleaning the C1s peak disappears, the O1s peak gets strongly attenuated and the Ga3d peak is amplified and shifted to lower binding energies. e) Summary of the elemental composition determined from XPS measurements for different preparations.

Zinc Oxide

Zinc oxide (ZnO) is, like GaN, a group III-V inorganic semiconductor. Its lattice constants ($a = 3.25$ Å and $c = 5.21$ Å [91]) and energy gap (3.3 eV [92]) are very similar to GaN. It was chosen in this study, because my colleague Sergey Sadovef was able to controllably grow Ga-doped ZnO $(000\bar{1})$ samples with a wide range of different donor concentrations by molecular beam epitaxy. With this it was possible to investigate the influence of the bulk doping concentration on the work function change upon acceptor deposition with doping concentrations ranging from 10^{17} cm^{-3} to high 10^{20} cm^{-3}. The samples were stored in a glovebox between growth and measurement and no surface treatment was employed before molecule deposition.

Silicon

Silicon is a widely studied material and commercially applied mainly in solar cells and computer electronics. It has an indirect band gap of 1.12 eV and grows in the diamond lattice structure with a lattice constant of $a = 5.4$ Å [13]. Due to advanced production techniques a very low residual doping concentration of down to 10^{13} cm^{-3} can be easily achieved. The samples used in this thesis were (111) cut, had a donor concentration of $10^{13} - 10^{14}$ cm^{-3} and were provided by the institute for silicon photovoltaics at the Helmholtz Zentrum Berlin. When silicon is stored under ambient conditions a natural oxide layer of SiO_2 forms. This needs to be removed and ideally substituted by a passivating hydrogen layer. Different cleaning procedures were tested to achieve this, which are presented in the following.

In Figure 20 a) the XPS survey spectrum of an as received sample is shown in black. Strong signals from oxygen and carbon can be observed. Also the presence of a peak at 103.5 eV binding energy, as can be seen in the Si2p narrow range spectrum in Figure 20 b), indicates the presence of a SiO_2 surface layer. This SiO_2 layer can be completely removed by treatment with both 5% HF and 40% NH_4F. However, the treatment with pure HF solution results in a rough, non-ordered surface as can be seen in the AFM image in Figure 20 c). A treatment with NH_4F and subsequent annealing on the other hand results in flat terraces with step heights of ~3 Å, corresponding to single Si atoms, as shown in the AFM image

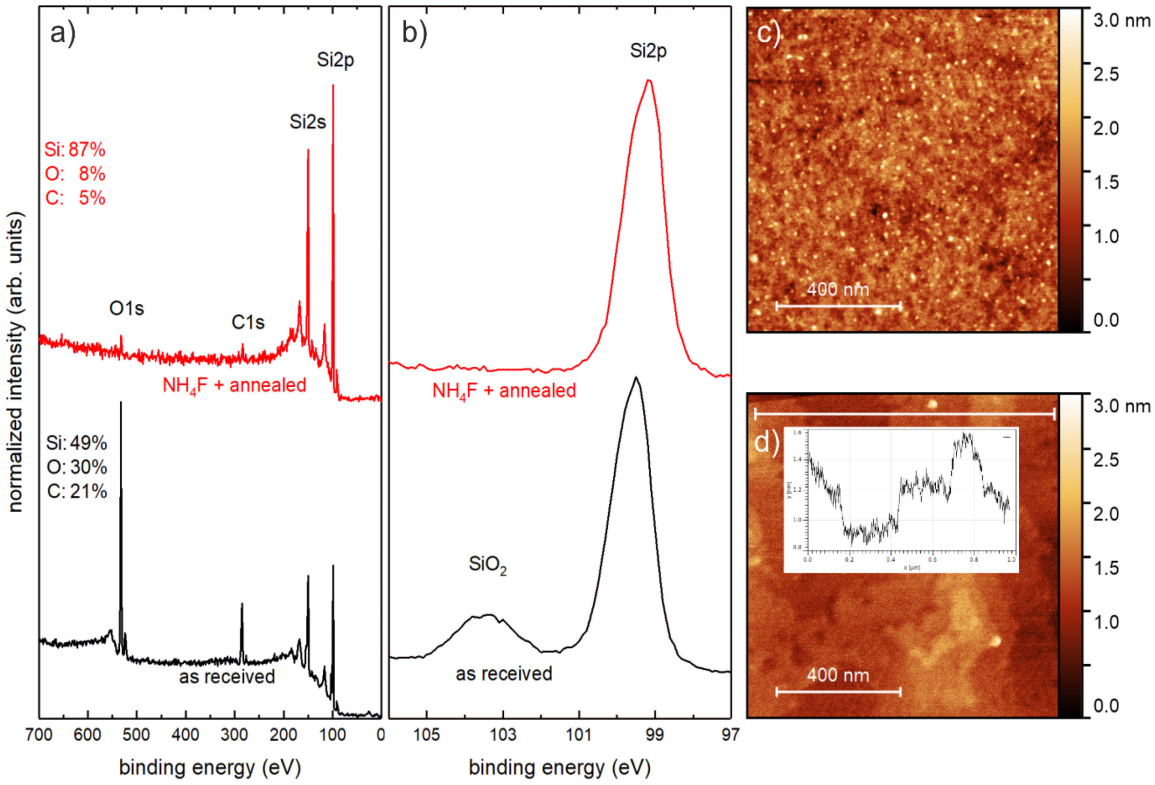

Figure 20: Overview of Si cleaning procedures. a) XPS survey scans of as received (black) and NH_4F treated and annealed (red) silicon. The carbon and oxygen contaminations are strongly reduced by the NH_4F+annealing treatment. b) Narrow scan of the Si2p region before (black) and after (red) preparation. The peak at 103.5 eV stems from a SiO_2 surface layer and is completely removed by the NH_4F treatment. c) AFM image of silicon cleaned by 5% HF, resulting in a rough surface. d) AFM image of silicon after NH_4F+annealing treatment, showing flat terraces with step heights of 3 Å.

in Figure 20 d). It also removes the surface oxide layer and most of the adventitious contaminations as can be seen in Figure 20 a) and b). A well-ordered Si:H (111) surface was confirmed by a strong hexagonal LEED pattern.

Tungsten Diselenide

Tungsten diselenide (WSe_2) in its bulk form is an inorganic, hexagonal semiconductor with an indirect band gap. Tungsten and selenium atoms within one planar layer are bound by strong covalent bonds, whereas different layers are only weakly bound by van der Waals forces. This is very common for transition metal dichalcogenides and makes it relatively easy to obtain 2-dimensional structures of these compounds. When reducing the dimensionality to a single layer, the band gap of WSe_2 changes from indirect to direct with a value of 1.6 eV [93], making it very promising for opto-electronic applications.

The WSe_2 samples investigated in this work were grown by chemical vapor deposition in the group of professor Li at KAUST University, using WO_3 powders as precursors. Samples used for STM measurements were directly grown on a graphite substrate to avoid contaminations during the mechanical transfer in air (coverage ≈ 10 %, as determined from STM measurements on different parts of the samples), whereas samples for PES measurements were first grown on sapphire as a large-scale WSe_2 film and afterwards transferred to a graphite substrate by a wet chemical method (coverage ≈ 80 %). All samples were degassed overnight at ≈ 450°C with base vacuum better than 10^{-9} mbar. This yields clean samples with a residual oxygen contamination of less than 1 %, as evidenced from the XPS survey shown in Figure 21 a). For electrical characterization a field effect transistor was built on a monolayer WSe_2 flake, using 300 nm SiO_2 on degenerately doped p-doped Si as a gate dielectric. The source and drain electrodes were made of Pd(20 nm)/Au(50 nm) and patterned on the WSe_2 flake by e-beam lithography. An optical image of the patterned contacts is shown in Figure 21 b). The electrical

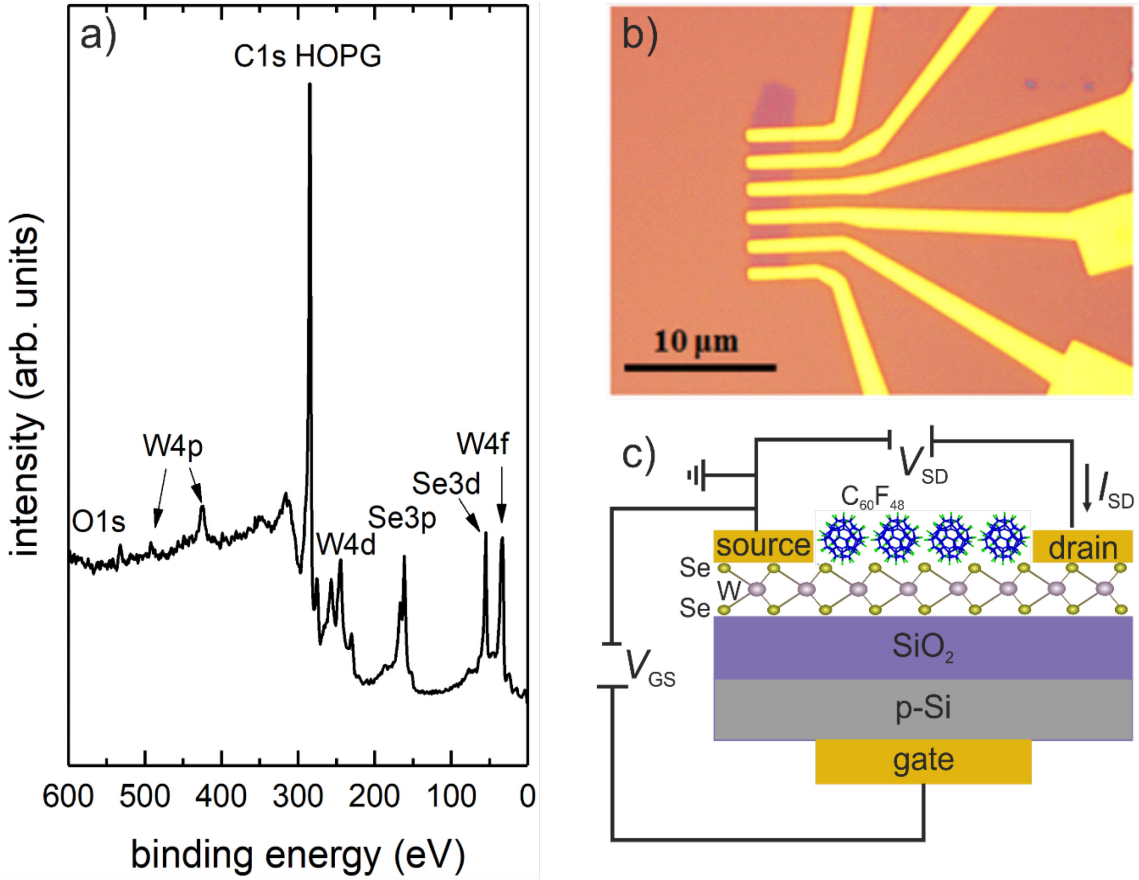

Figure 21: a) XPS survey spectrum of monolayer WSe_2 on HOPG after degassing over night at 450 °C. b) Optical image of the source-drain contacts to a WSe_2 monolayer flake, deposited by lithography (adapted from [94]). c) Scheme of a backgated field effect transistor configuration for WSe_2 on SiO_2/p-Si. $C_{60}F_{48}$ can be deposited on top of the WSe_2 flake after contact deposition.

characterizations were performed using an Agilent 2912A at room temperature and high vacuum ($\approx 10^{-8}$ mbar). After initial electrical characterization 20 nm of $C_{60}F_{48}$ were deposited on the already contacted WSe_2 flake and electrical characterization was repeated. A scheme of the field effect transistor structure is shown in Figure 21 c).

4.1.3 Organic Semiconductors

All organic semiconductors used in this work are shown in Figure 22. They can be divided in the following four categories

As *strong acceptor* molecules 2,2'-(perfluoronaphthalene-2,6-diylidene)dimalononitrile (F6-TCNNQ) and fluorinated fullerene ($C_{60}F_{48}$) were used. They have high electron affinities of 5.6 eV [94,95] and 5.2 eV [96], respectively, making them excellent electron acceptors. They also have comparably high molecular weights, making them less volatile and therefore device relevant.

As *strong donor* molecule $[RuCp^*(mes)]_2$ was used. After deposition on a surface the dimer breaks up in two monomers, which have an ionization energy of only 3.1 eV [97]. This is sufficiently low to achieve electron transfer to most materials.

As test molecule the commercially available and widely studied N,N′-Di(1-naphthyl)-N,N′-diphenyl-(1,1′-biphenyl)-4,4′-diamine (α-NPD), 4,4′-Bis(N-carbazolyl)-1,1′-biphenyl (CBP) and Fullerene (C_{60}) were used. Due to their large band gap they can be well used for investigating the subsequent energy level alignment after deposition of acceptor or donor molecules, without inducing significant charge transfer itself.

Self-assembled monolayers (SAMs) are closely packed assemblies of molecules, which form a densely packed, well ordered monolayer spontaneously after deposition on a surface. In this work two SAMs with a thiol anchor group, 1-hexadecanethiol (CSH) and 1H,1H,2H,2H-perfluorodecanethiol (FSH), were used. They possess oppositely orientated dipoles, leading to work function reduction (increase) after deposition on gold, respectively. Furthermore, they can be easily arranged in a patterned way by microcontact printing.

All molecules, except for the SAMs, were evaporated from resistively heated quartz crucibles in UHV and their thickness was controlled using a quartz crystal microbalance.

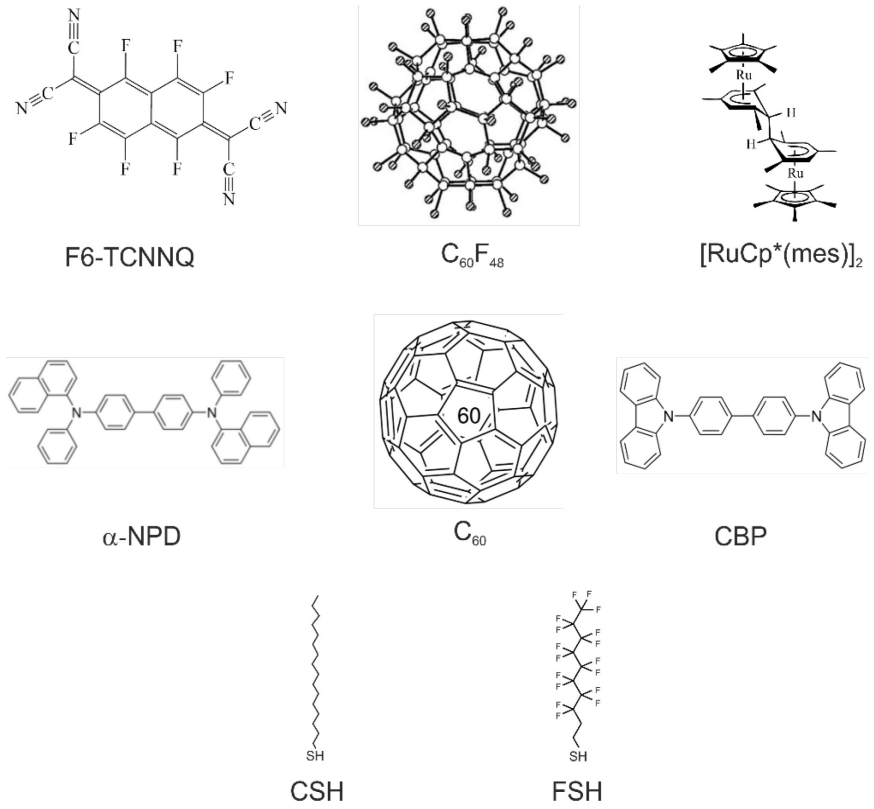

Figure 22: Molecular structure of all molecules used in this work. Acceptors (F6-TCNNQ, $C_{60}F_{48}$) were used to increase the substrate work function, whereas donors ($[RuCp^*(mes)]_2$) were used to decrease it. α-NPD, C_{60} and CBP were used as test molecules to verify the energy level alignment. Both SAMs (CSH and FSH) were used to change the work function of a gold substrate in a patterned way by microcontact printing.

4.2 Photoelectron Spectroscopy Setup

Most of the photoelectron spectroscopy measurements were conducted in the lab at the Humboldt Universität zu Berlin. The systems consists of an analysis chamber with a base pressure of $10^{-10} - 10^{-9}$ mbar, a preparation chamber with a base pressure of 10^{-9} mbar and a load lock for fast sample inward transfer. The preparation chamber can be equipped with up to three evaporators, one of them being externally pumped, enabling molecule exchange without braking the vacuum of the preparation chamber. Molecules are evaporated from resistively heated quartz crucibles.

The deposited thickness is determined by using a quartz crystal micro balance to measure the evaporation rate. A micro balance is based on an oscillating piezo crystal. If mass Δm is deposited on the crystal its resonance frequency f_0 changes by Δf according to the Sauerbrey equation, developed by G. Sauerbrey in 1959 [98]:

$$\Delta f = -\frac{2f_0}{A\sqrt{\rho_q \mu_q}} \Delta m. \tag{43}$$

Here A is the piezoelectrically active crystal area, ρ_q is the density of the quartz (2.648 g/cm^3) and μ_q is the shear modulus of the quartz ($2.947 \cdot 10^{11}$ g·cm^{-1}·s^{-2}). By knowing the density of the deposited material the change in mass can be converted to an equivalent film thickness, with detection sensitivities down to the sub-angstrom regime. However, it has to be kept in mind that not all organic materials grow in a layer-by-layer mode. Therefore the measured thickness can usually only be considered as a nominal thickness.

Furthermore, the preparation chamber is equipped with a sputter gun, which can be operated with different sputter gases, like argon or nitrogen. Also the manipulator can be resistively heated up to 750 °C.

As x-ray photon sources a magnesium and an aluminum anode are available, providing excitation energies of 1253.6 eV and 1486.6 eV, respectively. The FWHMs of the sources are 0.70 eV and 0.85 eV, respectively [99]. For UPS measurements, a He excitation lamp is used with an energy of 21.21 eV. The FWHM of the He lamp is typically below 10 meV, therefore broadening due to the UPS excitation source can be neglected. The He light can be attenuated with Al-filters to avoid damaging of sensitive organic samples. The analysis

chambers are equipped with hemispherical energy analyzers. The energy resolution of the analyzers can be determined by measuring the Fermi-edge of a polycrystalline metal sample, e.g. gold. The data are fitted with a convolution of a Fermi-function at room temperature and a Gaussian function. The analyzer resolution can then directly be determined by the width of the Gaussian function. This is exemplarily shown in Figure 23 for a pass energy of 10 eV. From the width of the Gaussian function the broadening due to the analyzer can be determined to be 167 meV. The Fermi-function at room temperature is shown in red for comparison. It can further be seen that the center of the measured Fermi-distribution is shifted by +25 meV with respect to zero binding energy. This means that the analyzer work function needs to be corrected by this value.

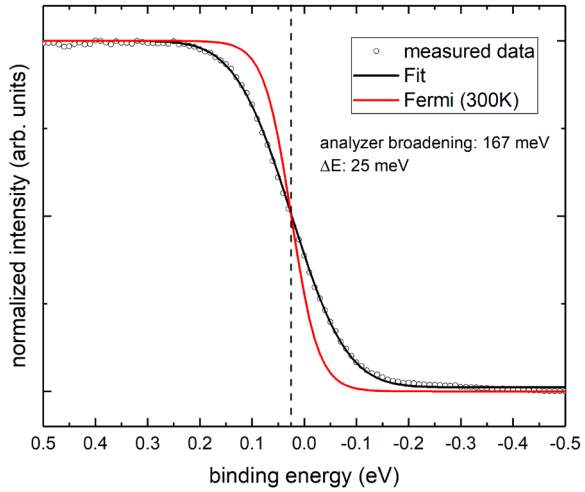

Figure 23: Fermi-edge of a sputter cleaned polycrystalline Au sample measured by UPS, using a pass energy of 10 eV. The data were fitted by a convolution of a Fermi-function at room temperature with a Gaussian function (black). The width of the Gaussian function gives the broadening due to the analyzer, which is 167 meV. It can further be seen that the analyzer work function needs to be corrected by 25 meV, as the center of the Fermi-distribution is not at zero binding energy. A Fermi-function at room temperature is shown for comparison (red).

Distinguishing between interface dipole formation and band bending

For the discussion in section 5.2 it is important to know how to distinguish between changes in band bending inside the inorganic semiconductor $\Delta\Phi_{BB}$ and an interface dipole between the inorganic semiconductor and the organic semiconductor $\Delta\Phi_{ID}$. Both contribute to the overall work function shift $\Delta\Phi$

$$\Delta\Phi = \Delta\Phi_{BB} + \Delta\Phi_{ID} \tag{44}$$

and can be measured separately by combining XPS and UPS measurements. The different contributions to the work function change are illustrated in Figure 24 a) and the measurement principle of the different contributions is shown in Figure 24 b). A shift of the SECO in UPS allows a direct determination of the overall work function change. While an interface dipole would not affect the energetic position of the inorganic semiconductor core levels, a change in band bending can be directly determined from a shift of the core level positions (preconditioned charging and chemical shifts can be ruled out). Care must be taken, as the change in potential due to band bending depends on the spatial position inside the inorganic semiconductor. Since electrons from different core levels have different kinetic energy, also their mean free path and with this the sampled depth is different (see Figure 11). For the determination of maximum changes in band bending, measuring core levels with low kinetic energy is recommended, as this yields a maximum surface sensitivity. The interface dipole can then be determined from $\Delta\Phi - \Delta\Phi_{BB}$.

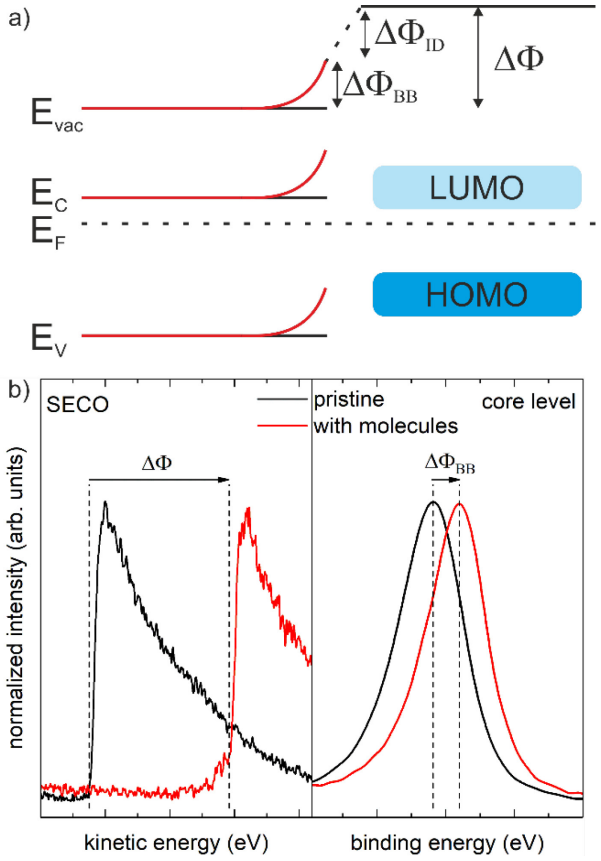

Figure 24: Schematic illustration of the different contributions to the work function change $\Delta\Phi$ of an inorganic semiconductor after deposition of organic acceptor molecules. a) The electron transfer can induce band bending changes inside the inorganic semiconductor $\Delta\Phi_{BB}$ and lead to the formation of an interface dipole $\Delta\Phi_{ID}$ between the inorganic semiconductor and the molecules. b) Measurement principle for the different work function contributions. The overall work function change $\Delta\Phi$ can be determined from the shift of the SECO in UPS after molecule adsorption. Changes in band bending $\Delta\Phi_{BB}$ can be estimated from the shift in the core levels of the inorganic semiconductor. The interface dipole contribution $\Delta\Phi_{ID}$ is then determined as the difference between the two measured quantities. Adapted from [100].

4.3 Scanning Probe Microscopy

Atomic Force Microscopy (AFM)

For the AFM measurements a Dimension Icon by *Bruker* was used. For all topography scans the ScanAsyst mode was used. This mode ensures best image quality by constantly monitoring the measurement and automatically readjusting measurement parameters like setpoint, feedback gains or scan rate. For all measurements ScanAsyst-air tips were used. They consist of a silicon nitride cantilever with reflective aluminum back side coating and the tip has a nominal radius of 2 nm.

Kelvin-Probe Force Microscopy (KPFM)

KPFM measurements were conducted using the same setup by *Bruker* as for AFM measurements. The measurement mode used was PeakForce KPFM, which is a combination of Peak Force Tapping mode and frequency modulated KPFM. For all KPFM measurements SCM-PIT tips were used. The tip and cantilever are coated with platinum-iridium to ensure good electrical conductivity and to improve laser reflectivity. The tip has a nominal radius of 20 nm. If not stated otherwise, a lift height of 60 nm was used.

Scanning Tunneling Microscopy/Spectroscopy (STM/STS)

The STM/STS studies were performed at the National University of Singapore, using an Omicron high-resolution STM interfaced to a Nanonis controller. Tungsten tips were electrochemically etched and the bias was applied to the tip, while keeping the sample grounded. All STM images were recorded in constant current mode, using a tunneling current of about 0.05 nA. The dI/dV spectra of the STS measurements were recorded using a lock-in amplifier with a modulation of 625 Hz and 40 mV. All measurements were conducted at 77 K in UHV.

5 Results and Discussion

In this chapter the results of this dissertation will be presented and discussed. It consists of three sections. The first section is about work function measurements on heterogeneous surfaces with UPS. The mechanisms leading to multiple cut-offs and work function averaging are unraveled and the *spatial resolution* of UPS work function measurements in dependence of the measurement parameters is determined. Furthermore it is shown how these findings influence the ionization energy determination of molecules deposited on heterogeneous substrates. Part of these results were published in [100,101].

The second section deals with the energy level alignment at hybrid inorganic/organic semiconductor interfaces (HIOS). The dependence of band bending and interface dipole on the surface state density of the inorganic semiconductor is discussed using the example of GaN and the organic acceptor F6-TCNNQ. The dependence on the bulk doping concentration is investigated with differently doped ZnO samples and the organic acceptor F6-TCNNQ. Furthermore the full range of energy level tuning with the help of organic interlayers is demonstrated using GaN and Si, organic acceptor or donor interlayers and the commercially used organic semiconductor α-NPD. Parts of these results were or are going to be published in [102–104].

The last section covers the growth and energy level alignment at the interface between the 2D transition metal dichalcogenide (TMDC) WSe_2 and the organic acceptor molecules $C_{60}F_{48}$. By combining STM/STS, PES and DFT X the mechanisms leading to the observed energy level changes are unraveled. Parts of the results were published in [105].

5.1 The Role of Electrostatic Potentials for Ultraviolet Photoelectron Spectroscopy Work Function Measurements

Ultraviolet photoelectron spectroscopy (UPS) is one of the primary techniques to determine the work function of surfaces nowadays. According to review articles [106,107] or textbooks [57,108–110], heterogeneous surfaces are expected to exhibit one secondary electron cut-off (SECO) representing an averaged sample work function. However, it is never explained in detail what are the underlying mechanisms responsible for this averaging effect to take place and up to which length-scale in terms of heterogeneity this averaging effect actually occurs. Also, a vast number of reports has shown that more than one cut-off can be observed for heterogeneous surfaces [111–113], but only very few address this issue directly [114,115]. To clarify this issue, a heterogeneous model system consisting of bilinear arrays of two self-assembled monolayers (SAMs), providing a periodic work function pattern with a difference of more than 1 eV, is investigated. With UPS two SECOs are measured, one reflecting the high work function material and the other a spatially averaged work function. To explain these observations, the electrostatic potential above the surface is further investigated by Kelvin-Probe Force Microscopy (KPFM) and compared to quantitative electrostatic modeling. It is shown quantitatively that the electrostatic potential from the high work function areas leads to an additional energy barrier for the electrons emitted from the low work function areas. Furthermore the influence of applied bias and spatial periodicity on the averaging effect is explored. It is finally demonstrated how this averaging phenomenon influences the determination of the ionization energy of molecular films evaporated on heterogeneous substrates. It should be mentioned here that other techniques, like photoelectron and X-ray emission (PAX), microspot UPS or PEEM, have been used before to investigate the microscopic origin of local work function differences [116,117].

5.1.1 KPFM and UPS Results

Prior to the UPS measurements, reference KPFM measurements were performed on the bilinear systems in order to assess locally the work function difference between the CSH and FSH stripes as well as the periodicity of the SAMs pattern. Due to slightly different preparation conditions (stamping time), the width of the stripes for both FSH and CSH are found to be equal (symmetric pattern) or unequal (asymmetric pattern), CSH stripe width being larger in this case. The potential map as well as the topography of 2 µm symmetrically and asymmetrically patterned samples are shown in Figure 25. The sharpness of the work function transition can be clearly seen in the line profile corresponding to the CPD map, demonstrating the reliability of the stamping process. As seen in Figure 25 b) and f), a large work function difference between CSH and FSH regions of 1.2 eV is achieved for both symmetric and asymmetric patterns. The CSH/FSH area ratio is ≈ 1 for the symmetric pattern and $\approx 5/3$ for the asymmetric pattern. The height difference is less than 1 nm for the two different SAMs, in good agreement with literature [118]. This proves the formation of actual monolayers (i.e. multilayer free samples) and minimizes topography crosstalk in the KPFM measurements [119]. Note that the samples were sufficiently stable for the course of the different experiments, yielding the same KPFM results after being stored for months in a nitrogen-filled glovebox.

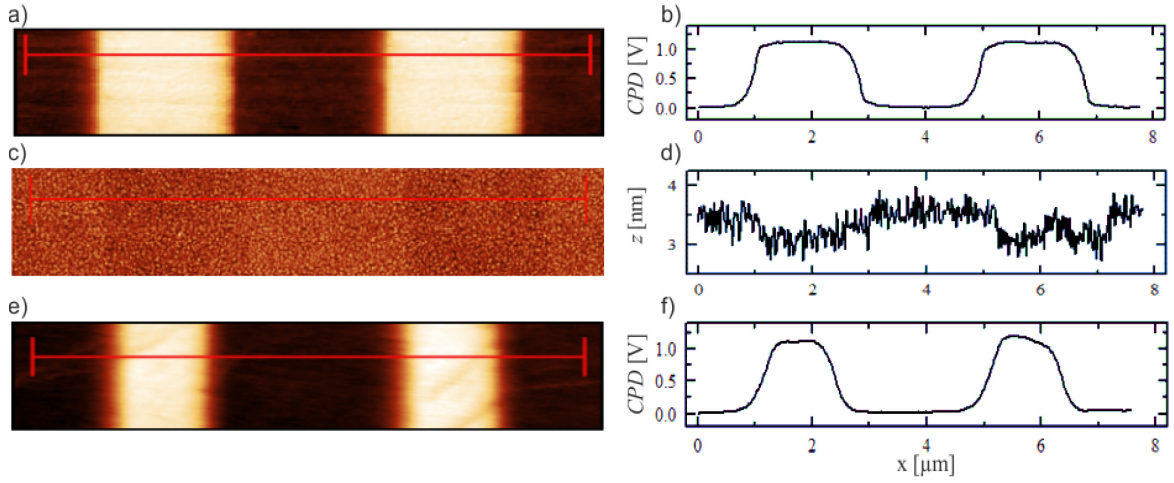

Figure 25: KPFM and AFM results of the patterned samples. a) and b) show the potential map and a cross section of the contact potential difference for a symmetric 2 µm pattern. Bright regions correspond to FSH, dark regions to CSH. c) and d) show the corresponding topography, indicating almost no height difference for the two different SAMs. e) and f) show the potential map and corresponding cross section for an asymmetric 2 µm pattern, indicating a CSH/FSH ratio of $\approx 5/3$. The CPD of CSH was set to zero for comparison. Adapted from [101].

The UPS results for the pristine SAMs on gold (solution grown) can be seen in Figure 26 a). The SECO of pristine CSH on gold (blue) is found at 4.35 eV and that of pristine FSH on gold (red) is at 5.45 eV, yielding an energy difference of 1.1 eV, in good agreement with the CPD difference obtained from KPFM measurements on the striped samples. The intensity of the CSH SECO is much higher compared to that of FSH, due to the lower CSH work function and since the number of secondary electrons increases exponentially with decreasing kinetic energy [120,121]. In Figure 26 b) the SECO spectra of the striped samples are shown. Besides a clear cut-off at 4.85 eV and 4.7 eV for both symmetric and asymmetric samples, respectively, an additional shoulder with a maximum at around 5.6 eV can be observed for both samples. The shoulder at higher kinetic energies is only present as a small bump, which is due to the before mentioned exponential dependence of the SECO intensity on the kinetic energy. Note that when looking at SECO spectra in literature, rather similar features at higher kinetic energies can often be observed but are mostly overlooked due to their lower intensity [115]. It must be kept in mind that the intensity is not directly related to the area coverage, due to the exponential dependence of the number of secondary electrons on the kinetic energy mentioned above.

To determine the onset of the cut-off at higher kinetic energy, the SECO spectra were fitted with an adaption of an empirical function suggested by Ogawa *et al.* [122], which consists of a convolution ($*$) of a Heaviside step-function (H, to account for the steep increase in

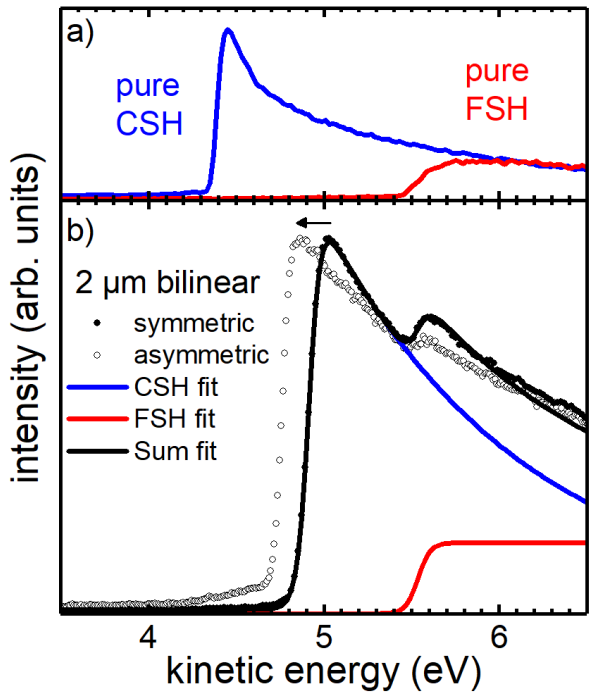

Figure 26: UPS measurements of SAM covered Au samples. a) Reference measurements on solution grown SAMs. CSH shows a cut-off at 4.35 eV and FSH shows a cut-off at 5.45 eV. The FSH intensity is much lower than the CSH intensity. b) SECO spectra of symmetric and asymmetric patterned samples, including fits to the symmetric sample according to equation (45). The FSH cut-off is visible as a small bump at the same energy as for the solution grown FSH reference. The low energy cut-off is shifted to higher kinetic energies compared to the bulk CSH reference due to an averaging effect. Its position depends on the CSH/FSH area ratio and is at 4.85 eV for the symmetric pattern and 4.70 eV for the asymmetric pattern, respectively. Adapted from [101].

intensity) with a Gaussian function (G, to account for thermal and experimental broadening). A multiplication with an exponential function $e^{-\alpha E}$ was added to account for the decrease of intensity with increasing kinetic energy. The SECO spectra can then be fitted by a sum of functions of the form:

$$I_{SECO} \sim H(E - E_0) * G(E) \cdot e^{-\alpha E}. \quad (45)$$

This is shown exemplarily in Figure 26 b) for the symmetric structure. The measured data can be well reproduced by a sum of two contributions, shown as red and blue curve in Figure 26 b). The work functions are then determined in the usual way, by fitting a linear function to the steep onset of the individual SECO components and taking the intersection with the energy axis. The high work function component of the striped samples is 5.5 eV, in good agreement with the work function of pristine FSH. The main cut-off at lower kinetic energies, however, is shifted to higher kinetic energies compared to the pristine CSH. Its onset is at 4.85 eV for the symmetric pattern and 4.70 eV for the asymmetric pattern, respectively, while it was found at 4.35 eV for the corresponding pristine CSH film. This clearly indicates an averaging effect, which only affects the SECO emerging from the low work function material and which seems to depend on the covered surface area. To understand this phenomena the electrostatic potential above such a bilinear patterned surface is investigated, both experimentally and theoretically, in the next section.

5.1.2 Electrostatic Potential Above a Bilinear Patterned Surface

As the work function difference directly at the surface is the same for bulk and patterned samples, as evidenced by KPFM measurements, the difference in the UPS measurements must originate somewhere between the sample surface and the analyzer, where the kinetic energy of the incoming electrons is measured. In this section the potential distribution above the surface is investigated experimentally and theoretically by means of KPFM and electrostatic calculations in order to determine the influence of the electrostatic potential on the photoelectrons in a UPS experiments.

The UPS SECO provides a measure of the kinetic energy of the secondary electrons, but does not provide a detailed picture of the potential landscape. In order to locally determine the electrostatic potential above the sample surface, a series of KPFM measurements with varying tip-sample distance was performed, going from 50 nm to 1200 nm. For the symmetric array, the corresponding potential line profiles are displayed as a contour plot

in Figure 27 (left panel), in which the x-axis represents the direction perpendicular to the orientation of the array and the y-axis corresponds to the tip-sample distance. Note that in this graph the average of each measured line profile potential was set to zero for enabling direct comparison with electrostatic calculations. The lateral positions of 4 µm, 0 µm and -4 µm correspond to the middle of CSH stripes and therefore, at small tip-sample distances, the measured potential is dominated by the CSH SAM stripes positioned below, while at the lateral positions of -2 µm and +2 µm the FSH SAM stripes dominate the measured potential. The potential difference between CSH and FSH measured for relatively small lift heights (typically below ca. 50 nm) corresponds to the potential difference as determined for very small tip-sample distances. However, with increasing tip-sample distance the measured potential difference between CSH and FSH approaches zero above the whole sample surface. For instance, for a tip-sample distance of 1 µm the determined potential difference between CSH and FSH decreased to ca. 200 meV. This potential mapping can now serve as benchmark measurement for theoretically modeling the electrostatic potential φ, which is calculated above a periodic arrangement of stripes with a potential difference of 1.2 eV, as determined from KPFM measurements at smallest low tip-sample distance, by solving the Laplace equation:

$$\Delta\varphi(x,z) = 0 \tag{46}$$

Here Δ is the Laplace operator in Cartesian coordinates. The y-component can be neglected due to the one dimensional periodicity of the system. The periodicity L and the area ratio η between the different potentials lead to the following mixed boundary conditions:

$$\varphi(x,0) = pulse_{L,\eta,\Delta\Phi}(x), \tag{47}$$

$$\lim_{z\to\infty} \frac{\partial\varphi(x,z)}{\partial z} = 0, \tag{48}$$

where $pulse_{L,\eta,\Delta\Phi}(x)$ is a pulse function with a height ΔΦ equal to the work function difference between the two SAMs (1.2 eV). A demonstrative illustration of all the parameters is shown in Fig. 1 a) in the Appendix. Equation (47) determines the boundary condition directly at the surface, whereas equation (48) ensures that the electric field vanishes far away from the surface. This set of equations (46)-(48) is analytically solvable and yields the following result for the potential $\varphi(x,z)$:

$$\varphi(x,z) = \Delta\Phi{\cdot}\eta + \sum_{n=1}^{\infty} \frac{2\Delta\Phi}{n\pi} \cdot \sin(n\pi\eta) \cdot \cos\left(2\pi n \frac{x}{L}\right) \cdot e^{-2\pi n \frac{z}{L}} \qquad (49)$$

A detailed derivation of equation (49) can be found in Appendix A). The resulting calculated potential is presented in Figure 27 (right panel) and is in excellent agreement with the potential landscape obtained by KPFM. Specifically, it suggests that the potential far away from the surface converges to an (area) averaged value of the surface potentials above the CSH and FSH stripes. For the UPS measurements of the symmetric array, this value corresponds to a work function of $\frac{1}{2} \cdot (\Phi_{CSH} + \Phi_{FSH}) = 4.9$ eV, in good agreement with the experimentally observed SECO (Figure 26). Theoretically, this means that a secondary electron with energy between 4.4 eV and 4.9 eV could in principle escape the surface via the regions of CSH-covered Au. However, this secondary electron will not be able to fully overcome the potential barrier above the surface and thus cannot reach the analyzer. This is made even clearer in Figure 28 a), where the potential is plotted as a function of the distance normal to the sample surface and above the center of CSH (blue) and FSH (red) stripes with 2 µm width.

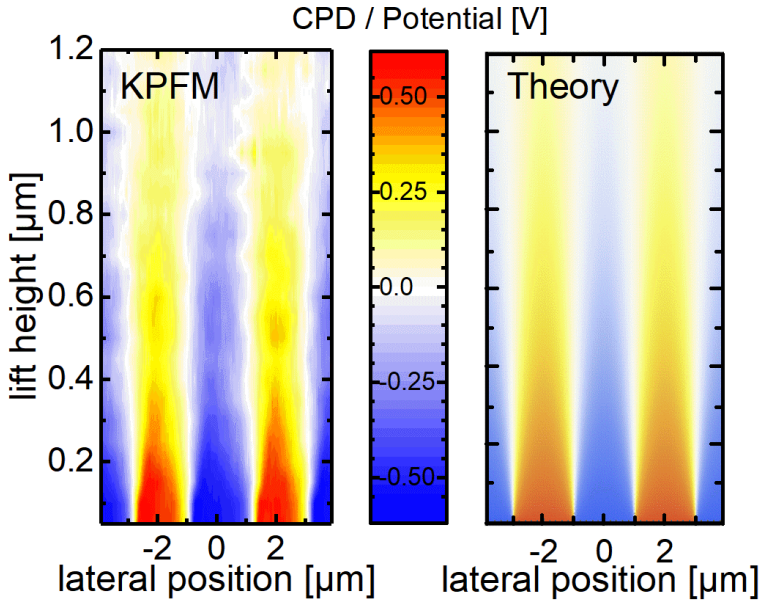

Figure 27: Comparison of potentials obtained by KPFM and from calculations. Left panel shows the electrostatic potential of a 2 µm symmetric patterned SAM sample measured by KPFM by performing line scans with different lift heights. The average of each line was subtracted for comparison with theory. The right panel shows the calculated potential above such a surface obtained by solving equation (45). Both results are in excellent agreement. Adapted from [101].

While the potential above the FSH stripes has its maximum directly at the surface and decreases further away from it, the potential above the CSH stripes further increases away from the surface. The immediate presence of the high work function material leads to the formation of an additional barrier $\Delta\Phi_{CSH}$ above the CSH stripes, which increases the measured work function. This barrier amounts to 0.6 eV for the symmetric stripes and 0.45 eV for the asymmetric stripes. The dashed lines in Figure 28 a) show the potential for an asymmetric pattern as used for the measurements shown in Figure 26 b) ($CSH/FSH = 5/3$). The calculated difference of the potential barrier $\Delta\Phi_{CSH}$ between the symmetric and asymmetric pattern of 150 meV is in excellent agreement with the experimental difference of 146 meV obtained from the SECO spectra (Figure 26 b)). One interesting question that arises is how this averaging behavior changes with varying periodic feature length-scale. Having demonstrated the good agreement between the electrostatic calculations and the experimental results, one can now investigate theoretically the amplitude of the potential barrier for varying feature length-scales. Surprisingly, the resulting potential barrier obtained from solving equation (49) is found to be completely independent of the stripe

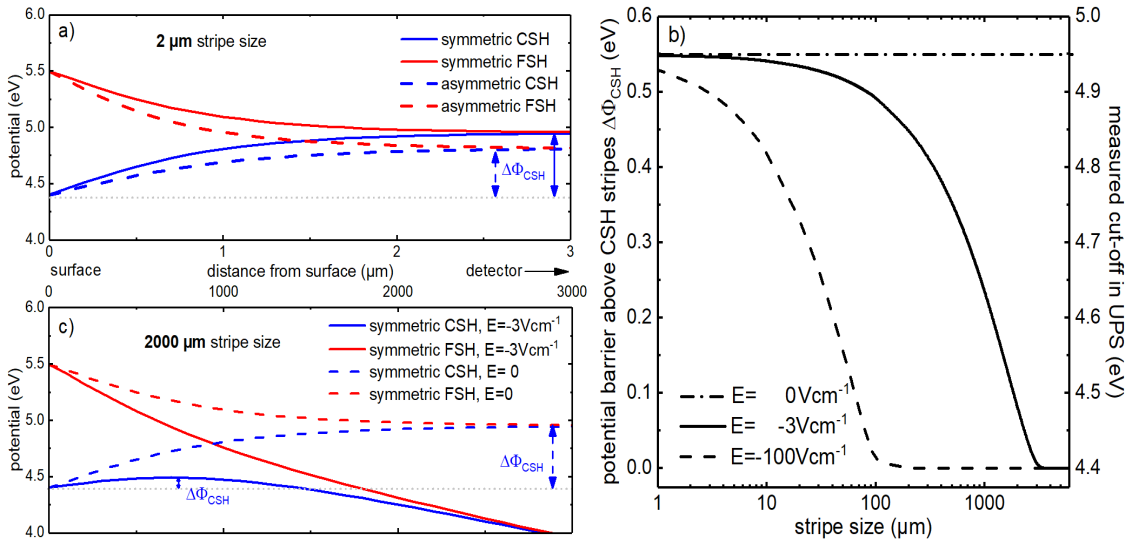

Figure 28: Results of the theoretically calculated potential above the striped surfaces. a) Potential perpendicular above the CSH (blue) and FSH (red) stripes as a function of distance from the surface for 2 µm symmetric (solid lines) and asymmetric (dashed lines, $CSH/FSH = 5/3$) SAM stripes. It can be seen that the potential barrier above the CSH $\Delta\Phi_{CSH}$ depends on the CSH/FSH area ratio. b) Calculated dependence of $\Delta\Phi_{CSH}$ on the stripe size without an applied electric field and two different field strengths. Without an additionally applied electric field, $\Delta\Phi_{CSH}$ is independent of stripe size. An averaging effect is present even for large stripe sizes ($\approx$ 2 mm). c) Potential above the different SAMs for 2 mm stripe size. The effect of an applied field (dashed and solid lines) on $\Delta\Phi_{CSH}$ is obvious when compared to no applied field (dash-dotted line). Adapted from [101].

size, as shown in Figure 28 b) (dash-dotted line). Since one would certainly not expect that an averaging effect takes place on a *macroscopic* scale (e.g. $L \geq 1$ cm), there must be something missing in the derivation of equation (49) in order to compare to actual UPS experiments. As mentioned already in section 3.1, a bias of a few volts is usually applied between the sample and the analyzer for work function measurements in UPS, in order to make sure that the secondary electrons can overcome the work function of the analyzer. As shown qualitatively by Helander et al [114], this bias results in an electric field, which will alter the potential landscape between the sample surface and the analyzer. To take this into account in the calculations, the boundary condition in equation (48) needs to be refined to:

$$\varphi(x, d) = \Delta V \tag{50}$$

Here ΔV is the applied bias between sample and analyzer, positioned at a distance d from the sample surface. Solving equations (46), (47) and (50) results in the following formula for the potential $\varphi(x, z)$:

$$\varphi(x, z) = \Delta\Phi{\cdot}\eta + \frac{\Delta V}{d} z + \sum_{n=0}^{\infty} \frac{2\Delta\Phi}{n\pi} \sin(n\pi\eta) \cdot \cos\left(2\pi n \frac{x}{L}\right) \cdot \frac{\sinh\left(2\pi n \frac{(d-z)}{L}\right)}{\sinh\left(2\pi n \frac{d}{L}\right)} \tag{51}$$

A detailed derivation of equation (51) can be found in Appendix A). The resulting potential, including a bias of -10 V and a sample/analyzer distance of 3.5 cm, as used in the experiments, is presented in Figure 28 c) (here with 2 mm stripe size). One can clearly see that the applied electric field strongly impacts the potential and decreases the additional barrier (involved in the averaging effect) above the CSH stripe down to $\Delta\Phi_{CSH} \approx 0.1$ eV, as compared to the sample with 2 µm stripe size in Figure 28 a), where this additional potential barrier amounts to 0.55 eV. This would correspond to a reduction of the averaging effect and a shift of the low kinetic energy SECO to 4.5 eV. The barrier above the CSH stripes as a function of the stripe width (for symmetric samples) is shown in Figure 28 b) for two applied electric fields of -3 and -100 V/cm as solid and dashed lines, respectively. With an applied field, the curves exhibit three regions, as exemplarily discussed for an electric field of -3 Vcm^{-1} (solid line) in the following: 1) For stripe sizes larger than 3 mm, the applied electric field completely compensates the emergence of the potential barrier $\Delta\Phi_{CSH}$ above the CSH stripes, leading to a SECO at 4.4 eV in a UPS spectrum (corresponding to pristine CSH work function). 2) For decreasing stripe size down to ca.

10 µm, the influence of the potential landscape emerging from the striped structure becomes increasingly important, leading to the formation of the potential barrier $\Delta\Phi_{CSH}$, which would shift the low kinetic energy SECO to higher kinetic energies. 3) Below 10 µm, the potential barrier $\Delta\Phi_{CSH}$ has reached saturation and the work function, as measured in UPS, corresponds to the spatially averaged work function, amounting to 4.9 eV. For larger electric fields, the influence of the potential landscape on the measured work function in UPS becomes significant only for smaller stripe widths, e.g. averaging only starts below 100 µm for an electric field of 100 Vcm^{-1} as depicted in Figure 28 b) (dashed line). These calculations suggest that the measurement parameters, like applied bias and sample/analyzer distance, should have an effect on the lateral averaging.

To demonstrate the influence of the applied electric field on the measured work function experimentally, bilinear arrays with either 500-500 µm or 250-200 µm stripe width were fabricated by evaporating gold on aluminum through shadow masks (see section 4.1.1). Such large stripe sizes are indeed needed to clearly observe the influence of the applied bias (in the range of bias which can be applied to the sample in the experimental set-up) on the measured SECO (compare Figure 28 b)). The work function of the pristine materials were determined to be $\Phi_{Au} = 4.50$ eV and $\Phi_{Al} = 3.55$ eV after air exposure, in good agreement with the 0.95 eV work function difference as determined by KPFM on the striped samples, shown in Figure 29 for a 250/200 µm striped Au/Al structure.

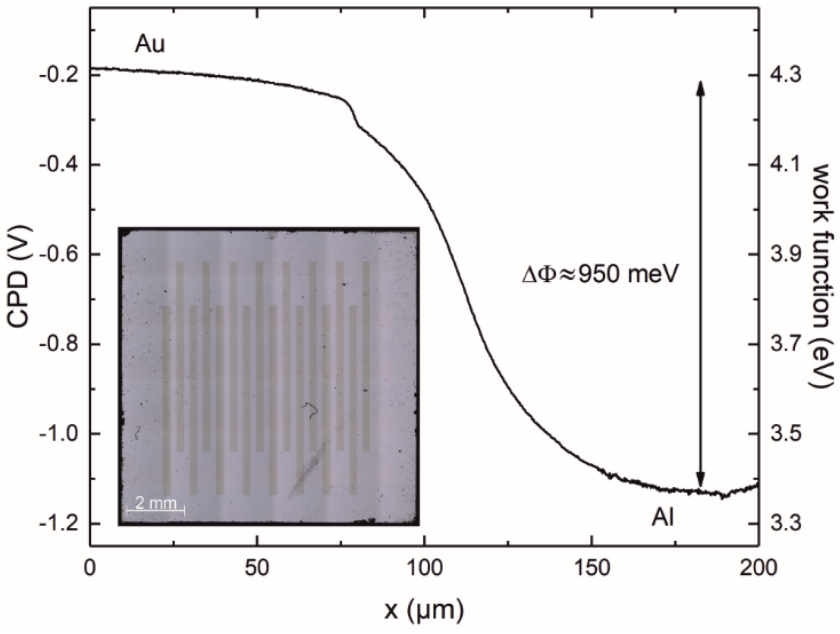

Figure 29: KPFM results of 250/200 µm Au/Al stripes transition region. The maximum work function difference of Au and Al regions amounts to ca. 950 meV. The inset shows an optical image of the whole sample. Adapted from [102].

Selected SECO spectra of the 500-500 µm sample are shown exemplarily for three different biases in Figure 30 a). It can be seen that, as for the CSH/FSH samples, each spectrum consists of two SECOs at ≈ 4.5 eV and ≈ 3.8 eV due to gold and aluminum, respectively. When increasing the bias, the aluminum-related SECO shifts to lower kinetic energies (after subtraction of the applied bias), while the gold-related SECO remains markedly at constant energy, i.e. the difference in the apparent work function between the two materials is bias-dependent. More precisely, this indicates a reduction of the additional potential barrier $\Delta\Phi_{Al}$ (in analogy to $\Delta\Phi_{CSH}$ in Figure 28 c)) above the aluminum stripes for increasing external electric field. A summary of the measured aluminum SECO shifts (due to changes in $\Delta\Phi_{Al}$) as a function of applied bias is shown in Figure 30 b) for 500-500 and 250-200 µm striped Au-Al samples. As further displayed in this figure, the change of the potential barrier, as calculated from equation (51), is in excellent agreement with the experimental results. This clearly demonstrates the influence of the applied bias on the SECO measurements by UPS on heterogeneous surfaces.

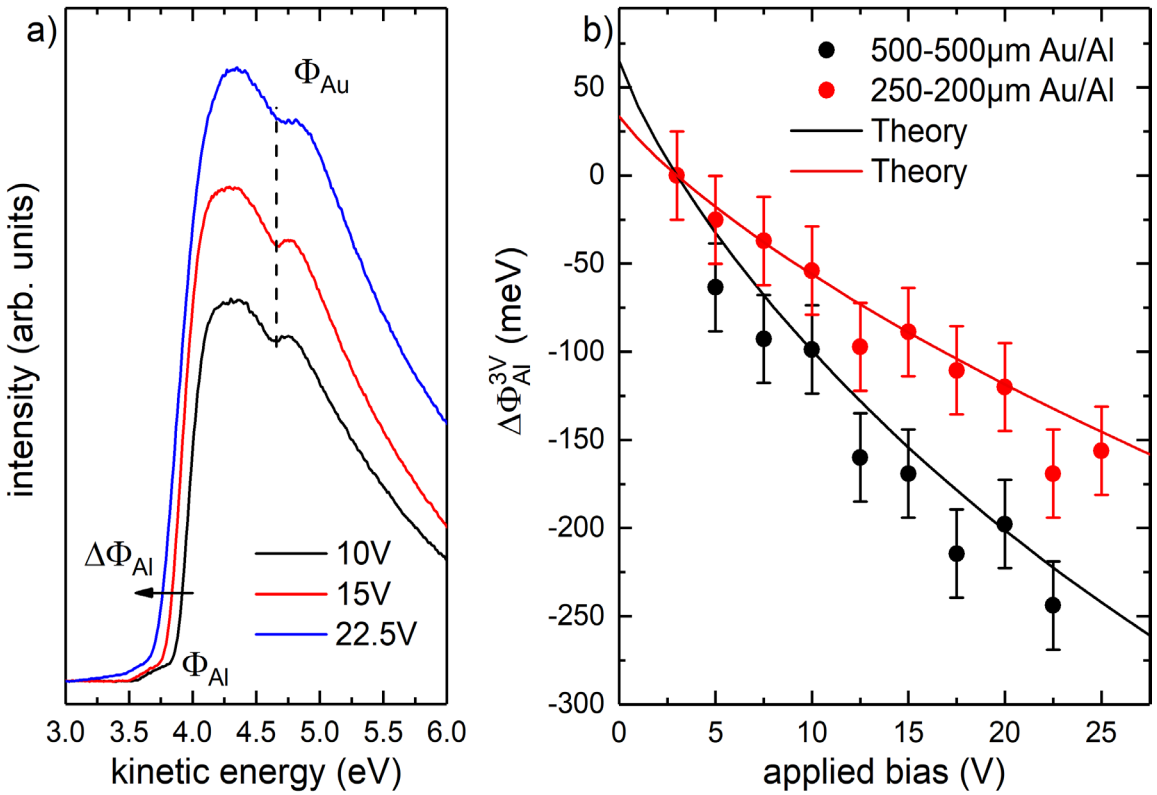

Figure 30: Results of UPS measurements on striped Au-Al samples. a) SECO spectra of 500-500 µm Au-Al striped samples for three different biases. The SECO corresponding to Al Φ_{Al} shifts to lower kinetic energies with increasing bias, whereas the SECO corresponding to Au remains constant. b) Summary of the Al SECO shift for different biases (referenced to the SECO at 3 V) for 500-500 and 250-200 µm Au/Al striped samples. The change in Δ_{Al} as calculated from equation (51) (solid lines) is in excellent agreement with measurements. Adapted from [101].

5.1.3 Influence of Heterogeneous Substrates on the Ionization Energy Determination of Subsequently Deposited Molecules

The above findings have direct influence when it comes to the determination of ionization energies IE of molecules, since it is determined directly from the measured work function Φ and the HOMO onset E_{HOMO} as $IE=\Phi+E_{HOMO}$. A wrong determination of Φ would inevitably lead to a false assignment of IE. Therefore, due to the averaging effect of the SECO as detailed above, it is necessary to use homogeneous substrates to accurately determine the IE of molecules. In practice, a substrate often used for the IE determination of molecules is indium tin oxide (ITO). However, it was found that the work function of ex-situ cleaned ITO films can change by up to 0.5 eV during UPS measurements, most probably due to UV-light-induced chemical reactions of surface contaminations with the ITO surface [123]. This could lead to inhomogeneities on the substrate surface, which would lead to an increase in the measured work function due to the averaging effect discussed above. This would in turn lead to a false determination of IE. In this section it is demonstrated how heterogeneous substrates (with spatially varying surface potential) influence the IE determination by UPS and how a correct IE value can still be obtained by careful data analysis. Two examples are given, using the bilinear samples consisting of CSH/FSH stripes with 4 µm periodicity as shown in Figure 25 a) and e) as substrates and evaporating two commercially available organic molecules (C_{60} and CBP) on top, whose ionization energies are well known.

Figure 31 shows the UPS results of 10 nm C_{60} deposited onto a symmetrically striped CSH/FSH sample comparable to the one shown in Figure 25 a) and Figure 26 b). Two cut-offs can be clearly distinguished in the SECO spectrum. Following a conventional way of data analysis, one would determine the work function from the low kinetic energy cut-off and obtain a value of 4.82 eV. Combined with the HOMO onset at 1.3 eV binding energy one would obtain an ionization energy for C_{60} of 6.12 eV, which is lower than the well-known value of 6.4 ± 0.1 eV [39,43,124–126]. This emerges from a wrong assignment of the SECO to the HOMO onset, as becomes clear after a more detailed analysis explained in the following. As shown in Figure 31 c) and d), the SECO spectrum can be perfectly fitted with two components, the red one representing C_{60} on top of FSH, with a work function of 5.14 eV, and the blue one coming from C_{60} on CSH, with an averaged work function of 4.82 eV. As shown in Figure 31 d), the valence spectrum can also be fitted excellently by two bulk C_{60} spectra. Here the red component at lower binding energy stems again from C_{60} on FSH and the blue component from C_{60} on CSH. Using the right

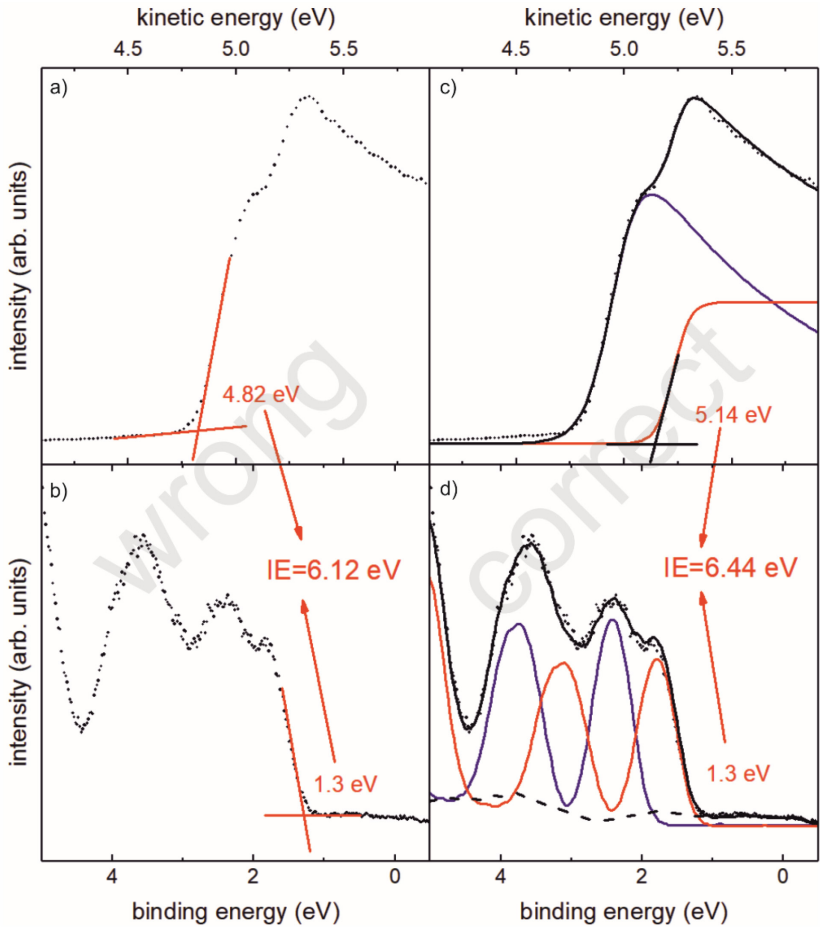

Figure 31: UPS measurements of 10 nm C_{60} evaporated onto a symmetric bilinear patterned sample, shown in Figure 25 a). a) and c) show the SECO spectrum and b) and d) the valence region spectrum. A conventional data analysis (left panels) would lead to an underestimation of the ionization energy of C_{60}, due to a wrong assignment of SECO and HOMO onset. A more careful analysis (right panel) yields correct values for the IE of C_{60}. Adapted from [102].

combination of SECO (high kinetic energy component) and E_{HOMO} (low binding energy component) one obtains an ionization energy for C_{60} of 6.44 eV, in perfect agreement with literature values. In this example, however, the presence of a second SECO is quite obvious. The following example demonstrates a case, were the presence of a second contribution in the SECO spectra is almost completely hidden.

For the second example nominally 10 nm of CBP were deposited on an asymmetrically striped CSH/FSH sample, comparable to the one shown in Figure 25 e) and Figure 26 b). The UPS results are shown in Figure 32. Here again the SECO spectrum is shown in a) and c) and the valence region spectrum in b) and d). In this case, due to the lower FSH coverage, the averaged cut-off is at lower kinetic energy and the high work function shoulder is almost invisible (the whole spectrum is shifted by $\approx$ 0.4 eV to lower kinetic energies compared to the previous example, because the pristine gold substrate where the CSH and FSH stripes were printed on had a 0.4 eV lower work function). Without exact knowledge of the sample surface (from KPFM measurements for example) one would most certainly overlook this shoulder when evaluating the data. Conventional analysis would yield a work function of 4.37 eV and together with the E_{HOMO} of 1.3 eV, this would result in an ionization energy for CBP of 5.67 eV. Literature values for CBP give an ionization energy of 6.15 ± 0.15 [48,127–131], which is much higher than the previously determined value. This is again due to the wrong assignment of SECO and E_{HOMO}. Fitting the SECO spectrum, as shown in Figure 32 c), reveals a small second contribution with an onset at 4.85 eV, stemming from CBP on FSH. This value, together with the HOMO onset of 1.3 eV, results in an IE of 6.15 eV, which is in perfect agreement with values reported in literature.

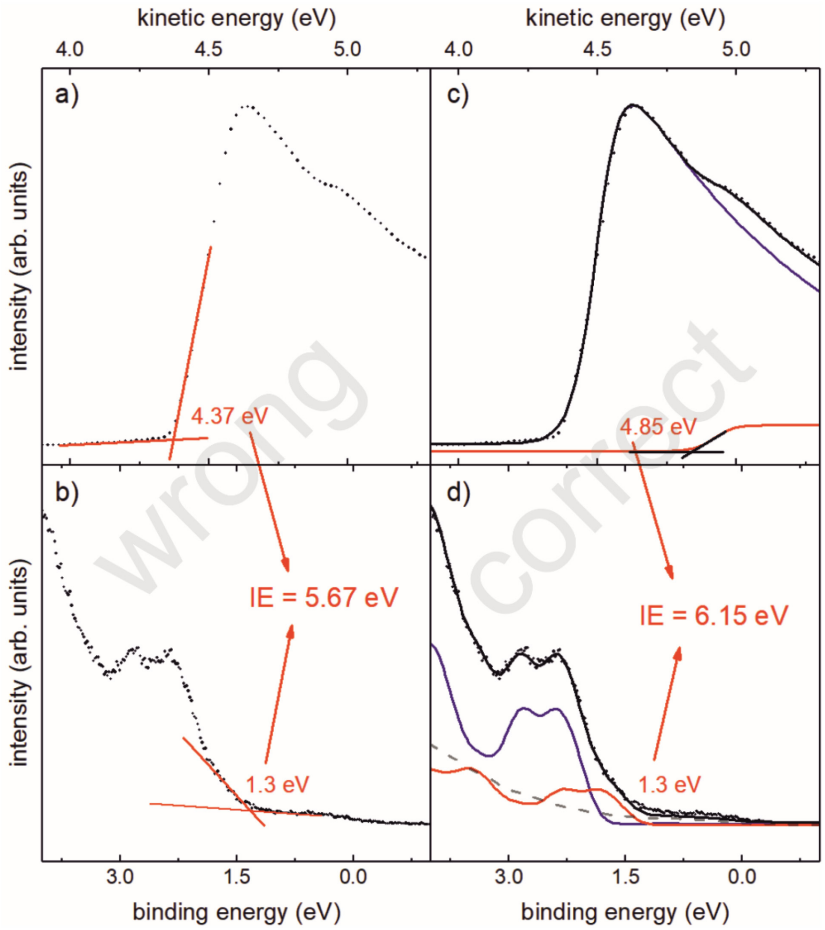

Figure 32: UPS measurements of 10 nm CBP evaporated onto an asymmetric bilinear patterned sample, shown in Figure 25 e). a) and c) show the SECO spectrum and b) and d) the valence region spectrum. A conventional data analysis (left panels) would lead to a severe underestimation of the ionization energy of CBP, due to a wrong assignment of SECO and HOMO onset. A more careful analysis (right panel) yields correct values for the IE of CBP. Adapted from [102].

In conclusion, in this section it was demonstrated how work function heterogeneities influence the results of UPS measurements. By investigating a well-defined model system of bilinear stripes it was shown, both experimentally and theoretically, that an additional potential barrier is formed above low work function areas, leading to an area-averaging effect, which shifts the low kinetic energy cut-off in UPS measurements to higher kinetic energies. Furthermore the influence of the applied electric field between sample and analyzer and of the feature size was demonstrated. It was additionally shown how a heterogeneous substrate influences the determination of the ionization energy of subsequently deposited molecules and how correct IE values can be obtained, by carefully analyzing the SECO spectra in more detail.

5.2 Work Function Modifications and Energy Level Alignment at Hybrid Semiconductor Interfaces

An important parameter for the functionality and performance of a multilayer device is the energy level alignment (ELA) between the different active layers or between the active layers and the electrical contacts [8]. Whereas for organic solar cells a large energy offset is preferred to facilitate exciton dissociation [132], a resonant ELA is desirable for energy transfer, e. g. in hybrid light emitting structures [3]. Combining two materials, each having favorable individual properties, does usually not result in a desired ELA and therefore does not yield desired device performance. However, there are different possibilities to modify the ELA between two materials, which have been extensively studied for metal electrodes [50,133–136]. One promising way to achieve desired ELA in hybrid device structures is to insert a thin interlayer of strong organic donor or acceptor molecules to change the work function of the underlying substrate and in turn the ELA with a subsequently deposited organic layer. This is schematically shown in Figure 33 for a HIOS system. The initial work function Φ_0 of the inorganic semiconductor can be modified with the help of organic donor/acceptor layers. This is discussed in detail in this section, including the influence of surface states and bulk donor concentration of the inorganic semiconductor on the work function changes after acceptor deposition. In section 5.2.3 the possible range of ELA modification is demonstrated for frequently used inorganic and organic semiconductors.

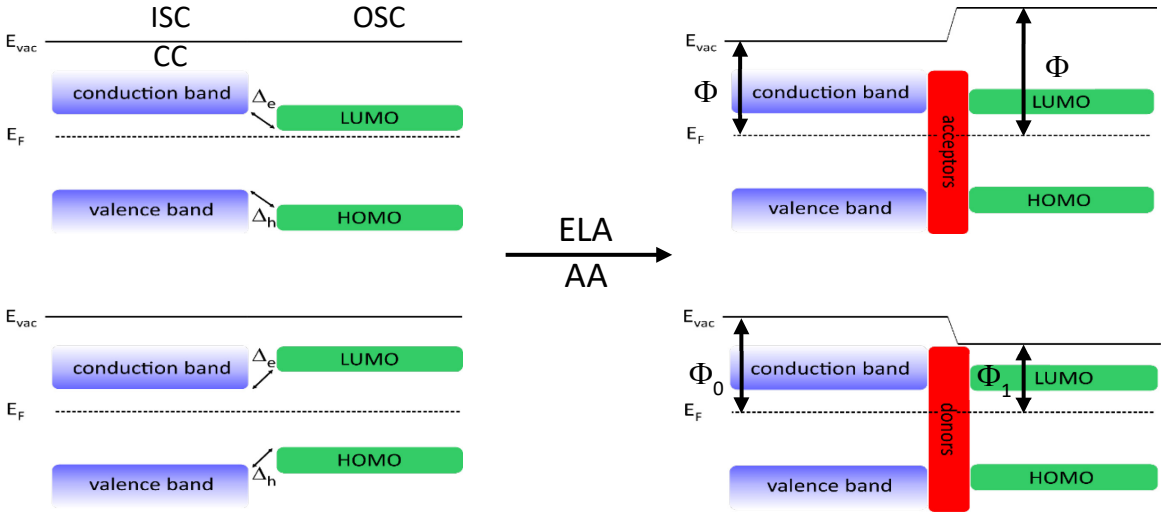

Figure 33: Schematic illustration of the interlayer method for energy level alignment manipulation at an inorganic/organic semiconductor interface. An intrinsic ELA (left) would result in undesired hole and electron barriers $\Delta_{e/h}$. With thin organic donor or acceptor interlayers (right) the initial work function Φ_0 of the ISC can be changed such that the subsequently deposited OSC aligns in the desired way.

5.2.1 Work Function Increase of Inorganic Semiconductors with Strong Organic Acceptor Molecules

5.2.1.1 Influence of Bulk Doping Concentration

The controlled doping of semiconductors is indispensable for nowadays semiconductor technology, as it for example enables the fabrication of p-n junctions in diodes or transistors or improves electron and hole blocking layers [137,138]. With increasing research interest in the area of hybrid devices, consisting of inorganic and organic semiconductors, it is important to understand the influence of the doping on the energetic alignment at such interfaces. However, only a few studies addressed this issue so far. Schlesinger *et al.* presented a classical approach based on Fermi-Dirac-statistics, which suggests a strong dependence of band bending and charge transfer on the bulk doping concentration of the inorganic semiconductor [88], while Xu *et al.* came to similar conclusions using a semi-classical approach including DFT [139]. The only known publication that directly addresses this issue experimentally is by Gleason-Rohrer *et al.*, who studied the band bending and interface dipoles of Si(111) with different chemical surface functionalizations [140]. They found that the band bending depends much more on the functionalizing group than on the doping and that very high doping concentrations lead to a pinning of the energy levels. However, these functionalizations were all based on chemisorption, while many organic molecules physisorb on semiconductor surfaces.

In this section the influence of the bulk doping concentration of ZnO $(000\bar{1})$ on the changes in work function and band bending after adsorption of the strong organic acceptor molecule F6-TCNNQ is investigated. For this purpose samples with different amounts of gallium, leading to n-doping, were grown by MBE by Sergey Sadofev at the Humboldt-Universität zu Berlin (see section 4.1.2). To ensure work function saturation, approximately 10 nm F6-TCNNQ were evaporated on the differently doped ZnO samples. The results are summarized in Figure 34. By and large, the work function of the samples is independent of the doping concentration, as can be seen from the SECO spectra in a), which all show a cut-off at 3.75 ± 0.05 eV. Solving charge neutrality equation (26) for the given donor concentrations yields a bulk Fermi-level position between 90 meV below the conduction band and slightly above the conduction band. This difference is rather small compared to changes in the work function after F6-TCCNQ deposition. Although the ZnO is probably degenerately doped at such high doping concentrations, possible effects like band gap

renormalization or changes of effective mass are neglected in the further discussion, as they are typically smaller than 0.05 eV for the highest carrier concentration investigated here [141,142]. After deposition of 10 nm F6-TCNNQ the SECOs shift to higher kinetic energies, indicating an increase in work function. The work function saturates at 5.70 ± 0.05 eV independent of the doping concentration, in good agreement with previous reported values for F6-TCNNQ on graphene [44] and F4-TCNQ (a similar organic acceptor) on ZnO $(000\bar{1})$ [88]. This value is reasonable, considering an electron affinity of F6-TCNNQ of 5.6 eV [95,143]. Besides a shift in the SECO also a shift in all core levels and in the VB spectrum of the ZnO to lower binding energies can be observed after F6-TCNNQ deposition. This is shown for the $Zn2p_{3/2}$ core level in Figure 34 b). The energy level shifts of the ZnO can be directly translated into an increase in upward band bending inside the ZnO. The $Zn2p_{3/2}$ peak is located at 1022.35 ± 0.05 eV binding energy for donor concentrations of $2 \cdot 10^{17}$ cm^{-3} and $7 \cdot 10^{18}$ cm^{-3} and shifts to 1022.19 ± 0.05 eV for

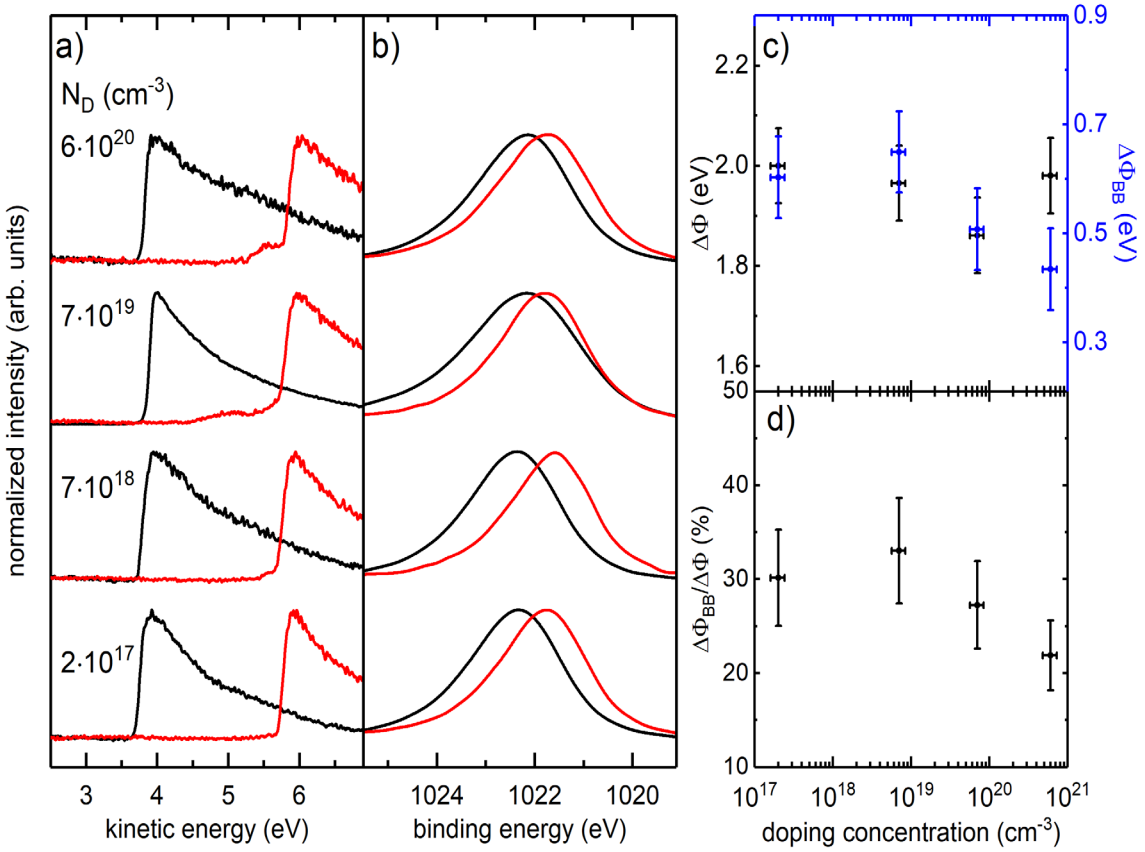

Figure 34: Results of differently doped ZnO samples before (black) and after (red) deposition of about 10 nm of F6-TCNNQ. a) Normalized SECO spectra, b) normalized $Zn2p_{3/2}$ core levels, c) changes in work function (black) and band bending (blue, determined from the average shift of $Zn2p_{3/2}$ and Zn3d core levels) and d) ratio of band bending contribution to the overall work function shift. Adapted from [100].

higher doping concentrations. Considering that the Fermi-level position in the bulk is closer to the conduction band for higher donor concentrations this indicated an increased upward band bending already before F6-TCNNQ deposition. This is in line with a shift of the valence band onset from 3.20 ± 0.05 eV to 3.00 ± 0.05 eV (see Appendix Fig. 2 b)). Comparing this to the band gap of ZnO (3.3 eV [92,144]) and the bulk Fermi-level positions obtained by charge neutrality equation results in slight upward band bending of about 0.3-0.4 eV for higher doping concentrations, whereas the bands of moderately doped ZnO are flat within the measurement uncertainty. The change in band bending after F6-TCNNQ deposition is determined from the average shift of the $Zn2p_{3/2}$ (Figure 34 b)) and the Zn3d (Appendix Fig. 2 a)) core levels, as they have similar surface sensitivity (compare Figure 11) and can be well resolved. A direct determination from the valence band onset is not possible, as this region is overlapped by signal from the F6-TCNNQ. The changes in band bending $\Delta\Phi_{BB}$ and total work function $\Delta\Phi$ as a function of doping concentration are summarized in Figure 34 c). With 1.96 ± 0.06 eV the work function change is independent of the doping concentration within the measurement uncertainties. The change in band bending is 0.6-0.7 eV for moderate doping concentrations and is reduced to 0.4-0.5 eV for higher doping concentrations. The ratio of band bending to the overall work function change $\Delta\Phi_{BB}/\Delta\Phi$ is shown in Figure 34 d) and basically follows the trend of the band bending change. Taking into account the 0.2 eV initial upward band bending of the pristine ZnO at higher doping concentrations it can be found that the Fermi-level is "pinned" at the surface at around 0.7 eV below the conduction band for all doping concentrations. Therefore it can be concluded that the bulk doping concentration of the inorganic semiconductor does not play a significant role for the energy level alignment at hybrid semiconductor interfaces.

Calculations by Xu *et al.* [139] and Schlesinger *et al.* [88] further suggest that a high doping concentration would result in a strongly increased charge transfer from the inorganic semiconductor to the organic acceptor (F4-TCNQ in their case). They find for example that an increase in doping concentration from 10^{17} cm^{-3} to 10^{20} cm^{-3} would lead to an increase of charged molecules from 1 % to 20 %. This is a quite significant difference, which should be detectable in UPS measurements. To check whether one can observe this difference in charge transfer one can have a closer look at the low binding energy range of a nominal monolayer (6-9 Å) of F6-TCNNQ on the differently doped substrates, as this is where one

expects features from charged molecules [44]. Since the cross section of F6-TCNNQ is low in this region, combined with the strong island growth already at sub-monolayer coverages, signal from the F6-TCNNQ cannot be directly observed in the spectra, as it is masked by the signal from the ZnO substrate. Therefore the background needed to be subtracted. The procedure is explained in detail in Fig. 3 in the Appendix. The resulting spectra with fits are shown in Figure 35 for the four different doping concentrations. By comparing the resulting difference spectra to literature data from F6-TCNNQ on graphene [44] three different peaks can be assigned. The blue peak at around 3 eV binding energy corresponds to the HOMO of neutral F6-TCNNQ molecules. It is slightly shifted to lower binding energy for doping concentrations of $7 \cdot 10^{19}$ cm^{-3} and $6 \cdot 10^{20}$ cm^{-3}. Although this is somehow in line with the observed shift of the valence band maximum and the core level positions to lower binding energies for higher doping concentrations before F6-TCNNQ deposition (see appendix Fig. 2), it is not understood yet, as the work functions of all samples initially are the same. Besides the HOMO peak of the neutral F6-TCNNQ one can assign the red peak at 1.65 ± 0.1 eV to the relaxed HOMO and the pink peak at 0.75 ± 0.1 eV to the partially filled LUMO of the charged molecules, which is qualitatively in line with a revised polaron picture of charged molecules by Winkler *et al.* [145]. It is clear at first glance that the amount of charged molecules does not change drastically with doping concentration of the ZnO. Estimating the ratio of charged molecules n^- from the area of the HOMOs of the charged molecules (red peak) I^- and the neutral molecules (blue) I^0, using

$$n^- = \frac{I^-}{I^- + I^0}, \tag{52}$$

results in values of $13 - 18$ %. However, these estimations must be interpreted with care, as they neglect possible different cross sections for the neutral and charged molecules, uncertainties induced by the process of background subtraction, and an uncertainty in the ratio of multilayer to monolayer molecules when comparing different samples. Nevertheless it can still be concluded that the amount of transferred charge from the inorganic semiconductor to the organic acceptor molecules, just like the change in work

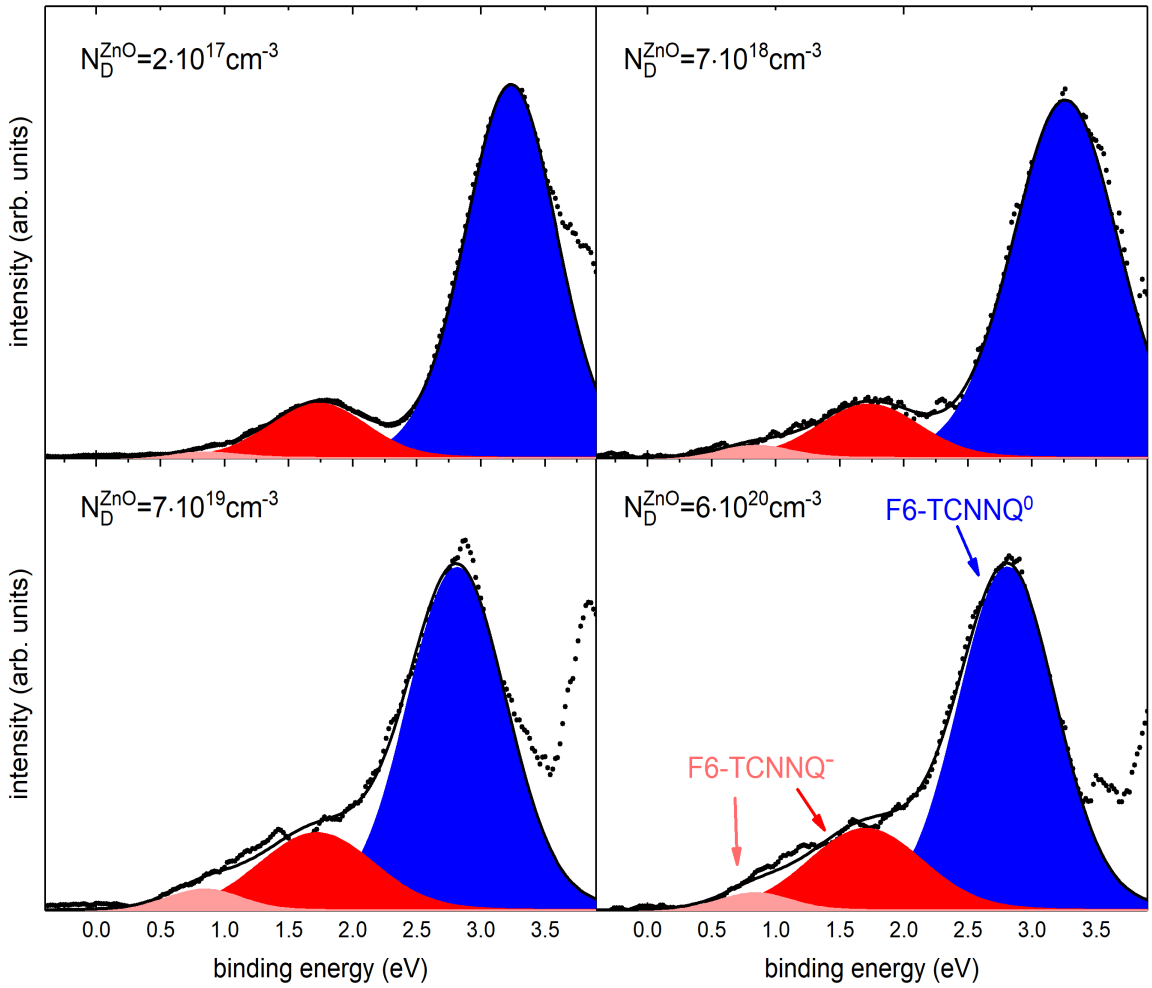

Figure 35: UPS spectra of the low binding energy region of approximately one monolayer of F6-TCNNQ deposited on differently doped ZnO $(000\bar{1})$ substrates. The spectra were obtained after background subtraction as described in Fig. 3 in the Appendix. Three different features can be observed in all spectra. The blue peak at around 3 eV binding energy, emerging from the HOMO of neutral F6-TCNNQ, the red peak at 1.7 eV binding energy, corresponding the relaxed HOMO of charged F6-TCNNQ molecules and the pink peak at 0.8 eV binding energy, corresponding to the singly filled LUMO of charged F6-TCNNQ molecules. The percentage of charged molecules, as determined from the area of the neutral and charged HOMO peaks, is between 13 and 18 % and seems slightly larger for higher doping concentrations.

function and band bending, does not depend strongly on the amount of donors inside the inorganic semiconductor. There must be a different reason for the pinning of the inorganic energy levels at a certain position, which could be the presence of charged surface states at the inorganic semiconductor surface. This will be discussed in more detail in the next section.

5.2.1.2 Influence of Surface States

As discussed in the last section, there must be a mechanism hindering the change of band bending inside an inorganic semiconductor upon adsorption of strong organic acceptor molecules. The presence of surface states was suggested to be a possible reason for this pinning effect. In this section it is demonstrated how the change in surface state density on the inorganic semiconductor surface influences the band bending change in the inorganic semiconductor. GaN (0001) was selected because of literature reports that suggest a simple way of reducing the amount of surface states [146,147].

The steps normally used for cleaning GaN (0001) in this thesis are described in section 4.1.2 and yield almost perfectly clean and stoichiometric surfaces. However, the annealing process leads to a breakup of the passivating Cl atoms, leaving behind Ga dangling bonds [147–150]. These dangling bonds form a density of acceptor-like surface states at about $0.6 - 0.8$ eV below the conduction band minimum [148,151]. For n-type GaN these surface states will lead to an upward band bending already for the pristine GaN surface, if their concentration is high enough. If the sputter and annealing procedure is omitted after the HCl treatment, the Cl atoms bind to the Ga atoms and saturate the free dangling bonds, therefore passivating the surface states [147]. This can also be seen in the energy levels of the differently treated samples. In Figure 36 the Ga3d core levels and the SECOs for the differently prepared samples are shown before (black) and after (red) deposition of 8 Å (about one monolayer) of F6-TCNNQ. The peak position of the Ga3d peak is shifted by about 0.5 eV to higher binding energy for the sample only treated by HCl, indicating different magnitudes of initial upward band bending, as the doping concentration of both samples is the same (residual doping concentration of $3 \cdot 10^{15}$ donors/cm^3, as determined by electrochemical C-V measurements). The exact amount of band bending can be calculated from the binding energy of the Ga3d peak, following a procedure given by Eller *et al.* [152]. This is more precise then determining the band bending from the valence band onset, as the UPS signal in the valence region of GaN is, in contrast to ZnO, very broad and decreases exponentially almost down to zero binding energy [102]. But since the difference in energy between the VBM and the Ga3d core level $\Delta_{VBM-Ga3d}$ is fixed and known (17.75 eV [153–155]), the band bending BB can be calculated by

$$BB = \Delta_{VBM-Ga3d} + E_G - E_B^{Ga3d} + E_C \,, \tag{53}$$

where E_G is the bandgap of GaN (3.4 eV at room temperature), E_B^{Ga3d} is the measured binding energy of the Ga3d peak and E_C is the distance of the Fermi-level to the conduction band minimum, which is determined to be -170 meV using charge neutrality equation (26) and the determined doping concentration. Combining all values results in

$$BB = 20.98\ \text{eV} - E_B^{Ga3d} \tag{54}$$

for the nominally undoped GaN samples. Using this one can determine the initial upward band bending of the differently prepared samples to be 0.06 eV for the samples treated only ex-situ by HCl and 0.54 eV for the subsequently in-situ sputtered and annealed samples. This is in line with the expected lower surface state density of the samples only treated by HCl and the dangling bond surface state density at around 0.6 eV below the conduction band minimum. Using equation (30) one can estimate that the charged surface state density of the HCl treated samples is in the order of $5 \cdot 10^{10}$ cm^{-2}, and that the charged surface state density for the sputtered and annealed samples must be larger than 10^{11} cm^{-2}. These values are way too low to be detectable with PES, as its detection limit is typically between 1 and 0.1 at.% [156]. The difference in initial band bending of 0.48 eV is in fair agreement with the difference in work function of the pristine samples of 0.37 eV, as the vacuum level follows the changes in band bending. This results in an ionization energy of 7.0 ± 0.1 eV and an electron affinity of 3.6 ± 0.1 eV (assuming an energy gap of 3.4 eV), which is in good agreement with literature [157,158].

After stepwise deposition of F6-TCNNQ the work function increases for both low and high densities of surface states, as expected, since the electron affinity of F6-TCNNQ is higher than the work function of both samples. Besides a shift of the SECOs to higher kinetic energies, also the core levels shift to lower binding energies as shown in Figure 36 a) exemplarily for the Ga3d core level. While the work function change $\Delta\Phi$ saturates at 1.6 ± 0.1 eV after a nominal coverage of 8 Å (which is typically associated with a closure of the monolayer) for both preparations, the change in core level binding energy, and with this the change in band bending $\Delta\Phi_{BB}$, is very different for both preparations. This is due to the difference in initial band bending, as for both preparations the Ga3d core level ends up at a binding energy of 20.24 ± 0.05 eV after monolayer coverage with F6-TCNNQ, corresponding to a final upward band bending of about 0.74 eV. This value is in good agreement with literature values reported for the energetic position of gallium dangling

bonds, being located 0.6-0.8 eV below the conduction band [149,159]. The detailed evolution of work function and Ga3d binding energy for both preparation methods are shown in Figure 37. It is striking that most of the change in Ga3d binding energy for the only with HCl prepared samples already takes place after the first deposition of 1 Å of F6-TCNNQ. Accordingly the initial change in work function is also higher for this samples. This becomes even clearer when looking at the ratio of work function change $\Delta\Phi$ and band bending change $\Delta\Phi_{BB}$, normalized with respect to the final changes (see Appendix Fig. 4). Based on this observations two mechanism being responsible for the changes in work function, as schematically shown in Figure 38, are proposed, depending on the surface state density on the inorganic semiconductor. In the case of low surface state density the energy levels are not pinned and free to change upon organic acceptor deposition. Starting with low coverages of acceptor molecules, all transferred charge to the acceptors stems from the bulk donors of the inorganic semiconductor. This yields a strong initial change in band bending (and with this also in work function), as the band bending changes quadratically with transferred charge, see equation (30). With the change in band bending also the position of the surface states changes with respect to the Fermi-level as shown in Figure 38 a). Once the Fermi-level intersects with the surface state density the surface states start to be depleted. This leads to a pinning of the Fermi-level around the surface state position,

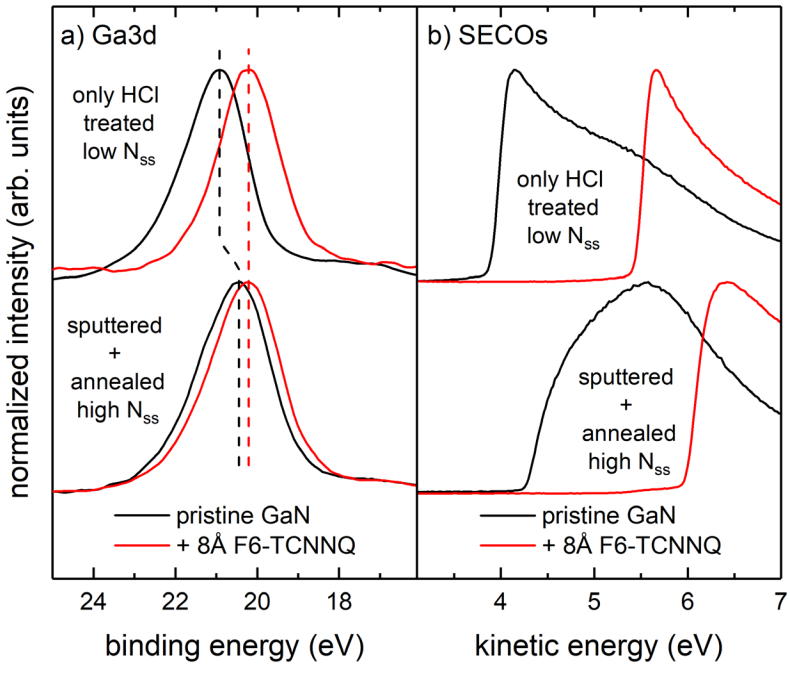

Figure 36: PES results of F6-TCNNQ deposition on undoped GaN with different surface state densities. a) Ga3d core level before (black) and after (red) deposition of a monolayer F6-TCNNQ. Different treatments lead to different concentrations of surface states, reflected by the different binding energies for the pristine samples. b) SECOs for the differently treated samples from a) before and after F6-TCNNQ deposition.

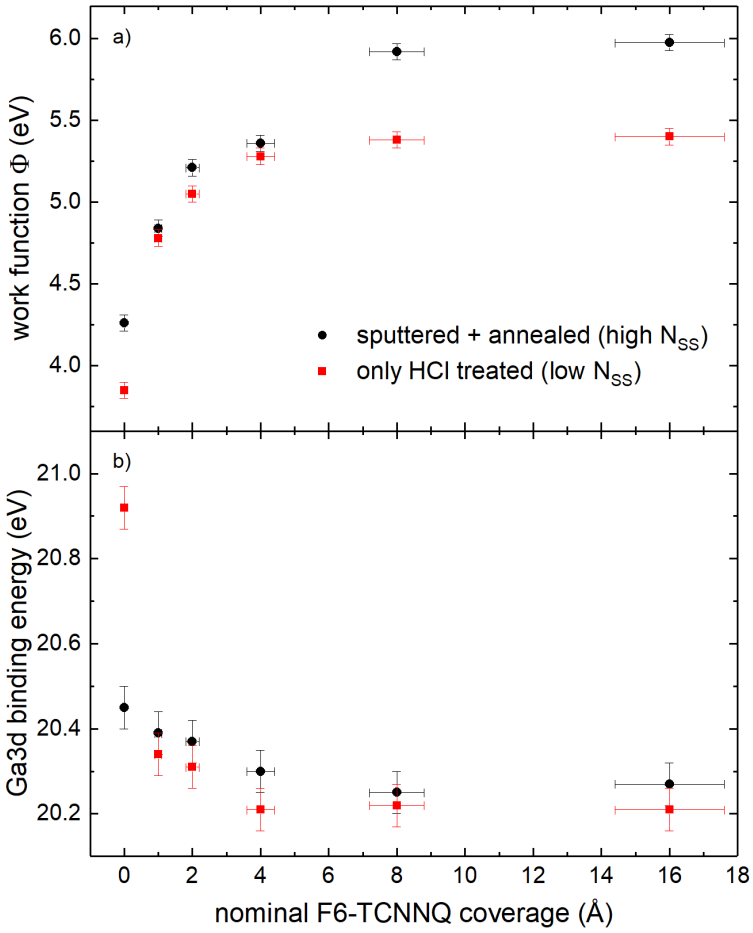

Figure 37: Summary of UPS results of F6-TCNNQ deposited on differently prepared undoped GaN surfaces. a) Work function of differently prepared GaN (0001) as a function of F6-TCNNQ coverage. For both preparation methods, resulting in high and low densities of surface states, the work function increases by about 1.6 ± 0.1 eV after nominally 8 Å F6-TCNNQ. b) Change in Ga3d binding energy, equivalent to an increase in upward band bending. For the sample with low N_{SS} most of the band bending occurs already after 1 Å. The Ga3d binding energy saturates at a value of 20.24 ± 0.05 eV for both surface state densities, corresponding to a total upward band bending of 0.74 eV.

as described in section 2.4.4 for the pristine inorganic surface. With further acceptor deposition the transferred charge then originates mainly from the surface states. This leads to only minor further changes in the band bending, but the work function still increases further due to the charge separation between the inorganic and the organic semiconductor, in literature often referred to as *interface dipole* [52,160,161]. For a high amount of surface states the Fermi-level of the inorganic semiconductor is already pinned in the absence of the organic acceptor molecules. Deposition of acceptor molecules leads to a depletion of the surface states and the formation of an interface dipole, with only minor changes in the band bending for all coverages, as depicted in Figure 38 b). This dependence of band bending changes on the surface state density has also been recently observed for perovskites after F6-TCNNQ or HATCN deposition [162].

Besides providing a qualitative picture of the influence of surface states it would be desirable to give a more quantitative description [102]. Therefore the model suggested by Schlesinger *et al.* [88], based on Fermi-Dirac-statistics and depletion approximation, was

extended to take into account the density of surface states. The first assumption is that the change in work function $\Delta\Phi$ can be separated into two parts as

$$\Delta\Phi = \Delta\Phi_{ID} + \Delta\Phi_{BB}, \tag{55}$$

where $\Delta\Phi_{ID}$ is the formation of an interface dipole and $\Delta\Phi_{BB}$ is the change in band bending inside the inorganic semiconductor. These two contributions can be described as a function of the transferred charge per area δq ([C/m^2]) by means of the Helmholtz equation

$$\Delta\Phi_{ID} = e\frac{\delta q}{\varepsilon_0 \bar{\varepsilon}} d_{eff}, \tag{56}$$

where d_{eff} is the distance between the organic acceptor and the inorganic surface (typically in the order of 3 Å) and $\bar{\varepsilon}$ is an average dielectric constant calculated from the dielectric

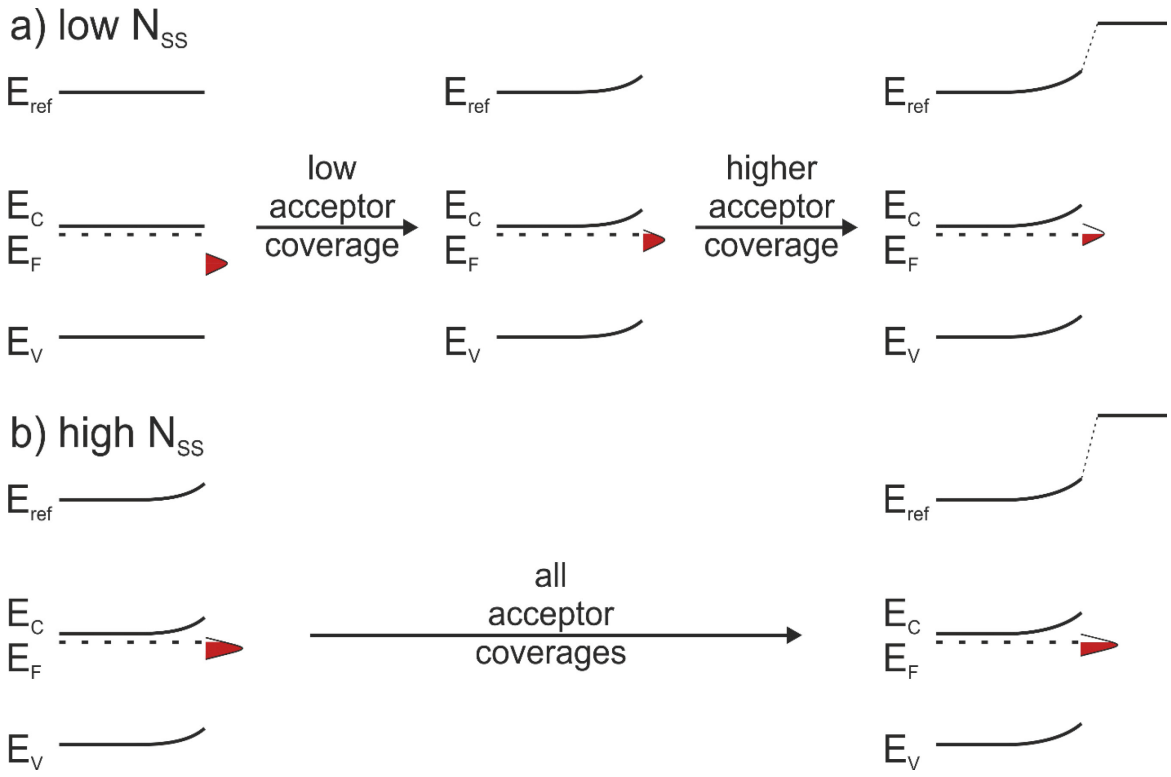

Figure 38: Qualitative description of the potential change of an inorganic semiconductor after deposition of organic acceptor molecules, depending on the amount of surface states on the inorganic semiconductor. a) For low amounts of surface states the energy bands are initially flat and free to move, leading to a large increase in band bending after initial deposition of acceptor molecules. Once the Fermi-level intersects the surface state density it becomes pinned and the band bending only changes slightly with further acceptor deposition. The charge transfer from the surface states to the acceptors then leads to the formation of an interface dipole, further increasing the work function. b) For a high amount of surface states the Fermi-level is already pinned from the beginning and depletion of surface states and interface dipole formation is dominant for all acceptor coverages.

constant of the inorganic semiconductor (≈9 for GaN) and the organic semiconductor (≈3), and in depletion approximation [13]

$$\Delta\Phi_{\mathrm{BB}} = \frac{\delta q^2}{2\varepsilon_0 \varepsilon N_D}, \tag{57}$$

where ε is the dielectric constant of the inorganic semiconductor and N_D its donor concentration. It is further assumed that charge is transferred to the acceptor molecules as long as the LUMO of the molecules is positioned below the Fermi-level, given by Fermi-Dirac-statistics:

$$\delta q \sim \frac{1}{1 + \mathrm{e}^{(\Phi_0 + \Delta\Phi - EA)/k_B T}}. \tag{58}$$

Here Φ_0 is the initial work function of the inorganic semiconductor and EA is the electron affinity of the organic acceptor. By iteratively increasing δq in accordance with equation (58) and calculating $\Delta\Phi_{\mathrm{ID}}$ and $\Delta\Phi_{\mathrm{BB}}$ by equation (56) and (57) until convergence, one can calculate the two different contributions to the work function change as a function of doping concentration, as done by Schlesinger *et al.* [88]. However, this does yield a strong dependence on the doping concentration, which was found to not play a significant role for the different contributions to the work function change, as shown in the previous section. To include the presence of surface states equation (57) is modified to

$$\Delta\Phi_{\mathrm{BB}} = \frac{\left(\delta q \frac{N_D}{N_D + N_S/\lambda_S}\right)^2}{2\varepsilon_0 \varepsilon N_D}. \tag{59}$$

Here N_S is the amount of surface states and λ_S is the surface state tailing length, which is typically in the order of 2-4 Å [163]. Equation (59) takes into account that only the charges actually transferred from the dopants to the acceptor molecules contribute to the change in band bending, while the electrons transferred from the surface states do not. It further assumes an equal probability of charge transfer from the dopants and the surface states and neglects the energetic position of the surface states. Using equations (56), (58) and (59) one can, for example, derive the band bending contribution $\Delta\Phi_{\mathrm{BB}}/\Delta\Phi$ as a function of doping concentration N_D and surface state density N_S. This is shown for GaN and F6-TCNNQ in Figure 39 a). The limit of $N_S \to 0$ yields the *empty gap* model by Schlesinger *et al.* [88]. It becomes clear that for higher doping concentrations a higher amount of surface states is

needed to suppress band bending changes, as already known for the pristine inorganic semiconductor surfaces (Figure 9). This holds until the doping concentration exceeds a critical amount of 10^{22} donors/cm^3, where the band bending is suppressed, just as if the material would be a metal. In Figure 39 b) a cut through Figure 39 a) is shown for a doping concentration of $3 \cdot 10^{15}$ donors/cm^3, the doping concentration present in the unintentionally doped GaN (0001) samples used in this thesis. For surface state densities larger than 10^{10} cm^{-2} the band bending change after F6-TCNNQ deposition is strongly suppressed. The measured $\Delta\Phi_{BB}/\Delta\Phi$ values for the differently prepared samples (only *ex-situ* HCl vs. *in-situ* sputtered + annealed) are marked by circles. Based on these results this model yields surface state densities of $\approx$ 5-6 $\cdot 10^{10}$ cm^{-2} for the *ex-situ* prepared samples and $\approx$ 1-2 $\cdot 10^{11}$ cm^{-2} for the *in-situ* prepared samples, in good agreement with the values estimated from the initial band bending. Although this model describes the relative changes for two different surface preparations, and with this different densities of surface states, reasonably well, the present model still needs to be further extended. The energetic position of the surface states within the band gap needs to be taken into account if one wants to make predictions about the absolute changes of band bending after acceptor deposition.

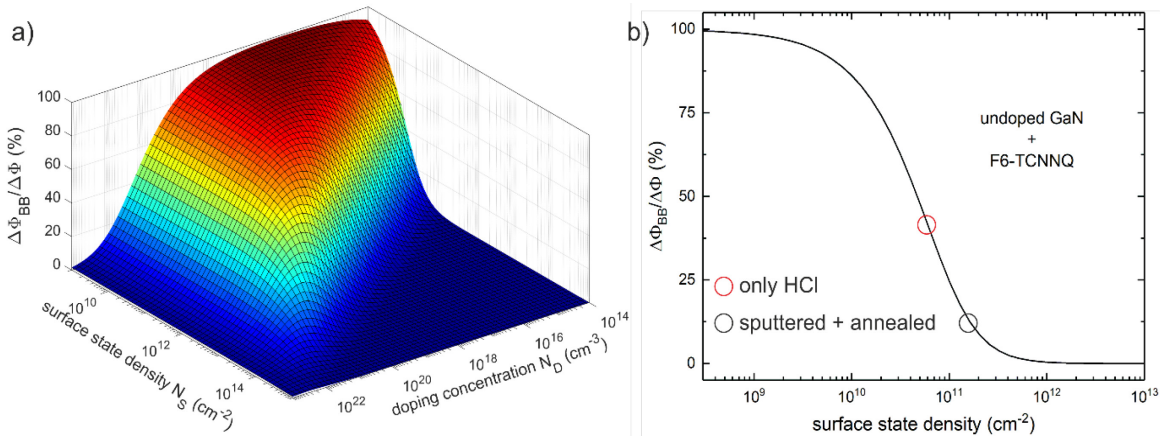

Figure 39: Results of surface state model calculations. a) Calculated band banding contribution to the work function change of GaN after F6-TCNNQ deposition as a function of bulk doping concentration N_D and surface state density N_S. b) Line-cut through a) for a doping concentration of $3 \cdot 10^{15}$ donors/cm^3, giving the band bending contribution as a function of the surface state density for the measured samples. The band bending contributions for the differently prepared samples are marked by circles.

5.2.2 Work Function Reduction of Inorganic Semiconductors with Strong Organic Donor Molecules

To extend the range of possible ELA to a subsequent organic material it is also necessary to be able to decrease the work function of the inorganic semiconductor. Therefore the possible work function reduction of GaN and Si with the help of organic donors ($[RuCp^*(mes)]_2$) is demonstrated in this section. $[RuCp^*(mes)]_2$ is an air stable dimer, which splits up into monomers after contact with an electron accepting surface and thereby reduces its ionization energy [164]. In this way it can be used to lower the work function of different materials down to 3 eV and below [3,165]. The SECOs of u-GaN with different coverages of $[RuCp^*(mes)]_2$ are shown in Figure 40 a). The SECO shifts to lower kinetic energies with increasing $[RuCp^*(mes)]_2$ coverage until it saturates at a nominal coverage of 8 Å. Starting out with a work function of 4.3 eV for the clean GaN the work function saturates at about 2.2 eV for monolayer coverage with $[RuCp^*(mes)]_2$. This is a substantial decrease of more than 2 eV. The work function evolution as a function of nominal $[RuCp^*(mes)]_2$ coverage is shown in Figure 40 b). It can be seen that the work function does not change any further with increasing coverage after a closed monolayer is reached. This is a commonly observed phenomena, since multi-layers do usually not contribute significantly to the charge transfer [43,45,88,145,166]. The initially strong decrease of the work function originates from an electron transfer from the organic donor to the inorganic semiconductor. This leads to the formation of an interface dipole and a decrease of the initial upward band bending present in the GaN. Initially the clean u-GaN shows an upward band bending of about 0.4 eV, as determined from the binding energy position of the Ga3d peak [167]. The reason of this initial band bending are acceptor like surface states, as discussed in detail in the previous section. After deposition of a monolayer of $[RuCp^*(mes)]_2$ the upward band bending is reduced by about 0.2 eV, estimated from the shift in binding energy of the $Ga2p_{3/2}$ peak. Differently charged species were observed for the Ru3d peak in XPS (see Appendix Fig. 5), suggesting the presence of neutral $[RuCp^*(mes)]^0$ and charged $[RuCp^*(mes)]^+$ molecules [3]. Therefore, probably integer charge transfer takes place at this interface. However, since the aim of the application of the $[RuCp^*(mes)]_2$ interlayer is to decrease the work function of the ISC for subsequent deposition of an organic semiconductor no further details about the origin of the work function reduction will be discussed at this point. Similar results were obtained for

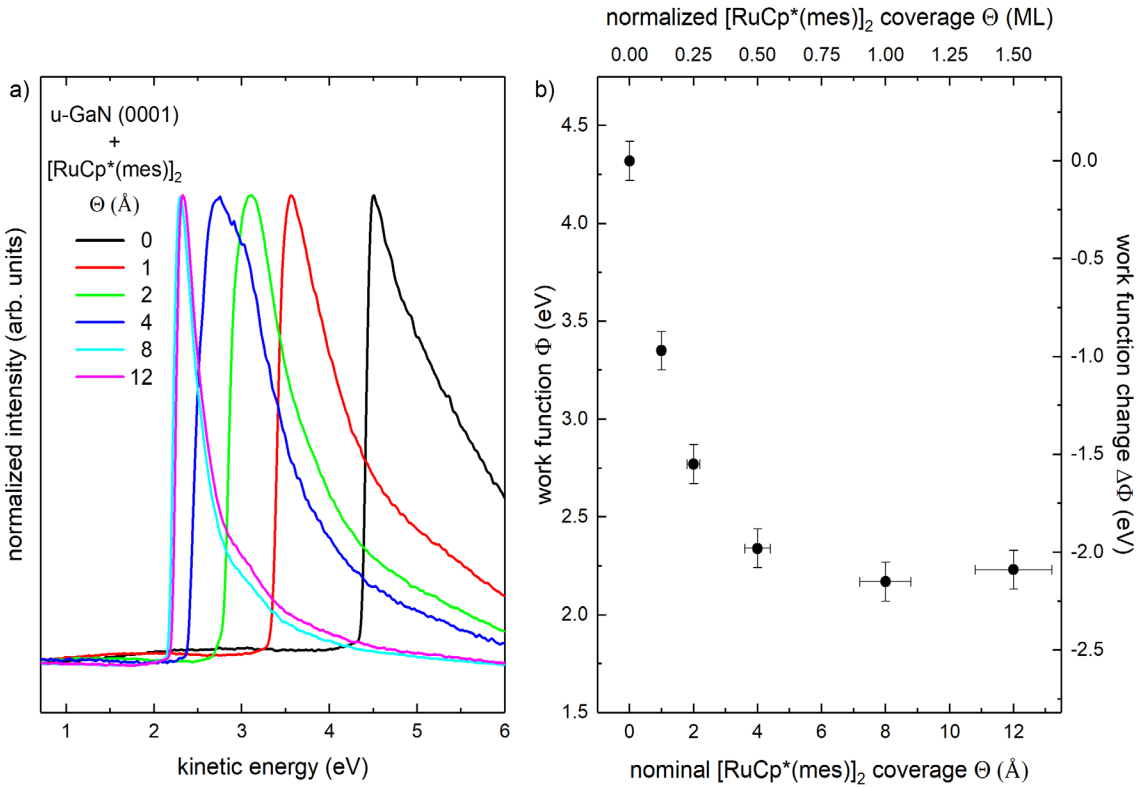

Figure 40: a) SECO spectra for undoped GaN (0001) and different nominal coverages of $[RuCp^*(mes)]_2$. The SECO shifts to lower kinetic energies with increasing nominal coverage. b) Work function obtained from the SECO spectra in a) as a function of coverage. The work function of GaN can be decreased down to 2.2 eV with only 8 Å of $[RuCp^*(mes)]_2$.

$[RuCp^*(mes)]_2$ on Si:H (111). The work function of pristine Si:H decreases from 4.2 ± 0.1 eV down to 2.5 eV after deposition (see Appendix Fig. 6). But here the change in band bending is much larger and accounts to about 0.5 eV after monolayer coverage, changing from initial upward band bending to slight downward band bending. The Ru3d core level also shows two contributions in this case.

5.2.3 Modified Energy Level Alignment in Inorganic/Organic Semiconductor Systems

In this section the capability of organic donor/acceptor interlayers to influence the energy level alignment between inorganic and organic semiconductors is demonstrated on two examples, comprising a wide band gap inorganic semiconductor (GaN), a narrow band gap inorganic semiconductor (Si), and a prototypical organic hole transport material (α-NPD). By using strong organic acceptor (F6-TCNNQ) or donor ($[RuCp^*(mes)]_2$) interlayers, the

energy level alignment at the HIOS interfaces was successfully modified in a range of up to 2.5 eV, demonstrating the great potential of the interlayer method for hybrid devices.

5.2.3.1 Gallium Nitride / α-NPD

For the investigation of possible energy level alignment scenarios between GaN and α-NPD, p-doped GaN was selected, because it has a large work function of 5.6 eV, i.e. sufficiently high to induce HOMO level pining for α-NPD (pinning work function 4.8 eV [49]). Therefore only a work function reducing donor interlayer needs to be studied to explore the limits of energy level alignment tuning between GaN and α-NPD. For this purpose $[RuCp^*(mes)]_2$, which was the strongest air-stable dopant available, was used. Nominally 10 nm of α-NPD were deposited on both pristine and molecularly modified GaN surfaces. In Figure 41 the UPS spectra of p-GaN+α-NPD (black) and p-GaN+$[RuCp^*(mes)]_2$+α-NPD (blue) are shown. As expected, HOMO-level pinning occurs and electrons are transferred from the HOMO of α-NPD into positively charged surface states of the p-GaN, leading to a decrease of the downward band bending inside the p-GaN. This effect is overcompensated by an interface dipole formed by the electron transfer and the work function is effectively reduced. The HOMO onset is located ~0.2 eV below the Fermi-level. A $[RuCp^*(mes)]_2$ interlayer reduces the work function of p-GaN down to 2.34 eV, due to electron transfer from the $[RuCp^*(mes)]_2$ HOMO into the GaN conduction band, donor surface states or bulk acceptors. This leads to a further increase of

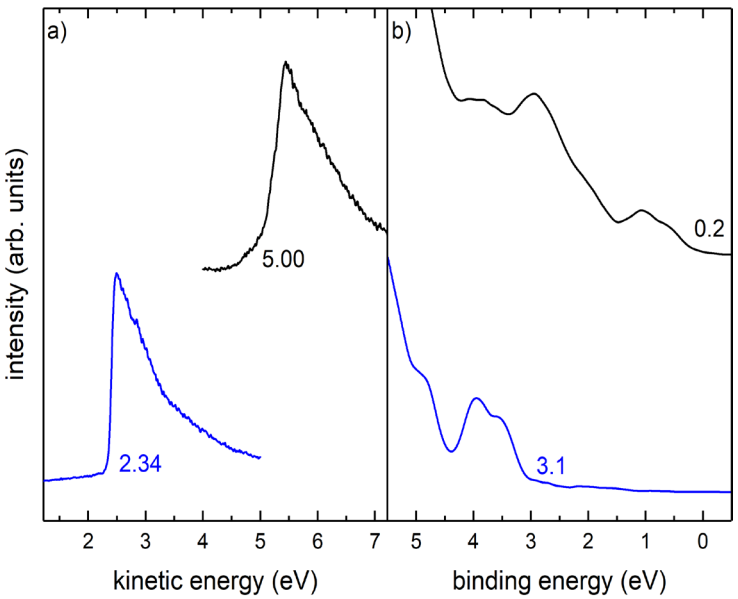

Figure 41: UPS spectra of pristine p-GaN (black) and p-GaN modified by $[RuCp^*(mes)]_2$ (blue), with nominally 10 nm α-NPD on top. a) SECO spectra and b) the corresponding valence regions. Numbers indicate the work function and HOMO onset, respectively. The HOMO onset of α-NPD can be tuned by 2.9 eV with the help of the organic donor interlayer.

the downward band bending. The work function is still too high to lead to LUMO level pinning, therefore the α-NPD is vacuum level aligned to the modified p-GaN, which leads to a HOMO onset 3.1 eV below the Fermi-level. The detailed energy level diagrams are shown in Figure 42. Without the donor interlayer, electrons at the interface tend to move to the p-GaN and holes to the α-NPD. The $[RuCp^*(mes)]_2$ interlayer changes the energy level alignment in such a way that this tendency is reversed.

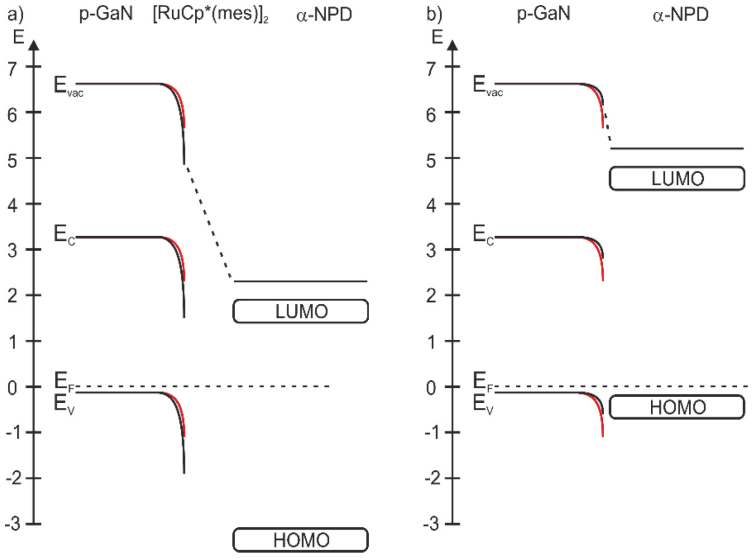

Figure 42: Energy level diagrams of a) p-GaN+$[RuCp^*(mes)]_2$+α-NPD and b) p-GaN+α-NPD. Red lines indicate the energy levels of p-GaN before deposition of molecules. At the pristine p-GaN / α-NPD interface electrons tend to go to the p-GaN and holes to the α-NPD. With the $[RuCp^*(mes)]_2$ interlayer the energy level alignment is changed in such a way, that electrons now tend to go to the α-NPD and holes to the p-GaN.

5.2.3.2 Silicon / α-NPD

The energy level alignment between differently modified hydrogen terminated silicon Si:H (111) and a prototypical organic hole transport material (α-NPD) is studied by UPS. Therefore nominally 5 nm α-NPD were deposited directly on Si:H or on Si:H modified by a thin layer of either F6-TCNNQ or $[RuCp^*(mes)]_2$. Figure 43 shows the SECO and valence spectra of Si:H+α-NPD (black), Si:H+F6-TCNNQ+α-NPD (red) and Si:H+$[RuCp^*(mes)]_2$+α-NPD (blue) after subtraction of the substrate background signal. For the pristine Si:H+α-NPD vacuum level alignment takes place, resulting in a α-NPD HOMO onset at 1.4 eV below the Fermi-level. The deposition of a thin interlayer of F6-TCNNQ increases the work function of Si:H to more than 5 eV. This value is again higher than the pinning work function of α-NPD [49], resulting in HOMO-level pinning. This leads to a final work function of 4.8 eV and a HOMO onset of 0.5 eV below the Fermi-level. The $[RuCp^*(mes)]_2$ interlayer on the other hand reduces the work function of

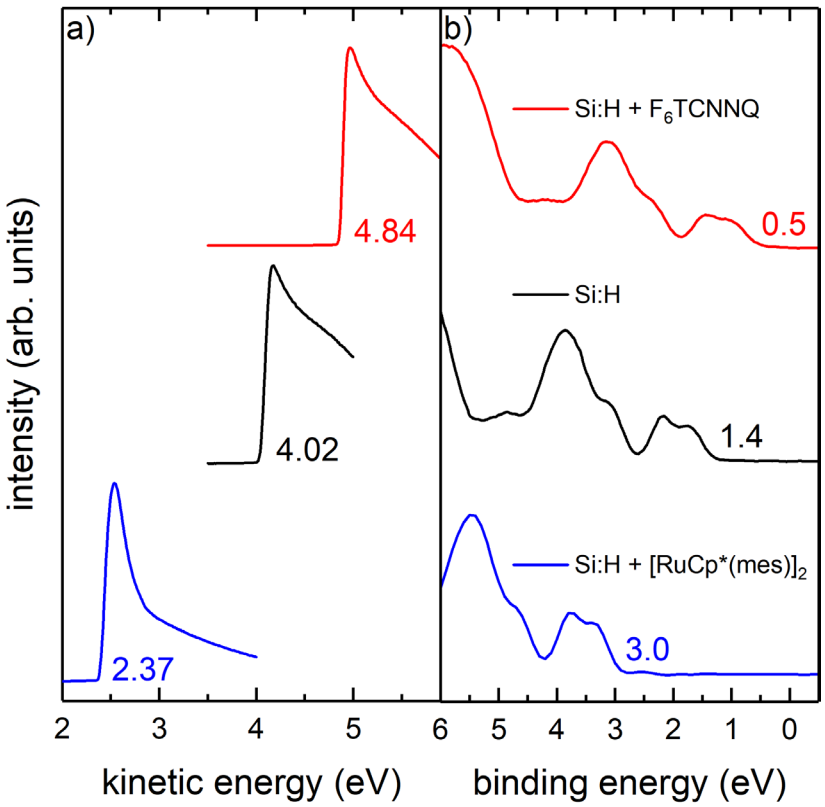

Figure 43: UPS spectra of pristine Si:H (black) and Si:H modified by F6-TCNNQ (red) or $[RuCp^*(mes)]_2$ (blue), with nominally 5 nm α-NPD on top. a) shows SECO spectra and b) the corresponding valence regions. Numbers indicate the work function and HOMO onset, respectively. The HOMO onset of α-NPD can be tuned by 2.5 eV with the help of organic donor/acceptor interlayers. Adapted from [104].

Si:H down to 2.37 eV. This is still higher than the electron affinity of α-NPD (1.5 eV [168]), resulting again in vacuum level alignment. In this case the HOMO onset of α-NPD is positioned 3.0 eV below the Fermi-level. The detailed energy level diagrams are shown in Figure 44, including changes in the band bending inside the silicon. After preparation,

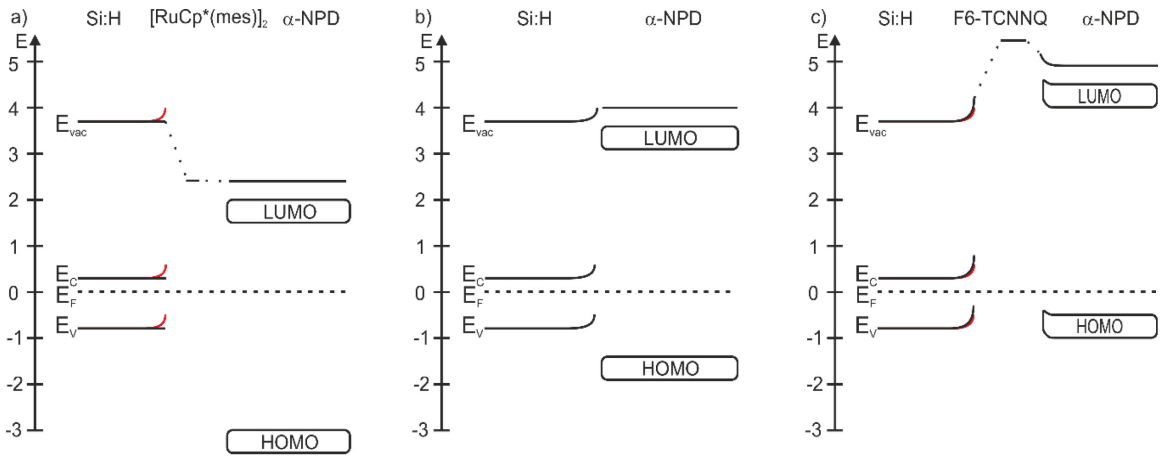

Figure 44: Energy level diagrams of a) Si:H+$[RuCp^*(mes)]_2$+α-NPD, b) Si:H+α-NPD and c) Si:H+F6-TCNNQ+α-NPD. Red lines indicate the energy levels of Si:H before donor/acceptor deposition. The energy level alignment between Si:H and α-NPD can be tuned by 2 eV using donor/acceptor interlayers.

as described in detail in section 4.1.2, the Si:H starts out with an upward band bending of 0.4 ± 0.1 eV. After deposition of $[RuCp^*(mes)]_2$ the Si2p core level shifts by 0.5 eV to higher binding energies, indicating a band flattening and even slight downward band bending. After deposition of F6-TCNNQ on the other hand the upward band bending increases slightly to 0.6 eV. Taking this into account one can give values for the VB-HOMO offset, which is often used as a figure of merit for possible hole injection/extraction. It ranges from 2.1 eV in the case of $[RuCp^*(mes)]_2$ down to -0.25 eV in the case of F6-TCNNQ.

In this chapter the influence of bulk doping concentration and surface states of the inorganic semiconductor on the energy level alignment between inorganic semiconductors and strong organic acceptor molecules was investigated in detail and it was demonstrated that the doping concentration plays only a minor role for the band bending change inside the inorganic semiconductor. The band bending is rather dictated by the surface state density and their energetic position within the band gap of the inorganic semiconductor. It was further demonstrated that the interlayer method, where the work function of the inorganic semiconductor substrate is changed by a thin layer of organic donor or acceptor molecules, can be used to manipulate the energy level alignment to a subsequently deposited organic semiconductor. The hole injection barrier between two different inorganic semiconductors and α-NPD could be tuned by more than 2 eV, rendering this method a very powerful tool.

5.3 Interface Between a 2D-Semiconductor and Strong Organic Acceptor Molecules

2-dimensional transition metal dichalcogenide semiconductors are of emerging interest for many possible opto-electronic applications, due to their direct band gap, large spin-orbit splitting or enhanced photoluminescence compared to their bulk counterparts [169–171]. Because of a lack of inversion symmetry, two non-equivalent valence band maxima form with opposite spin preference, opening up possible applications in valleytronic devices like valley filters or valves [172]. Combining 2D TMDCs with organic molecules, to directly change their properties or combined in heterostructures, further opens up a wide range of opportunities. As 2D TMCDs are relatively new (first synthesis by CVD in 2012), a lot of phenomena regarding the interface with organic semiconductors still need to be investigated. A first straight forward approach is to use organic acceptor molecules for interface doping, analogously to the case of bulk inorganic semiconductors in the previous chapter.

In this chapter the morphology and energy level changes after deposition of the strong organic acceptor $C_{60}F_{48}$ on the 2-dimensional transition-metal dichalcogenide WSe_2 are investigated using a complementary approach, consisting of scanning tunneling microscopy/spectroscopy (STM/STS), PES measurements and density functional theory (DFT) calculations. It is also demonstrated how the $C_{60}F_{48}$ improves the electrical properties of WSe_2 employed in a field effect transistor.

5.3.1 Morphology of $C_{60}F_{48}$ on WSe_2

The growth morphology of $C_{60}F_{48}$ on WSe_2 monolayers (ML) was investigated by low temperature (77K) STM measurements for different molecular coverages. All STM measurements were conducted by Zhibo Zong and Yuli Huang at National University of Singapore, using an Omicron high-resolution STM with electrochemically etched tungsten tips and constant current mode.

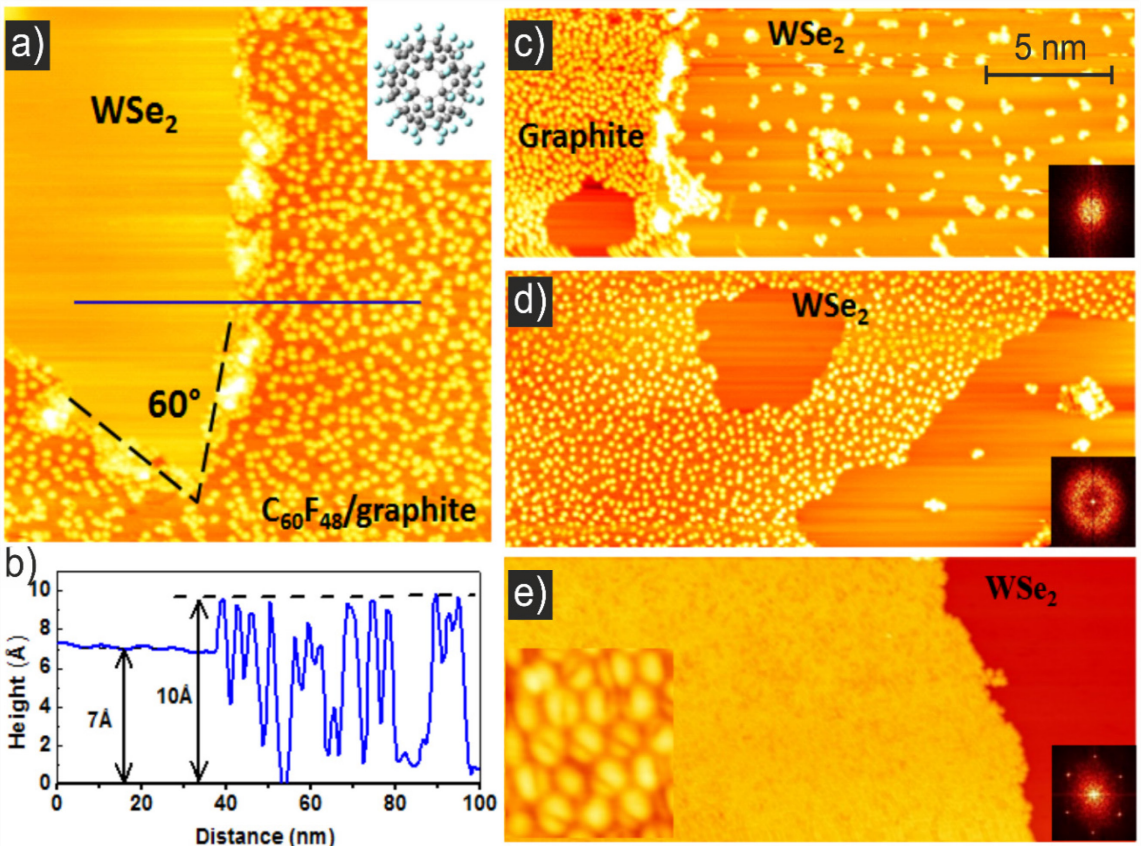

Figure 45: Different growth of $C_{60}F_{48}$ on WSe_2/graphite for different coverages. a) At very low coverages (< 1 % of a ML) the $C_{60}F_{48}$ preferentially covers the graphite substrate. The typical triangular shape of WSe_2 flakes can be seen. b) The line-cut shown in a) reveals the height of WSe_2 (7 Å, thickness of a ML) and of the $C_{60}F_{48}$ molecules (1 nm). c) For increased coverages (1-10 % of a ML) $C_{60}F_{48}$ starts to form clusters on the WSe_2. d) At coverages of > 10 % of a ML the molecules tend to stay separated and form a liquid like phase. d) When the coverage exceeds half a ML the molecules start to form close-packed islands (solid phase). Insets in c)-e) show the Fourier-transform of the corresponding images, indicating an increased order of the $C_{60}F_{48}$ film with higher coverages. Adapted from [105].

The growth of $C_{60}F_{48}$ on WSe_2 is demonstrated in Figure 45, showing STM images a), c)-e) for different $C_{60}F_{48}$ coverages. Starting the molecule deposition (< 0.01 ML coverage), the $C_{60}F_{48}$ molecules initially grow on the remaining graphite, leaving the WSe_2 uncovered, as shown in a). This indicates a lower formation energy for the $C_{60}F_{48}$/graphite interface compared to the $C_{60}F_{48}$/WSe_2 interface. Also the typical triangular shape of the WSe_2 flakes can be observed. The line-cut in a) as shown in b) allows determination of the WSe_2 and $C_{60}F_{48}$ heights. The height of the WSe_2 flakes is ≈ 7 Å, in good agreement with literature values for WSe_2 monolayers [173,174], and the height of a $C_{60}F_{48}$ molecule is about 1 nm. When the coverage is increased (> 0.01 ML) the molecules start to grow on the WSe_2 and form clusters as shown in c). Further increasing the coverage leads to a liquid like phase,

where all molecules tend to be well separated from each other as shown in d). It is unlikely that the molecules in the liquid-like phase are anchored at specific adsorption sites on WSe_2 or HOPG, as these are both atomically smooth and chemically inert. This leads to the conclusion that repulsive interactions must be present. The most likely candidate for a repulsive interaction is dipole-dipole repulsion caused by electron transfer to the molecules and concomitant dipole formation [175]. The packing motif of $C_{60}F_{48}$ molecules is then determined by the subtle competition between attractive van der Waals forces and repulsive dipole-dipole interactions [176]. At a coverage of ≈ 0.5 ML the molecules form close packed islands, covering some parts of the WSe_2 completely and leaving some parts uncovered as shown in e). As the coverage increases the dipole per molecule decreases (see DFT results later) and the attractive van-der Waals forces dominate, leading to the formation of the solid phase. This configuration of covered and uncovered regions coexisting simultaneously is perfectly suited for studying the energetic transition between doped and intrinsic regions as done in the next sections.

5.3.2 Energy Level Alignment at the 2D TMDC / Organic Interface

To obtain insight into the electronic properties of the $C_{60}F_{48}/WSe_2$/graphite heterostructure STS measurements were carried out at the transition region between uncovered and $C_{60}F_{48}$ covered WSe_2, as already shown in Figure 45 e). Figure 46 a) shows the transition region between a close-packed molecular island of $C_{60}F_{48}$ (right, bright) and bare WSe_2 (left, dark). In b) one can see an enlarged part of a) (as indicated by the white square, 8×8 nm^2) near the $C_{60}F_{48}$ island edge. A contrast variation is visible close to the island (upper right corner), indicating that the electronic properties of the WSe_2 layer are modified. A series of STS spectra, arranged in Figure 46 c), was obtained at the positions denoted by the colored triangles in Figure 46 a) and b). The dI/dV spectra obviously vary as a function of the distance d from the $C_{60}F_{48}$ island edge. As highlighted by the dashed lines in Figure 46 c), the valence band maximum (VBM) and the conduction band minimum (CBM) shift significantly as the tip moves from the pristine WSe_2 ($d > 5$ nm) towards the $C_{60}F_{48}$ island edge ($d = 0$ nm). It should be noted at this point that STS measurements directly on top of $C_{60}F_{48}$ were not possible, due to the low conductivity of the molecules. As illustrated in Figure 46 d), the VBM shifts upward towards the Fermi level from -0.84 eV to -0.22 eV ($\Delta V_{\mathrm{VBM}} = 0.62$ eV), while the CBM shifts upwards as well from $+1.10$ eV to $+1.48$ eV ($\Delta V_{\mathrm{CBM}} = 0.38$ eV). This implies a bandgap decrease of $\Delta E_{\mathrm{G}} = -0.24$ eV. The decrease of

the band gap is due to an increased electronic screening of the WSe_2 by the organic layer ($\varepsilon_{org} \approx 3$, as compared to the vacuum dielectric constant of 1) on top [177]. The data in Figure 46 thus strongly suggest that the bare WSe_2 is intrinsic, while it is *p*-doped when covered by $C_{60}F_{48}$, with a region of band bending formed between the two areas.

It was shown by the STM/STS experiments that intrinsic and *p*-doped WSe_2 patches coexist next to each other, and that the border between them forms a lateral 1D (line) intrinsic/*p*-doped interface within the semiconducting WSe_2. The gradual band bending over several nm, observed from the spatially resolved STS spectra in Figure 46 d), is due to in-plane

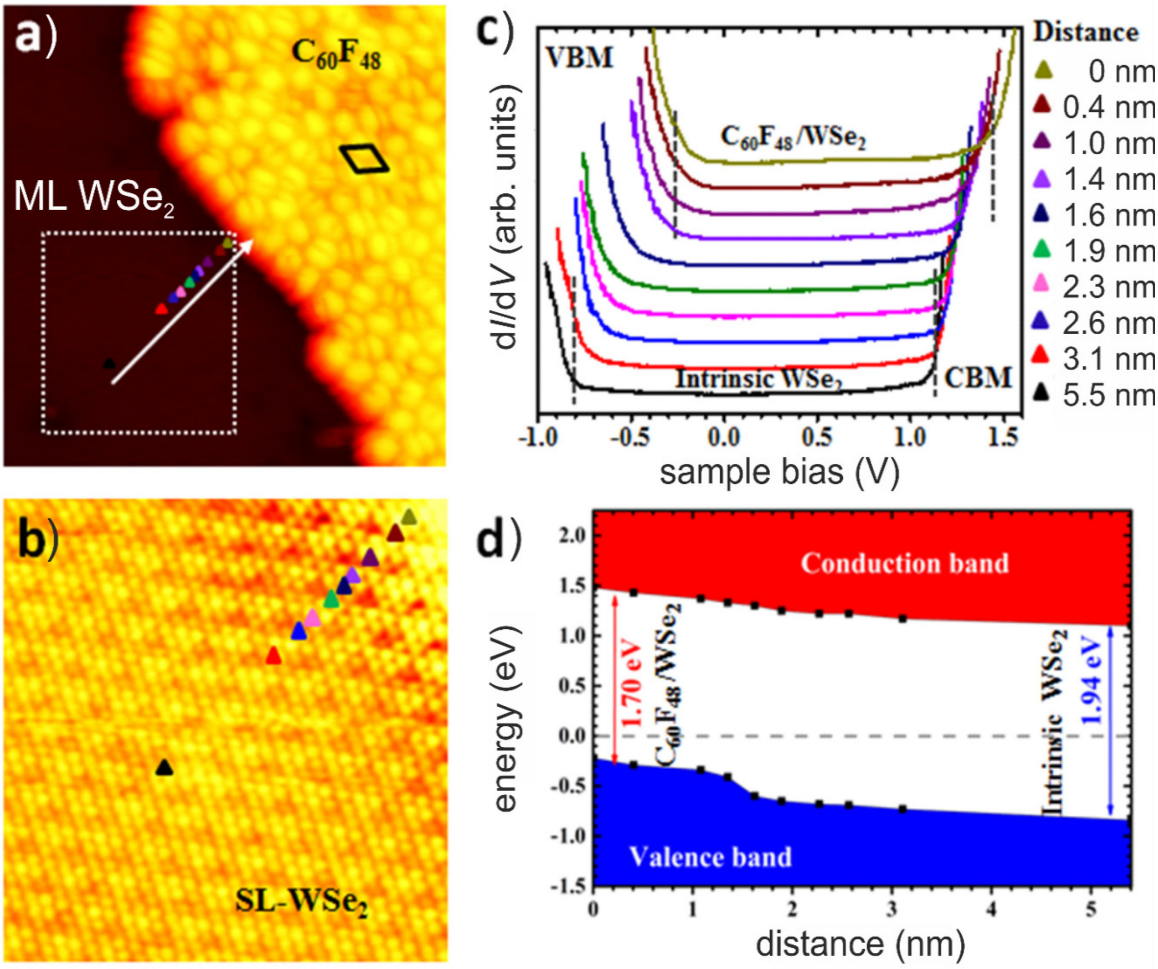

Figure 46: 1D intrinsic/*p*-doped heterojunction in SL-WSe_2. **a**) A molecular-resolved STM image shows a close-packed $C_{60}F_{48}$ island (0.5 ML) on the SL-WSe_2 (20×20 nm^2; $V_{sample} = 3.1$ V), and **b**) is the close-up corresponding to the white dotted square in a). Contrast variation is observed close to the molecular island edge (8×8 nm^2, $V_{sample} = 0.9$ V). **c**) dI/dV spectra recorded at the positions denoted by the multicolored triangles in panel **a**) and **b**) (set point: $V_{sample} = 0.9$ V, $I_{sample} = 100$ pA). The variation of the WSe_2 bandgap is getting pronounced as the STM tip approaches to the $C_{60}F_{48}$ island. **d**) Schematic diagram showing the band bending of the SL-WSe_2 as a function of the distance from the molecular island, due to the Thomas-Fermi screening effect. Adapted from [105].

electrostatic screening. Using linear Thomas-Fermi theory to describe dielectric screening in a semiconductor [178], the change of the potential ΔV as a function of distance d from a charge density perturbation is given by $\Delta V \propto e^{-d/L_{\mathrm{TF}}}$, where L_{TF} is the Thomas-Fermi screening length. Fitting the potential as shown in Figure 46 d) at four different points (shown in Appendix Fig. 7) with this equation yields $L_{\mathrm{TF}} = 2.3 \pm 0.7$ nm for the transition from the intrinsic WSe_2 side across the hole doped edge. However, it has to be kept in mind that this value is system specific and could be different for a different surrounding (e.g. for another substrate), as the electric properties of TMDCs are strongly determined by the screening due to the surrounding media [179].

It might be straightforward to presume that electron transfer from WSe_2 to $C_{60}F_{48}$ causes the *p*-doping of the 2D TMDC semiconductor. But previous observations for a molecular acceptor adsorbed on graphene have highlighted a substantial influence of the underlying substrate in tuning the electronic structure of a 2D material [44]. Thus the graphite substrate must be included in the considerations. To understand the origin of the charge transfer, Zijing Ding from National University of Singapore calculated the differential charge density (DCD) across the organic-TMDC heterostructure including the graphite substrate, as well as those of reference systems. The side-views of the DCD isosurfaces for $C_{60}F_{48}$ on a) graphite, c) ML-WSe_2 on graphite and e) freestanding ML-WSe_2 are plotted in Figure 47, respectively. Projector-augmented wave pseudopotentials, PBE functionals, van der Waals corrections and a (7×7) graphene supercell and a $(3\sqrt{3} \times 3\sqrt{3})$ WSe_2 supercell were used for the computations. The adsorption of the $C_{60}F_{48}$ molecule on a double bond in between hexagons was used in the calculations. The DCD plots reveal that the $C_{60}F_{48}$ molecule is negatively charged in all cases, and the electrons predominantly accumulate at the lower half of the molecule. In turn, all substrates are positively charged. However, the sandwiched WSe_2 single-layer in Figure 47 c) remains essentially charge-neutral. It becomes polarized, as the top Se layer facing the molecule is hole-accumulated, while the bottom Se layer facing graphite is electron-accumulated. To provide a more quantitative picture, the plane-integrated DCD, $\Delta\rho(z)$ (red), and the cumulative charge transfer $\Delta Q(z)$ (blue), are plotted in Figure 47 b), d) and f). The latter describes how much charge has been transferred from the bottom to the top at position z. The total amount of charge transfer ($\Delta Q_{\mathrm{total}}$) from graphite to $C_{60}F_{48}$ reaches $-0.40\ e$ per molecule in Figure 47 b), and reduces slightly to $-0.38\ e$ with the SL-WSe_2 interlayer in Figure 47 d). Two pronounced maxima

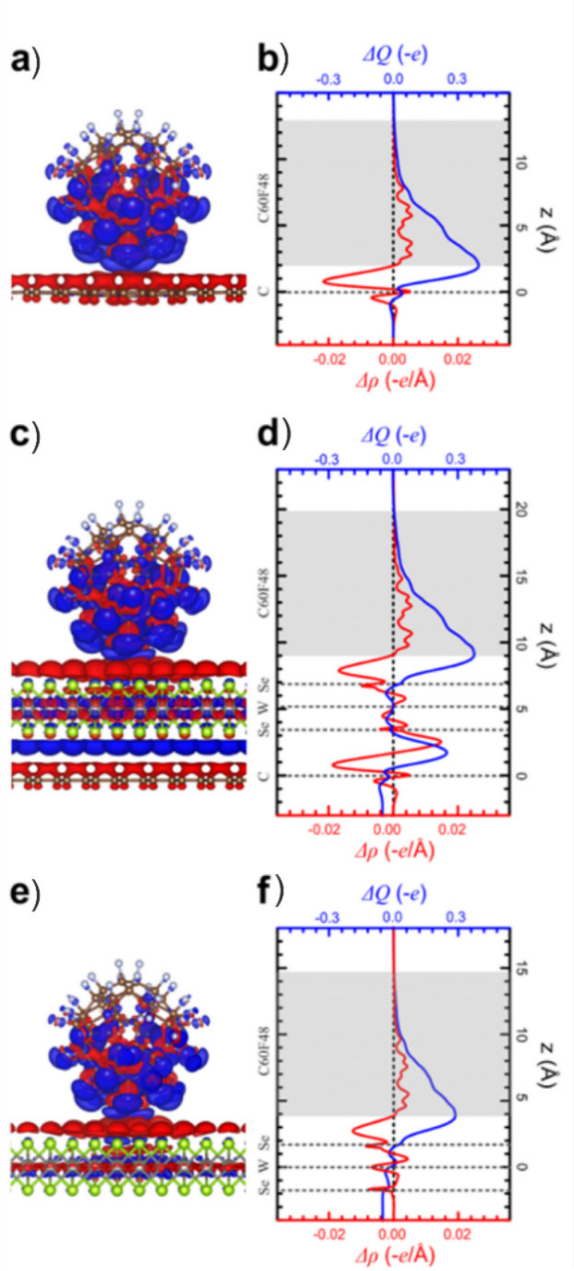

Figure 47: DFT calculations of the charge transfer at HOPG/WSe_2/$C_{60}F_{48}$ interfaces. a), c) and e) are side views of DCD isosurfaces of a $C_{60}F_{48}$ molecule on a single-layer graphene, SL-WSe_2/graphene, and SL-WSe_2, respectively. A (7×7) graphene supercell and a $(3\sqrt{3} \times 3\sqrt{3})$ WSe_2 supercell were used. Gray, green, brown and pearl gray balls represent W, Se, C and F atoms, respectively. Blue (red) represents electron accumulation (depletion) regions. b), d) and f) represent the corresponding plots of the plane-averaged $\Delta\rho(z)$ (red) and $\Delta Q(z)$ (blue). Adapted from [105].

can be observed in Figure 47 d): the top one at $-0.38\ e$ represents the charge transfer from WSe_2/graphite to $C_{60}F_{48}$, and the lower one at $-0.25\ e$ is that from graphite to $C_{60}F_{48}$/WSe_2. The difference of these two peaks, $-0.13\ e$, is the contribution from the WSe_2 interlayer, which is about half of that from the graphite substrate. Consequently, the graphite contributes about two thirds of the charge to the molecular acceptor, while the ML-WSe_2 contributes only one third, contradicting the presumption of dominant charge transfer from WSe_2 to $C_{60}F_{48}$. Due to the presence of the graphite substrate the direct charge transfer from the WSe_2 to $C_{60}F_{48}$ is significantly reduced, as the charge transfer for freestanding WSe_2 would be much larger ($-0.29\ e$ as seen in Figure 47 f). The underlying graphite substrate thus plays an important role in defining the electronic structure of the heterojunction, as speculated above. Further calculations suggest that the $C_{60}F_{48}$/WSe_2/graphite heterojunction has a charge transfer induced interfacial dipole moment of $2.65\ e$Å, which is much larger than that of $C_{60}F_{48}$/graphite without the WSe_2 interlayer ($1.70\ e$Å) and that of $C_{60}F_{48}$/WSe_2 without the graphite substrate ($1.31\ e$Å). This can be rationalized by the increased distance

between the separated charges due to the WSe_2 interlayer. The dipole field induced by the charge transfer at the heterojunction can significantly impact the electronic properties e.g., energy level alignment.

To substantiate the conclusions from STM/STS and DFT calculations, and to obtain a unified picture of the energy level alignment, PES measurements were performed to determine changes of work function, valence band and core level spectra after $C_{60}F_{48}$ deposition. The main results are shown in Figure 48. The spectra of the clean graphite substrate are shown as black dotted lines for comparison. The work function of HOPG (4.5 eV) increases by less than 0.1 eV when covered with ML-WSe_2 (labeled with 0 Å), indicating negligible charge transfer. The valence region in Figure 48 b) shows two distinct features from the ML-WSe_2 at 1.5 eV and 3.9 eV binding energy. The VB onset of the pristine ML-WSe_2, namely the lower binding energy onset of the first peak, is at 1.1 eV, slightly larger than the value of the VBM determined by STS (0.84 eV). The reason for this is the band structure of WSe_2. It is well known, both from theory and experiment, that the valence band maximum of monolayer WSe2 is located at the K-point in the Brillouin zone [180]. This energy is measured in the STS experiments. In photoemission experiments at normal emission, however, the measured VB spectra correspond to electronic states around the Γ-point. The density of states around the Γ-point is energetically deeper than that at the K-point. Therefore, it is reasonable that the VB onset measured by PES is further away from the Fermi level than the VB onset determined by STS.

After the adsorption of $C_{60}F_{48}$, the work function increases significantly, as seen by the shift of the SECO to higher kinetic energies in Figure 48 a). The work function change saturates at a nominal coverage Θ of 8 Å, which is identified as a full $C_{60}F_{48}$ monolayer coverage. The total work function increase of 1.56 eV with a $C_{60}F_{48}$ monolayer indicates the formation of an interfacial dipole induced by the charge transfer across the heterostructure, consistent with the DFT calculations. The intensities of the two WSe_2 related distinct peaks in the valence band region reduce with increasing $C_{60}F_{48}$ coverage and typical $C_{60}F_{48}$ features appear at 6 eV and 9 eV BE, as indicated in Figure 48 b). From the 20 Å SECO and valence region spectra the ionization energy of $C_{60}F_{48}$ can be determined to be 10.75 eV, in good agreement with previous reports by Smets *et al.* [181]. The C1s spectra are shown in Figure 48 c). The graphite (HOPG) peak at 284.4 eV is attenuated with increasing $C_{60}F_{48}$ coverage, but shows no energy shift. The emerging $C_{60}F_{48}$

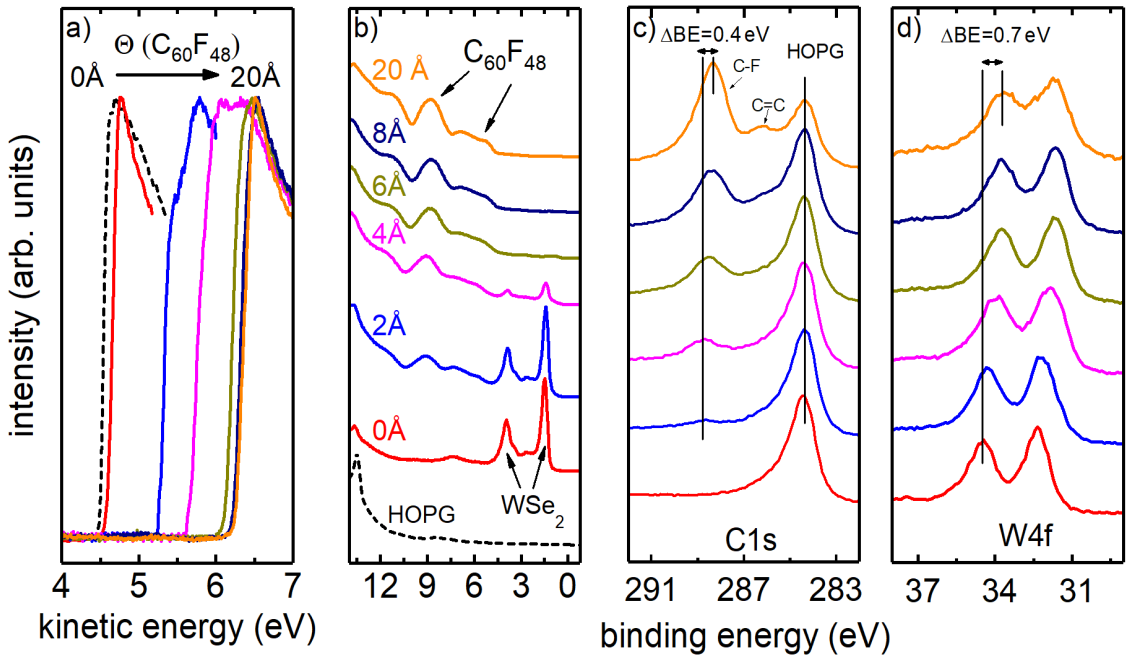

Figure 48: PES spectra of a $C_{60}F_{48}$/WSe_2/graphite heterostructure. a) The secondary electron cut-off shifts to higher kinetic energies with increasing $C_{60}F_{48}$ coverage, indicating a work function increase. b) Valence band spectra show sharp WSe_2 peaks at around 1.5 eV and 4 eV before molecular deposition (0 Å), which are strongly attenuated for coverages higher than 4 Å. The dashed black line in a) and b) shows the clean HOPG for comparison. c) C1s core level of HOPG does not shift, whereas the C1s core level of $C_{60}F_{48}$ shifts to lower binding energies for high coverages. d) W4f core levels shift by 0.7 eV to lower binding energy with increasing $C_{60}F_{48}$ coverage. Adapted from [105].

peaks at 288.7 eV (C-F bond) and 286.2 eV (C=C bond) on the other hand shift to lower binding energies by 0.4 eV with increasing $C_{60}F_{48}$ coverage. This indicates a band bending within the $C_{60}F_{48}$. The same shift is observed for the F1s peak. The W4f peak is shown exemplarily for the WSe_2 layer in Figure 48 d). It shifts gradually to lower binding energies with a total shift of 0.7 eV at full $C_{60}F_{48}$ coverage, indicating p-doping of the WSe_2 layer. The same shift is observed for the Se core levels. These shifts are in line with the gradual work function shift. Enlarged valence band spectra are shown in Figure 49 a). A pronounced shift of the VB onset to lower binding energy takes place at coverages above 4 Å. This could be connected to formation of the solid phase at 0.5 ML $C_{60}F_{48}$ coverage, as shown by STM. The valence band onset after monolayer coverage with $C_{60}F_{48}$ is at 0.35 eV below the Fermi-level. A summary of the energy shifts of all core levels, the valence band onset and the work function change is shown in Figure 49 b). The change in WSe_2 energy levels is 0.75 ± 0.1 eV to lower binding energies, in good agreement with

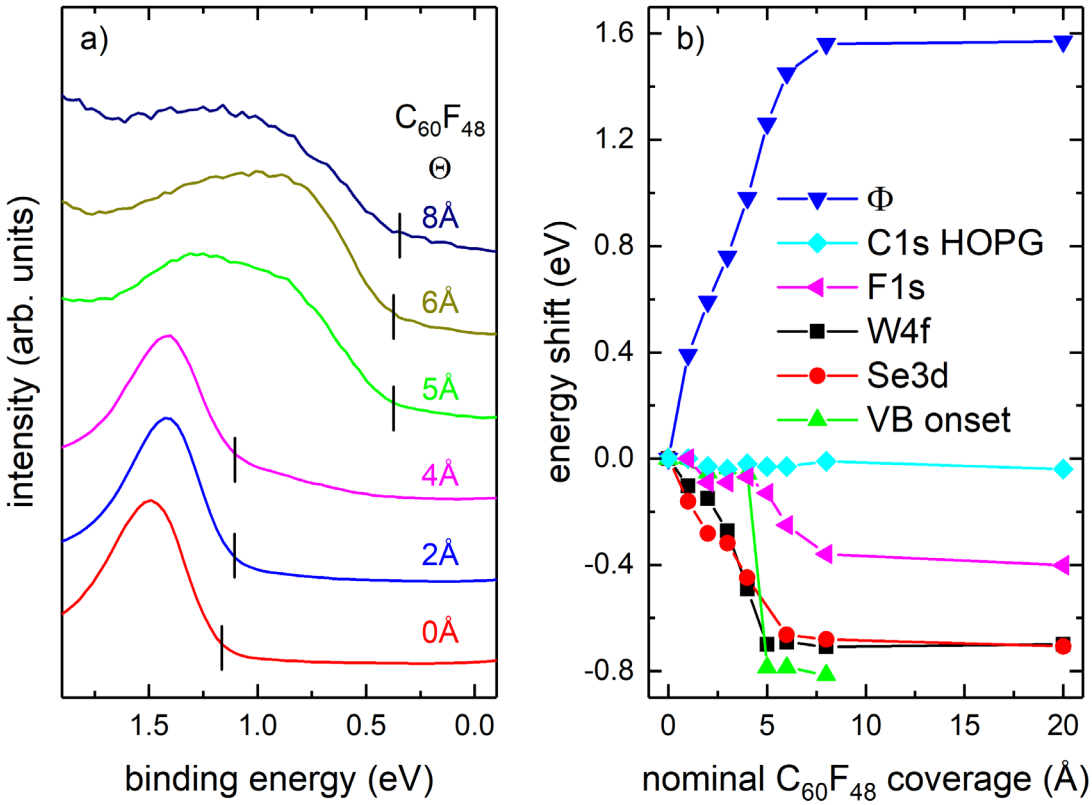

Figure 49: a) Enlarged valence band spectra of WSe_2 with increasing $C_{60}F_{48}$ coverage. The onsets determined from linear extrapolation are marked. b) Summary of the work function change and energy shifts of the valence band onset and the different core levels as a function of $C_{60}F_{48}$ coverage.

the shift in valence band onset obtained from STS measurements. This shift is about half of the total change in work function. From these results one can draw an energy diagram of the HOPG/WSe_2/$C_{60}F_{48}$ heterostructure, as shown in Figure 50. The main electron transfer to the $C_{60}F_{48}$ molecules stems from the graphite substrate. This charge separation leads to the formation of an electric field across the WSe_2 layer. The associated potential shifts all occupied energy levels of the WSe_2 closer to the Fermi-level, effectively p-doping the WSe_2 layer.

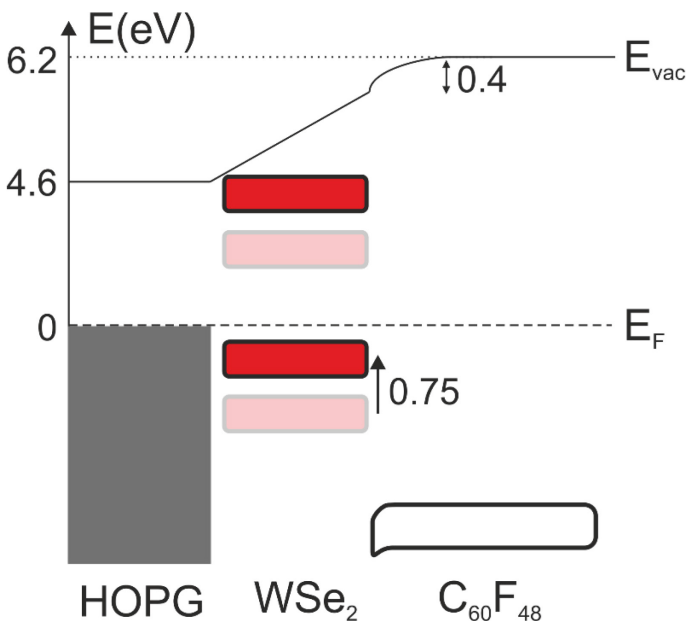

Figure 50: Schematic energy level diagram of the HOPG/ML-WSe_2/$C_{60}F_{48}$ heterostructure, as determined from PES measurements. Electron transfer from HOPG to $C_{60}F_{48}$ leads to the formation of an electric field across the WSe_2 layer. The corresponding potential shifts the energy levels of WSe_2 upwards by 0.75 eV, leading to an effective p-doping of the WSe_2 layer. The $C_{60}F_{48}$ experiences slight band bending away from the interface. The energy axis is not to scale. Transparent boxes indicate the WSe_2 levels before $C_{60}F_{48}$ deposition.

5.3.3 Performance Improvement of a Field Effect Transistor

In this section the p-doping of the WSe_2 monolayer, as fundamentally investigated in the previous sections, is employed in an actual device. Therefore a field effect transistor (FET) was fabricated on a monolayer WSe_2 flake, as described in section 4.1.2, and its electrical properties were measured before and after deposition of 20 nm $C_{60}F_{48}$. Two typical ways to characterize the electrical properties of a FET are to measure the so called *transfer characteristics* (I_{SD}-V_G, Figure 51 a)) and *output characteristics* (I_{SD}-V_{SD}, Figure 51 b) and c)). The transfer characteristics of the pristine WSe_2 shows ambipolar behavior, which can be clearly seen from the logarithmic plot in the inset of Figure 51 a). This means that both electron and hole transport are similarly present, only depending on the direction of the gate bias (hole dominated transport for negative V_G and electron dominated transport for positiv V_G), which is in line with observations from STS and PES that the Fermi-level is positioned around midgap for the intrinsic WSe_2 (compare Figure 46 d). The transport characteristic is clearly changed after deposition of 20 nm $C_{60}F_{48}$. While the hole current is increased by an order of magnitude, the electron current is decreased by almost two orders of magnitude. This is due to the induced p-doping by the $C_{60}F_{48}$, as demonstrated in

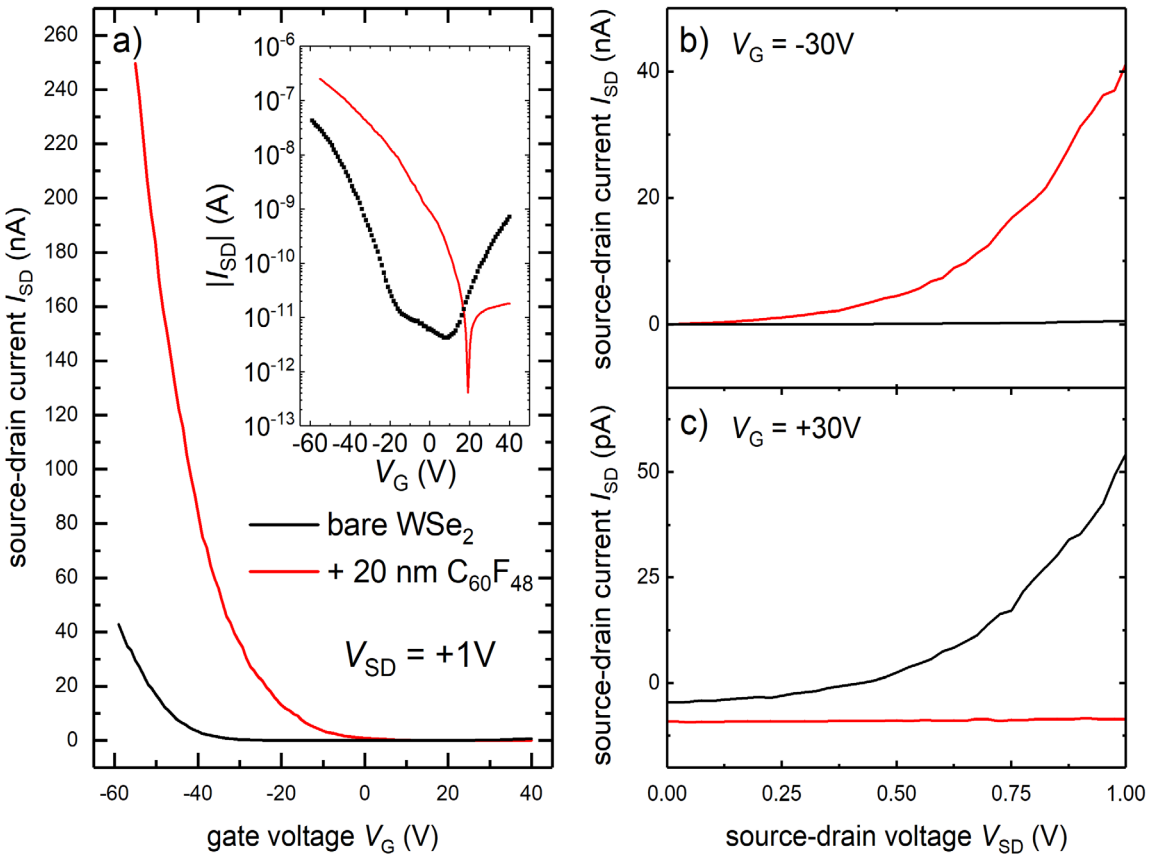

Figure 51: Electrical characteristics of a SL-WSe_2 FET without (black) and with (red) $C_{60}F_{48}$. a) Transfer characteristics (I_{SD}-V_G) of the SL-WSe_2 device with $V_{SD} = 1$ V. The inset shows a logarithmic plot of the transfer curve, indicating ambipolar conductivity before doping with $C_{60}F_{48}$. After p-doping the hole transport (negative V_G) dominates. b) and c) show the output characteristics (I_{SD}-V_{SD}) in the hole transport regime ($V_G = -30$ V) and in the electron transport regime ($V_G = +30$ V), respectively, clearly demonstrating the p-doping effect of the $C_{60}F_{48}$.

the previous sections. The output characteristics further support these findings. For a negative gate bias (hole dominated transport, Figure 51 b) a strong increase in current is observed for the doped WSe_2 with increasing source-drain bias, whereas there is no significant current flow for the intrinsic WSe_2. When reversing the gat bias (electron dominated transport, Figure 51 c)) the current increases with increasing source-drain bias for the intrinsic WSe_2, whereas it is constant for the p-doped WSe_2. Note the different scales in b) and c) (nA vs. pA). The slow increase in current with increasing source-drain voltage is an indication for high contact resistances [174],which is not surprising as the device structure was not optimized, as the aim of these measurements was the investigation of the influence of the WSe_2 doping on the device performance and not building highly efficient transistors. Changes of the contact properties to the changes of the device characteristics after $C_{60}F_{48}$ deposition can be ruled out, as the molecules were deposited on top of the

contacts and diffusion of $C_{60}F_{48}$ into the WSe_2/contact interface is very unlikely. Therefore all the described changes of the FET performance can be ascribed to a p-doping of the WSe_2, perfectly in line with observations in the previous sections.

In this chapter the change in energy levels of the transition metal dichalcogenide monolayer WSe_2 after deposition of the strong organic acceptor molecules $C_{60}F_{48}$ was investigated. Besides the effective p-doping of the TMDC, which was consistently shown by STS, PES, DFT and device characteristics, the molecules form closed monolayer islands for sub-monolayer coverage, which allowed to investigate a 1D transition between doped and undoped regions of the WSe_2. By analyzing the STS data at such a transition edge it was possible to directly determine the Thomas-Fermi screening length of the WSe_2 layer in this system, an important parameter when it comes to the design of nanoscale devices.

6 Summary, Conclusion and Outlook

The aim of this thesis was to gain a deeper understanding of the phenomena taking place at hybrid inorganic/organic interfaces, especially concerning the energy level alignment and ways to manipulate it. A strong tool to investigate such properties and also the main experimental technique used in this work, is photoelectron spectroscopy (PES). Using ultraviolet photoelectron spectroscopy (UPS), information about the valence states can be obtained and the absolute work function of samples can be determined by measuring the secondary electron cut-off (SECO). However, the evaluation of SECO spectra can be delicate for heterogeneous surfaces, as multiple cut-offs can be present. The emergence of SECO spectra with multiple cut-offs was investigated with the help of well-controlled model systems in ad 1) and an understanding of the reason for the area averaging effect as well as its consequences on the determination of ionization energies was obtained. With x-ray photoelectron spectroscopy (XPS), changes in band bending of an inorganic substrate after molecule deposition can be directly measured and distinguished from the formation of an interface dipole due to charge transfer. The influence of inorganic bulk doping and inorganic surface states on the band bending after deposition of strong organic acceptors was investigated for GaN, ZnO and F6-TCNNQ in ad 2) as well as the possible manipulation of the energy level alignment between prototypical inorganic (GaN, Si) and organic (α-NPD) semiconductors with the help of the interlayer method. Furthermore, the energy level changes of a transition metal dichalcogenide (WSe_2), a novel class of 2D materials, after deposition of the strong organic acceptor $C_{60}F_{48}$ were investigated in detail in ad 3).

Ad 1) To understand the influence of surface work function heterogeneity on the SECO spectrum measured in UPS, model systems of bilinear areas were fabricated by either microcontact printing of two different self-assembled monolayers (SAMs) on gold (stripe size ≤ 2 µm) or evaporation of gold on alumina through a shadow mask (stripe size ≥ 200 µm). By this, periodic work function differences of more than 1 eV were obtained, which were benchmarked with the help of Kelvin-probe force microscopy (KPFM). Two cut-offs could be observed in the SECO spectra in UPS, a dominant one at lower kinetic energy, whose energy depended on the area ratio of the two materials, and a smaller shoulder at higher kinetic energy, whose energetic position was independent of the area

ratio. By comparing these results to UPS results of the pure materials, to KPFM results of the bilinear structures and with electrostatic calculations based on solving the Laplace-equation, it was found that the presence of areas with locally high work function leads to the formation of a potential barrier above areas with low work function, effectively increasing the measured kinetic energy of the low kinetic energy cut-off, eventually leading to the observed area averaging effect in UPS. It was further found, both experimentally and theoretically, that this averaging effect depends on the stripe size and experimental parameters, like applied bias between sample and analyzer and distance between sample and analyzer. It was further demonstrated how heterogeneous substrates influence the determination of the ionization energy of subsequently deposited molecules. Because the averaging effect influences electrons with low kinetic energy (SECO), but not electrons with higher kinetic energy (valence region), the ionization energy determined from the sum of the low binding energy HOMO onset and the low kinetic energy cut-off is too low compared to the real ionization energy. Therefore it is recommend to use clean metal single crystals for the determination of ionization energies of unknown molecules, as it is for example known that ITO, an often used substrate for the deposition of organic molecules, can change its work function during illumination with UV light. Further studies on more complex model systems could help to understand, for instance, the growth of molecules on surfaces. Also the dependence of the SECO intensity on energy and area ratio, which leads to the fact that the high kinetic energy shoulder is often overlooked in experiment, is not fully understood yet.

Ad 2) With a combination of XPS and UPS two contributions to the work function change of inorganic semiconductors after organic molecular acceptor deposition can be determined separately: a change of the band bending inside the inorganic semiconductor, by observing shifts in the binding energy of the core levels, and the formation of an interface dipole due to a charge redistribution. By measuring these two contributions for differently Ga-doped ZnO $(000\bar{1})$ samples ($N_D = 2 \cdot 10^{17} - 6 \cdot 10^{20}$ cm^{-3}) after F6-TCNNQ deposition it was found that the doping concentration does not have a significant influence on the band bending and work function change. For all doping concentrations the work function increased by about 2 eV after deposition of a monolayer of F6-TCNNQ. The band bending changes were $0.4 - 0.7$ eV, but only due to slight differences in the initial band bending. For all doping concentrations the Fermi-level was pinned at about 0.7 eV below the conduction band. It was further found that the amount of charged molecules differs only

slightly and is in the range of $10 - 20$ % of a monolayer. This universal pinning of the Fermi-level is attributed to the presence of surface states. Using different preparation methods for the GaN (0001) surface, it was shown that a reduction of surface state density leads to a reduction of the initial band bending. Therefore, the change in band bending after acceptor molecule deposition is larger than in the presence of high surface state density, but the final pinning position remains the same and is dominated by the energetic position of the surface states, which can be attributed to Ga dangling bonds in the case of GaN (0001). A numerical model was suggested, which allows to calculate the band bending contribution as a function of doping concentration and surface state density. Although it captures the relative changes between the differently prepared GaN surfaces very well, the model still needs further extension, taking into account the energetic position of the surface states, to be able to make predictions about the absolute band bending change. Therefore experimental techniques with higher sensitivity than XPS/UPS are needed to give direct measures of the surface state density and density functional theory (DFT) could help to obtain energetic positions of the surface states. Besides these detailed findings about the work function changes after molecular acceptor deposition, these acceptors and also organic donors were used as thin interlayers to change the energetic alignment between typical inorganic (GaN, Si) and the organic semiconductor α-NPD. It is demonstrated that, for example, the hole injection barrier can be tuned by more than 2.5 eV, making the interlayer method a very strong tool for the design and improvement of hybrid devices.

Ad 3) The transition metal dichalcogenide WSe_2, grown on highly oriented pyrolytic graphite (HOPG), was characterized by scanning tunneling microscopy/spectroscopy (STM/STS), PES and DFT after deposition of the strong organic acceptor $C_{60}F_{48}$. By STM it was found that the $C_{60}F_{48}$ forms closely packed monolayer islands above a coverage of 0.5 monolayers, which is ideal to investigate the transition between undoped and doped WSe_2 regions. Electrons are transferred from the WSe_2/HOPG to the molecules, effectively p-doping the WSe_2. Using DFT, it is found that most of the electrons are transferred from the HOPG to the molecules and the WSe_2 is polarized in the resulting electric field. An energy level diagram for this system was presented based on the PES results. From STS measurements at the border of a $C_{60}F_{48}$ covered island it was found that the WSe_2 band gap decreased after $C_{60}F_{48}$ coverage, due to the additional screening of the top layer. Furthermore, the Thomas-Fermi screening length, a measure for the screening of a charge in a semiconductor and an important parameter in nano-scale devices, was determined to

be about 2 nm for this specific heterostructure. Finally, the surface doping was exploited in a field effect transistor structure, which lead to the suppression of electron transport and a reduced turn-on voltage for hole transport.

The results of this work should raise awareness of the careful evaluation of SECO data obtained by UPS. It furthermore stresses the importance of surface states on inorganic semiconductors for the energetic alignment at hybrid interfaces, which are often neglected due to the difficulty of detecting them directly. To my best knowledge, it is also the first time that the Thomas-Fermi screening length of WSe_2 was determined directly from experiment, a parameter which will help to improve the design of nano-scale devices based on 2D semiconductors.

7 Bibliography

[1] J.E. Lilienfeld, *Method and apparatus for controlling electric currents*, US1926014036319261008 (1930).

[2] H. Koezuka, A. Tsumura and T. Ando, *Field-effect transistor with polythiophene thin film*, Synthetic Metals 18 (1987), pp. 699–704.

[3] R. Schlesinger, F. Bianchi, S. Blumstengel, C. Christodoulou, R. Ovsyannikov, B. Kobin et al., *Efficient light emission from inorganic and organic Semiconductor hybrid structures by energy-level tuning*, Nature Communications 6 (2015), pp. 6754.

[4] F. Yang and Z. Guo, *Fabrication of inorganic-organic hybrid TiO_2@PDA@CuO composite nanoparticles and its special wettable, gas sensing and photocatalytic behaviors*, Materials Letters 217 (2018), pp. 320–323.

[5] C.B. Bucur, M. Jones, M. Kopylov, J. Spear and J. Muldoon, *Inorganic-organic layer by layer hybrid membranes for lithium-sulfur batteries*, Energy Environ. Sci. 10 (2017), pp. 905–911.

[6] T.M. Brenner, D.A. Egger, L. Kronik, G. Hodes and D. Cahen, *Hybrid organic-inorganic perovskites: low-cost semiconductors with intriguing charge-transport properties*, Nature Reviews Materials 1 (2016), pp. 15007.

[7] J. Hwang, A. Wan and A. Kahn, *Energetics of metal-organic interfaces: New experiments and assessment of the field*, Materials Science and Engineering: R: Reports 64 (2009), pp. 1–31.

[8] N. Koch, *Organic electronic devices and their functional interfaces*, ChemPhysChem 8 (2007), pp. 1438–1455.

[9] R. Schlesinger, *Energy-Level Control at Hybrid Inorganic/Organic Semiconductor Interfaces*, Springer International Publishing, 2017.

[10] F. Bloch, *Über die Quantenmechanik der Elektronen in Kristallgittern*, Zeitschrift für Physik (1929), pp. 555–600.

[11] A. Sommerfeld and H. Bethe, *Handbuch der Physik (Elektronentheorie der Metalle)*, Vol. 24, Springer Verlag, Heidelberg, 1933.

[12] R. de L. Kronig and W.G. Penney, *Quantum Mechanics of Electrons in Crystal Lattices*, Proceedings of the Royal Society of London. Series A 130 (1931), pp. 499–513.

[13] M. Grundmann, *The physics of semiconductors: An introduction including devices and nanophysics*, 1st ed.Springer Berlin Heidelberg, 2006.

[14] N.W. Ashcroft and N.D. Mermin, *Solid State Physics*, Cengage Learning, 2011.

[15] C. Wöll, *Physical and Chemical Aspects of Organic Electronics: From Fundamentals to Functioning Devices*, Wiley-VCH, 2009.

[16] M. Schwoerer and H.C. Wolf, *Organic Molecular Solids*, Wiley-VCH, 2008.

[17] J.E. Lennard-Jones, *The electronic structure of some diatomic molecules*, Trans. Faraday Soc. 25 (1929), pp. 668–686.

[18] E. Hückel, *Quantentheoretische Beiträge zum Problem der aromatischen und ungesättigten Verbindungen. III*, Zeitschrift für Physik 76 (1932), pp. 628–648.

[19] E. Hückel, *Quantentheoretische Beiträge zum Benzolproblem*, Zeitschrift für Physik 70 (1931), pp. 204–286.

[20] E. Hückel, *Zur Quantentheorie der Doppelbindung*, Zeitschrift für Physik 60 (1930), pp. 423–456.

[21] A. Streitwieser, *Pioneers of Quantum Chemistry: Molecular Orbital Theory for Organic Chemists*, in *Pioneers of Quantum Chemistry*, American Chemical Society, 2013, pp. 275–300.

[22] R.O. Jones, *Density functional theory: Its origins, rise to prominence, and future*, Rev. Mod. Phys. 87 (2015), pp. 897–923.

[23] W. Kohn, *Nobel Lecture: Electronic structure of matter-wave functions and density functionals*, Rev. Mod. Phys. 71 (1999), pp. 1253–1266.

[24] M. Oehzelt, N. Koch and G. Heimel, *Organic semiconductor density of states controls the energy level alignment at electrode interfaces*, Nature Communications 5 (2014), pp. 4174.
[25] T. Sueyoshi, H. Fukagawa, M. Ono, S. Kera and N. Ueno, *Low-density band-gap states in pentacene thin films probed with ultrahigh-sensitivity ultraviolet photoelectron spectroscopy*, Applied Physics Letters 95 (2009), pp. 183303.
[26] P.P. Altermatt, A. Schenk, F. Geelhaar and G. Heiser, *Reassessment of the intrinsic carrier density in crystalline silicon in view of band-gap narrowing*, Journal of Applied Physics 93 (2003), pp. 1598–1604.
[27] P. Hofmann, *Solid State Physics: An Introduction*, Wiley-VCH, 2015.
[28] J.E. de la Cerda-Pedro, R. Arcos-Ramos, M. Maldonado-Dominguez, S. Rojas-Lima, M. Romero-Avila, M.P. Carreon-Castro et al., *Engineering organic semiconducting solids. Multicomponent access to crystalline 3-(4-aryl-1,2,3-triazolyl)coumarins*, CrystEngComm 18 (2016), pp. 5562–5571.
[29] S. Hotta, T. Yamao, S.Z. Bisri, T. Takenobu and Y. Iwasa, *Organic single-crystal light-emitting field-effect transistors*, J. Mater. Chem. C 2 (2014), pp. 965–980.
[30] K.-I. Nakayama, M. Yokoyama, Y.-J. Pu and J. Kido, *Organic Field-Effect Transistors Using Hetero-Layered Structure with OLED Materials*, in *Organic Light Emitting Diode - Material, Process and Devices*, S.H. Ko, ed., InTech, Rijeka, 2011, .
[31] X. Lin, B. Wegner, K.M. Lee, M.A. Fusella, F. Zhang, K. Moudgil et al., *Beating the thermodynamic limit with photo-activation of n-doping in organic semiconductors*, Nature Materials 16 (2017), pp. 1209–2015.
[32] V. Coropceanu, J. Cornil, D.A. da Silva Filho, Y. Olivier, R. Silbey and J.-L. Brédas, *Charge Transport in Organic Semiconductors*, Chemical Reviews 107 (2007), pp. 926–952.
[33] M.L. Tietze, J. Benduhn, P. Pahner, B. Nell, M. Schwarze, H. Kleemann et al., *Elementary steps in electrical doping of organic semiconductors*, Nature Communications 9 (2018), pp. 1182.
[34] O.T. Hofmann, P. Rinke, M. Scheffler and G. Heimel, *Integer versus Fractional Charge Transfer at Metal(/Insulator)/Organic Interfaces: Cu(/NaCl)/TCNE*, ACS Nano 9 (2015), pp. 5391–5404.
[35] N.B. Kotadiya, H. Lu, A. Mondal, Y. Ie, D. Andrienko, P.M.W. Blom et al., *Universal strategy for Ohmic hole injection into organic semiconductors with high ionization energies*, Nature Materials (2018), pp. 329–334.
[36] W.-L. Seah, C.G. Tang, R.-Q. Png, V. Keerthi, C. Zhao, H. Guo et al., *Interface Doping for Ohmic Organic Semiconductor Contacts Using Self-Aligned Polyelectrolyte Counterion Monolayer*, Advanced Functional Materials 27 (2017), pp. 1606291.
[37] H. Glowatzki, B. Bröker, R.-P. Blum, O.T. Hofmann, A. Vollmer, R. Rieger et al., *Soft" Metallic Contact to Isolated C"60 Molecules*, Nano Letters 8 (2008), pp. 3825–3829.
[38] L. Romaner, G. Heimel, J.-L. Brédas, A. Gerlach, F. Schreiber, R.L. Johnson et al., *Impact of Bidirectional Charge Transfer and Molecular Distortions on the Electronic Structure of a Metal-Organic Interface*, Phys. Rev. Lett. 99 (2007), pp. 256801.
[39] H. Wang, P. Amsalem, G. Heimel, I. Salzmann, N. Koch and M. Oehzelt, *Band-Bending in Organic Semiconductors: the Role of Alkali-Halide Interlayers*, Advanced Materials 26 (2014), pp. 925–930.
[40] Z. Zhang and J. J. T. Yates, *Band Bending in Semiconductors: Chemical and Physical Consequences at Surfaces and Interfaces*, Chemical Reviews 112 (2012), pp. 5520–5551.
[41] O.V. Molodtsova, M. Grobosch, M. Knupfer and V.Y. Aristov, *Consistent experimental determination of the charge neutrality level and the pillow effect at metal/organic interfaces*, Applied Physics Letters 91 (2007), pp. 244103.
[42] H. Vázquez, Y.J. Dappe, J. Ortega and F. Flores, *A unified model for metal/organic interfaces: IDIS, "pillow" effect and molecular permanent dipoles*, Applied Surface Science 254 (2007), pp. 378–382.

[43] P. Amsalem, J. Niederhausen, A. Wilke, G. Heimel, R. Schlesinger, S. Winkler et al., *Role of charge transfer, dipole-dipole interactions, and electrostatics in Fermi-level pinning at a molecular heterojunction on a metal surface*, Phys. Rev. B 87 (2013), pp. 035440.

[44] C. Christodoulou, A. Giannakopoulos, G. Ligorio, M. Oehzelt, M. Timpel, J. Niederhausen et al., *Tuning the Electronic Structure of Graphene by Molecular Dopants: Impact of the Substrate*, ACS Applied Materials & Interfaces 7 (2015), pp. 19134–19144.

[45] J. Niederhausen, P. Amsalem, A. Wilke, R. Schlesinger, S. Winkler, A. Vollmer et al., *Doping of C_{60} (sub)monolayers by Fermi-level pinning induced electron transfer*, Phys. Rev. B 86 (2012), pp. 081411.

[46] I.G. Hill, A.J. Mäkinen and Z.H. Kafafi, *Distinguishing between interface dipoles and band bending at metal/tris-(8-hydroxyquinoline) aluminum interfaces*, Applied Physics Letters 77 (2000), pp. 1825–1827.

[47] Irfan, M. Zhang, H. Ding, C.W. Tang and Y. Gao, *Strong interface p-doping and band bending in C_{60} on MoOx*, Org. Electron. 12 (2011), pp. 1588–1593.

[48] M.T. Greiner, M.G. Helander, W.-M. Tang, Z.-B. Wang, J. Qiu and Z.-H. Lu, *Universal energy-level alignment of molecules on metal oxides*, Nat. Mater. 11 (2012), pp. 76–81.

[49] S. Winkler, N. Koch, J. Frisch, R. Schlesinger, M. Oehzelt, R. Rieger et al., *The impact of local work function variations on fermi level pinning of organic semiconductors*, The Journal of Physical Chemistry C 117 (2013), pp. 22285–22289.

[50] S. Braun, W.R. Salaneck and M. Fahlman, *Energy-Level Alignment at Organic/Metal and Organic/Organic Interfaces*, Advanced Materials 21 (2009), pp. 1450–1472.

[51] J.-P. Yang, L.-T. Shang, F. Bussolotti, L.-W. Cheng, W.-Q. Wang, X.-H. Zeng et al., *Fermi-level pinning appears upon weak electrode-organic contact without gap states: A universal phenomenon*, Organic Electronics 48 (2017), pp. 172–178.

[52] S. Braun, W. Osikowicz, Y. Wang and W.R. Salaneck, *Energy level alignment regimes at hybrid organic-organic and inorganic-organic interfaces*, Organic Electronics 8 (2007), pp. 14–20.

[53] J. Bardeen, *Surface States and Rectification at a Metal Semi-Conductor Contact*, Phys. Rev. 71 (1947), pp. 717–727.

[54] W. Shockley, *On the Surface States Associated with a Periodic Potential*, Phys. Rev. 56 (1939), pp. 317–323.

[55] I.E. Tamm, *Über eine mögliche Art der Elektronenbindung an Kristalloberflächen*, Phys. Z. Sowjetunion 1 (1932), pp. 733–736.

[56] A. Einstein, *Concerning an Heuristic Point of View Toward the Emission and Transformation of Light*, Annalen der Physik 17 (1905), pp. 132–148.

[57] S. Hüfner, *Photoelectron Spectroscopy: Principles and Applications*, Springer, 2003.

[58] T. Koopmans, *Über die Zuordnung von Wellenfunktionen und Eigenwerten zu den einzelnen Elektronen eines Atoms*, Physica 1 (1934), pp. 104–113.

[59] M. Magnuson, *Electronic structure studies using resonant x-ray and photoemission spectroscopy*, Uppsala University, 1999.

[60] M. P., H. C. and O. I., *Determination of attenuation lengths of photoelectrons in aluminium and aluminium oxide by angle-dependent x-ray photoelectron spectroscopy*, Surface and Interface Analysis 20 (1993), pp. 923–929.

[61] M.P. Seah and W.A. Dench, *Quantitative electron spectroscopy of surfaces: A standard data base for electron inelastic mean free paths in solids*, Surface and Interface Analysis 1 (1979), pp. 2–11.

[62] A. Proctor and P.M.A. Sherwood, *Data analysis techniques in x-ray photoelectron spectroscopy*, Analytical Chemistry 54 (1982), pp. 13–19.

[63] D.A. Shirley, *High-Resolution X-Ray Photoemission Spectrum of the Valence Bands of Gold*, Phys. Rev. B 5 (1972), pp. 4709–4714.

[64] J. Végh, *The Shirley background revised*, Journal of Electron Spectroscopy and Related Phenomena 151 (2006), pp. 159–164.

[65] J.C. Fuggle and S.F. Alvarado, *Core-level lifetimes as determined by x-ray photoelectron spectroscopy measurements*, Physical Review A 22 (1980), pp. 1615–1624.

[66] J.J. Olivero and R.L. Longbothum, *Empirical fits to the Voigt line width: A brief review*, Journal of Quantitative Spectroscopy and Radiative Transfer 17 (1977), pp. 233–236.
[67] J.F. Moulder, W.F. Stickle, P.E. Sobol and K.D. Bomben, *Handbook of X-ray Photoelectron Spectroscopy*, Physical Electronics, Inc., 1995.
[68] H. R., S. P. and S. R., *Improved accuracy of quantitative XPS analysis using predetermined spectrometer transmission functions with UNIFIT 2004*, Surface and Interface Analysis 37 (2004), pp. 589–607.
[69] G. Binnig, C.F. Quate and C. Gerber, *Atomic Force Microscope*, Phys. Rev. Lett. 56 (1986), pp. 930–933.
[70] G. Haugstad, *Atomic Force Microscopy: Understanding Basic Modes and Advanced Applications*, John Wiley & Sons, Inc., 2012.
[71] J. Shi, Y. Hu, S. Hu, J. Ma and C. Su, *Method and Apparatus of Using Peak Force Tapping Mode to Measure Physical Properties of a Sample*, 2012, .
[72] W. Melitz, J. Shen, A.C. Kummel and S. Lee, *Kelvin probe force microscopy and its application*, Surface Science Reports (2011), .
[73] U. Zerweck, C. Loppacher, T. Otto, S. Grafström and L.M. Eng, *Accuracy and resolution limits of Kelvin probe force microscopy*, Physical Review B 71 (2005), pp. 125424.
[74] C.J. Chen, *Introduction to Scanning Tunneling Microscopy*, Oxford Series in Optical and Imaging SciencesOxford University Press, 1993.
[75] A. Kumar, H.A. Biebuyck and G.M. Whitesides, *Patterning Self-Assembled Monolayers: Applications in Materials Science*, Langmuir 10 (1994), pp. 1498–1511.
[76] T.W. Odom, J.C. Love, D.B. Wolfe, K.E. Paul and G.M. Whitesides, *Improved Pattern Transfer in Soft Lithography Using Composite Stamps*, Langmuir 18 (2002), pp. 5314–5320.
[77] H. Schmid and B. Michel, *Siloxane Polymers for High-Resolution, High-Accuracy Soft Lithography*, Macromolecules 33 (2000), pp. 3042–3049.
[78] T. Lenz, T. Schmaltz, M. Novak and M. Halik, *Self-Assembled Monolayer Exchange Reactions as a Tool for Channel Interface Engineering in Low-Voltage Organic Thin-Film Transistors*, Langmuir 28 (2012), pp. 13900–13904.
[79] R.K. Smith, P.A. Lewis and P.S. Weiss, *Patterning Self-Assembled monolayers*, Prog. Surf. Sci. 75 (2004), pp. 1.
[80] T.E. Balmer, H. Schmid, R. Stutz, E. Delamarche, B. Michel, N.D. Spencer et al., *Diffusion of Alkanethiols in PDMS and its Implications on Microcontact Printing (μCP)*, Langmuir 21 (2005), pp. 622–632.
[81] I. Bergmair, M. Mühlenberger, E. Lausecker, K. Hingerl and R.Schöftner, *Diffusion of thiols during microcontact printing with rigid stamps*, Microelectronic Engineering 87 (2010), pp. 848–850.
[82] E. Delamarche, H. Schmid, A. Bietsch, N.B. Larsen, H. Rothuizen, B. Michel et al., *Transport Mechanisms of Alkanethiols during Microcontact Printing on Gold*, The Journal of Physical Chemistry B 102 (1998), pp. 3324–3334.
[83] M. Leszczynski, H. Teisseyre, T. Suski, I. Grzegory, M. Bockowski, J. Jun et al., *Lattice parameters of gallium nitride*, Applied Physics Letters 69 (1996), pp. 73–75.
[84] T. Ambridge and M.M. Faktor, *An automatic carrier concentration profile plotter using an electrochemical technique*, Journal of Applied Electrochemistry 5 (1975), pp. 319–328.
[85] A.N. Hattori, K. Endo, K. Hattori and H. Daimon, *Surface treatments toward obtaining clean GaN(0001) from commercial hydride vapor phase epitaxy and metal-organic chemical vapor deposition substrates in ultrahigh vacuum*, Appllied Surface Science 256 (2010), pp. 4745–4756.
[86] S.W. King, J.P. Barnak, M.D. Bremser, K.M. Tracy, C. Ronning, R.F. Davis et al., *Cleaning of AlN and GaN surfaces*, Journal of Applied Physics 84 (1998), pp. 5248–5260.
[87] K.M. Tracy, W.J. Mecouch, R.F. Davis and R.J. Nemanich, *Preparation and characterization of atomically clean, stoichiometric surfaces of n- and p-type GaN(0001)*, Journal of Applied Physics 94 (2003), pp. 3163–3172.

[88] R. Schlesinger, Y. Xu, O.T. Hofmann, S. Winkler, J. Frisch, J. Niederhausen et al., *Controlling the work function of ZnO and the energy-level alignement at the interface to organic semiconductors with a molecular electron acceptor*, Physical Review B 87 (2013), pp. 155311.

[89] K. Harafuji and K. Kawamura, *Sputtering Yield as a Function of Incident Ion Energy and Angle in Wurtzite-Type GaN Crystal*, Japanese Journal of Applied Physics 47 (2008), pp. 1536.

[90] M. Mishra, S. Krishna, P. Rastogi, N. Aggarwal, A.K.S. Chauhan, L. Goswami et al., *New Approach to Clean GaN Surfaces*, Materials Focus 3 (2014), pp. 218–223.

[91] R.B. Heller, J. McGannon and A.H. Weber, *Precision Determination of the Lattice Constants of Zinc Oxide*, Journal of Applied Physics 21 (1950), pp. 1283–1284.

[92] V. Srikant and D.R. Clarke, *On the optical band gap of zinc oxide*, Journal of Applied Physics 83 (1998), pp. 5447–5451.

[93] J.-K. Huang, J. Pu, C.-L. Hsu, M.-H. Chiu, Z.-Y. Juang, Y.-H. Chang et al., *Large-Area Synthesis of Highly Crystalline WSe_2 Monolayers and Device Applications*, ACS Nano 8 (2014), pp. 923–930.

[94] P.K. Koech, A.B. Padmaperuma, L. Wang, J.S. Swensen, E. Polikarpov, J.T. Darsell et al., *Synthesis and application of 1,3,4,5,7,8-Hexafluorotetracyanonaphthoquinodimethane (F6-TNAP): a conductivity dopant for organic light-emitting devices*, Chemistry of Materials 22 (2010), pp. 3926–3932.

[95] H. Méndez, G. Heimel, S. Winkler, J. Frisch, A. Opitz, K. Sauer et al., *Charge-transfer crystallites as molecular electrical dopants*, Nature Communications 6 (2015), pp. 8560.

[96] R. Mitsumoto, T. Araki, E. Ito, Y. Ouchi, K. Seki, K. Kikuchi et al., *Electronic Structures and Chemical Bonding of Fluorinated Fullerenes Studied by NEXAFS, UPS, and Vacuum-UV Absorption Spectroscopies*, The Journal of Physical Chemistry A 102 (1998), pp. 552–560.

[97] S.K. Mohapatra, A. Fonari, C. Risko, K. Yesudas, K. Moudgil, J.H. Delcamp et al., *Dimers of Nineteen-Electron Sandwich Compounds: Crystal and Electronic Structures, and Comparison of Reducing Strengths*, Chemistry - A European Journal 20 (2014), pp. 15385–15394.

[98] G. Sauerbrey, *Verwendung von Schwingquarzen zur Wägung dünner Schichten und zur Mikrowägung*, Zeitschrift für Physik 155 (1959), pp. 206–222.

[99] J.D. Andrade, *X-ray Photoelectron Spectroscopy (XPS)*, in *Surface and Interfacial Aspects of Biomedical Polymers*, J.D. Andrade, ed., Springer US, 1985, pp. 105–195.

[100] T. Schultz, T. Lenz, N. Kotadiya, G. Heimel, G. Glasser, R. Berger et al., *Reliable Work Function Determination of Multicomponent Surfaces and Interfaces: The Role of Electrostatic Potentials in Ultraviolet Photoelectron Spectroscopy*, Advanced Materials Interfaces 4 (2017), pp. 1700324.

[101] T. Schultz, P. Amsalem, N. Kotadiya, T. Lenz, P.W.M. Blom and N. Koch, *Importance of substrate work function homogeneity for reliable ionization energy determination by photoelectron spectroscopy*, Submitted to Physica Status Solidi B (2018), .

[102] T. Schultz, R. Schlesinger, J. Niederhausen, F. Henneberger, S. Sadofev, S. Blumstengel et al., *Tuning the work function of GaN with organic molecular acceptors*, Phys. Rev. B 93 (2016), pp. 125309.

[103] T. Schultz, J. Niederhausen, R. Schlesinger, S. Sadofev and N. Koch, *Impact of surface states and bulk doping level on hybrid inorganic/organic semiconductor interface energy levels*, Journal of Applied Physics 123 (2018), pp. 245501.

[104] T. Schultz, S. Barlow, S.R. Marder and N. Koch, *Ultimate energy level alignment tuning at inorganic/organic semiconductor heterojunctions*, 2018, .

[105] Z. Song, T. Schultz, Z. Ding, B. Lei, C. Han, P. Amsalem et al., *Electronic Properties of a 1D Intrinsic/p-Doped Heterojunction in a 2D Transition Metal Dichalcogenide Semiconductor*, ACS Nano 11 (2017), pp. 9128–9135.

[106] D. Cahen, A. Kahn and E. Umbach, *Energetics of molecular interfaces*, Materials Today 8 (2005), pp. 32–41.

[107] A. Kahn, *Fermi level, work function and vacuum level*, Materials Horizon 3 (2016), pp. 7–10.
[108] J.B. Hudson, *Surface Science: An Introduction*, John Wiley & Sons, Inc., 1998.
[109] M. Prutton, *Electronic properties of surfaces*, Adam Hilger Ltd., 1984.
[110] D.P. Woodruff and T.A. Delchar, *Modern Techniques of Surface Science*, Cambridge University Press, 1994.
[111] L. Aversa, R. Verucchi, R. Tatti, F.V.D. Girolamo, M. Barra, F. Ciccullo et al., *Surface doping in T6/PDI-8CN2 heterostructures investigated by transport and photoemission measurements*, Appl. Phy. Lett. 101 (2012), pp. 233504.
[112] A. Tada, Y. Geng, Q. Wei, K. Hashimoto and K. Tajima, *Tailoring organic heterojunction interfaces in bilayer polymer photovoltaic devices*, Nat. Mater. 10 (2011), pp. 450–455.
[113] T. Wang, T.R. Kafle, B. Kattel, Q. Liu, J. Wu and W.-L. Chan, *Growing Ultra-flat Organic Films on Graphene with a Face-on Stacking via Moderate Molecule-Substrate Interaction*, Sci. Rep. 6 (2016), pp. 28895.
[114] M.G. Helander, M.T. Greiner, Z.B. Wang and Z.H. Lu, *Pitfalls in measuring work function using photoelectron spectroscopy*, Applied Surface Science 256 (2010), pp. 2602–2605.
[115] A. Sharma, R. Berger, D.A. Lewis and G.G. Andersson, *Invisible high work function materials on heterogeneous surfaces*, Applied Surface Science 327 (2015), pp. 22–26.
[116] T. Sugiyama, M. Aida, N. Ueno and T. Munakata, *Photoemission microscopy for surface states of copper measured at different photoelectron energies*, Journal of Electron Spectroscopy and Related Phenomena 144–147 (2005), pp. 1167–1169.
[117] T. Sugiyama, T. Sasaki, S. Kera, N. Ueno and T. Munakata, *Photoemission microspectroscopy and imaging of bilayer islands formed in monolayer titanyl phthalocyanine films*, Chemical Physics Letters 449 (2007), pp. 319–322.
[118] D.M. Alloway, M. Hofmann, D.L. Smith, N.E. Gruhn, A.L. Graham, R. Colorado et al., *Interface Dipoles Arising from Self-Assembled Monolayers on Gold:UV-Photoemission Studies of Alkanethiols and Partially Fluorinated Alkanethiols*, The Journal of Physical Chemistry B 107 (2003), pp. 11690–11699.
[119] S. Barbet, M. Popoff, H. Diesinger, D. Deresmes, D. Théron and T. Mélin, *Cross-talk artefacts in Kelvin probe force microscopy imaging: A comprehensive study*, Journal of Applied Physics 115 (2014), pp. 144313.
[120] X. Li, Z. Zhang and V.E. Henrich, *Inelastic electron background function for ultraviolet photoelectron spectra*, J. Electron Spectrosc. Telat. Phenom. 63 (1993), pp. 253–265.
[121] J.J. Scholtz, D. Dijkkamp and R.W.A. Schmitz, *Secondary electron emission properties*, Philips J. Res. 50 (1996), pp. 375–389.
[122] S. Ogawa and Y. Takakuwa, *Simultaneous observation of oxygen uptake curves and electronic states during room-temperature oxidation on Si(001) surfaces by real-time ultraviolet photoelectron spectroscopy*, Surface Science 601 (2007), pp. 3838–3842.
[123] R. Schlaf, H. Murata and Z.. Kafafi, *Work function measurements on indium tin oxide films*, Journal of Electron Spectroscopy and Related Phenomena 120 (2001), pp. 149–154.
[124] M. Brendel, S. Krause, A. Steindamm, A.K. Topczak, S. Sundarraj, P. Erk et al., *The Effect of Gradual Fluorination on the Properties of FnZnPc Thin Films and FnZnPc/C_{60} Bilayer Photovoltaic Cells*, Advanced Functional Materials 25 (2015), pp. 1565–1573.
[125] S. Duhm, I. Salzmann, R.L. Johnson and N. Koch, *Electronic non-equilibrium conditions at C_{60}/pentacene heterostructures*, Journal of Electron Spectroscopy and Related Phenomena 174 (2009), pp. 40–44.
[126] C. Wang, I. Irfan, A.J. Turinske and Y. Gao, *Pinning of fullerene lowest unoccupied molecular orbital edge at the interface with standing up copper phthalocyanine*, Thin Solid Films 525 (2012), pp. 64–67.
[127] W. Gao and A. Kahn, *Effect of electrical doping on molecular level alignment at organic-organic heterojunctions*, Applied Physics Letters 82 (2003), pp. 4815–4817.
[128] M.G. Helander, Z.B. Wang, J. Qiu, M.T. Greiner, D.P. Puzzo, Z.W. Liu et al., *Chlorinated Indium Tin Oxide Electrodes with High Work Function for Organic Device Compatibility*, Science 332 (2011), pp. 944–947.

[129] I.G. Hill and A. Kahn, *Organic semiconductor heterointerfaces containing bathocuproine*, Journal of Applied Physics 86 (1999), pp. 4515–4519.
[130] A.J. Mäkinen, I.G. Hill and Z.H. Kafafi, *Vacuum level alignment in organic guest-host systems*, Journal of Applied Physics 92 (2002), pp. 1598–1603.
[131] S. Zhong, J.Q. Zhong, H.Y. Mao, J.L. Zhang, J.D. Lin and W. Chen, *The role of gap states in the energy level alignement at the organic-organic heterojunction interfaces*, Physical Chemistry Chemical Physics 14 (2012), pp. 14127–14141.
[132] N. Marinova, S. Valero and J.L. Delgado, *Organic and perovskite solar cells: Working principles, materials and interfaces*, Journal of Colloid and Interface Science 488 (2017), pp. 373–389.
[133] B. Bröker, R. Blum, L. Beverina, O.T. Hofmann, M. Sassi, R. Ruffo et al., *A high molecular weight donor for electron injection interlayers on metal electrodes*, ChemPhysChem 10 (2009), pp. 2947–2954.
[134] A. El-Sayed, P. Borghetti, E. Goiri, C. Rogero, L. Floreano, G. Lovat et al., *Understanding Energy-Level Alignment in Donor–Acceptor/Metal Interfaces from Core-Level Shifts*, ACS Nano 7 (2013), pp. 6914–6920.
[135] Z. Hu, Z. Zhong, Y. Chen, C. Sun, F. Huang, J. Peng et al., *Energy-Level Alignment at the Organic/Electrode Interface in Organic Optoelectronic Devices*, Advanced Functional Materials 26 (2016), pp. 129–136.
[136] N. Koch, *Energy levels at interfaces between metals and conjugated organic molecules*, Journal of Physics: Condensed Matter 20 (2008), pp. 184008.
[137] Y. Kim and W.B. Im, *Effect of hole-blocking layer doped with electron-transport molecules on the performance of blue organic light-emitting device*, physica status solidi (a) 201 (2004), pp. 2148–2153.
[138] J. Tardy, M.B. Khalifa and D. Vaufrey, *Organic light emitting devices with doped electron transport and hole blocking layers*, Materials Science and Engineering: C 26 (2006), pp. 196–201.
[139] Y. Xu, O.T. Hofmann, R. Schlesinger, S. Winkler, J. Frisch, J. Niederhausen et al., *Space-Charge Transfer in Hybrid Inorganic-Organic Systems*, Physical Review Letters 111 (2013), pp. 226802.
[140] D.C. Gleason-Rohrer, B.S. Brunschwing and N.S. Lewis, *Measurement of the Band Bending and Surface Dipole at Chemically Functionalized Si(111)/Vacuum Interfaces*, Journal of Physical Chemistry 117 (2013), pp. 18031–18042.
[141] J.D. Ye, S.L. Gu, S.M. Zhu, S.M. Liu, Y.D. Zheng, R. Zhang et al., *Gallium doping dependence of single-crystal n-type Zno grown by metal organic chemical vapor deposition*, Journal of Crystal Growth 283 (2005), pp. 279–285.
[142] J.D. Ye, S.L. Gu, S.M. Zhu, S.M. Liu, Y.D. Zheng, R. Zhang et al., *Fermi-level band filling and band-gap renormalization in Ga-doped ZnO*, Applied Physics Letters 86 (2005), pp. 192111.
[143] F. Zhang and A. Kahn, *Investigation of the High Electron Affinity Molecular Dopant F6-TCNNQ for Hole-Transport Materials*, Adv. Funct. Mater. 28 (2018), pp. 1703780–n/a.
[144] J.G. Lu, S. Fujita, T. Kawaharamura, H. Nishinaka, Y. Kamada, T. Ohshima et al., *Carrier concentration dependence of band gap shift in n-type ZnO:Al films*, Journal of Applied Physics 101 (2007), pp. 083705.
[145] S. Winkler, P. Amsalem, J. Frisch, M. Oehzelt, G. Heimel and N. Koch, *Probing the energy levels in hole-doped molecular semiconductors*, Mater. Horiz. 2 (2015), pp. 427–433.
[146] P.-S. Chen, T.-H. Lee, L.-W. Lai and C.-T. Lee, *Schottky mechanism for Ni/Au contact with chlorine-treated n-type GaN layer*, Journal of Applied Physics 101 (2007), pp. 024507.
[147] C.-T. Lee, C.-C. Lin, H.-Y. Lee and P.-S. Chen, *Changes in surface state density due to chlorine treatment in GaN Schottky ultraviolet photodetectors*, Journal of Applied Physics 103 (2008), pp. 094504.
[148] D. Segev and C.G.V. de Walle, *Electronic structure of nitride surfaces*, Journal of Crystal Growth 300 (2007), pp. 199–203.

[149] D. Segev and C.G.V. de Walle, *Origins of Fermi-level pinning on GaN and InN polar and nonpolar surfaces*, Europhysics Letters 76 (2006), pp. 305–311.
[150] C.G.V. de Walle and D. Segev, *Microscopic origins of surface states on nitride surfaces*, Journal of Applied Physics 101 (2007), pp. 081704.
[151] M. Himmerlich, L. Lymperakis, R. Gutt, P. Lorenz, J. Neugebauer and S. Krischok, *GaN(0001) surface states: Experimental and theoretical fingerprints to identify surface reconstructions*, Physical Review B 88 (2013), pp. 125304.
[152] B.S. Eller, J. Yang and R.J. Nemanich, *Polarization Effects of GaN and AlGaN: Polarization Bound Charge, Band Bending, and Electronic Surface States*, Journal of Electronic Materials 43 (2014), pp. 4560–4568.
[153] T.E.C. Jr., C.C. Fulton, W.J. Mecouch, R.F. Davis, G. Lucovsky and R.J. Nemanich, *Band offset measurements of the GaN (0001)/HfO_2 interface*, Journal of Applied Physics 94 (2003), pp. 7155–7158.
[154] J. Hedman and N. Martensson, *Gallium Nitride Studied by Electron Spectroscopy*, Physica Scripta 22 (1980), pp. 176.
[155] J.R. Waldrop and R.W. Grant, *Measurement of AlN/GaN (0001) heterojunction band offsets by x-ray photoemission spectroscopy*, Applied Physics Letters 68 (1996), pp. 2879–2881.
[156] A.G. Shard, *Detection limits in XPS for more than 6000 binary systems using Al and Mg Kα X-rays*, Surface and Interface Analysis 46 (2014), pp. 175–185.
[157] S.-C. Lin, C.-T. Kuo, X. Liu, L.-Y. Liang, C.-H. Cheng, C.-H. Lin et al., *Experimental Determination of Electron Affinities for InN and GaN Polar Surfaces*, Applied Physics Express 5 (2012), pp. 031003.
[158] C.I. Wu, A. Kahn, N. Taskar, D. Dorman and D. Gallagher, *GaN (0001)-(1x1) surfaces: Composition and electronic properties*, Journal of Applied Physics 83 (1998), pp. 4249–4252.
[159] C.-I. Wu, *Electronic properties of gallium nitride(0001) and aluminum nitride(0001) surfaces and interfaces*, PRINCETON UNIVERSITY, 2000.
[160] X. Crispin, V. Geskin, A. Crispin, J. Cornil, R. Lazzaroni, W.R. Salaneck et al., *Characterization of the Interface Dipole at Organic/ Metal Interfaces*, Journal of the American Chemical Society 124 (2002), pp. 8131–8141.
[161] W. Osikowicz, M.P. de Jong and W.R. Salaneck, *Formation of the Interfacial Dipole at Organic-Organic Interfaces: C_{60}/Polymer Interfaces*, Advanced Materials 19 (2007), pp. 4213–4217.
[162] F. Zu, P. Amsalem, M. Ralaiarisoa, T. Schultz, R. Schlesinger and N. Koch, *Surface State Density Determines the Energy Level Alignment at Hybrid Perovskite/Electron Acceptors Interfaces*, ACS Applied Materials & Interfaces 9 (2017), pp. 41546–41552.
[163] W. Mönch, *Semiconductor Surfaces and Interfaces*, Springer-Verlag, 1993.
[164] S. Guo, S.B. Kim, S.K. Mohapatra, Y. Qi, T. Sajoto, A. Kahn et al., *n-Doping of Organic Electronic Materials using Air-Stable Organometallics*, Advanced Materials 24 (2012), pp. 699–703.
[165] A.J. Giordano, F. Pulvirenti, T.M. Khan, C. Fuentes-Hernandez, K. Moudgil, J.H. Delcamp et al., *Organometallic Dimers: Application to Work-Function Reduction of Conducting Oxides*, ACS Applied Materials & Interfaces 7 (2015), pp. 4320–4326.
[166] M. Castellani, S. Winkler, B. Bröker, M. Baumgarten, K. Müllen and N. Koch, *Work Function Increase of transparent conductive electrodes by solution processed electron acceptor molecular monolayers*, Applied Physics A 114 (2014), pp. 291–295.
[167] I. Bartos, O. Romanyuk, J. Houdkova, P.P. Paskov, T. Paskova and P. Jiricek, *Electron band bending of polar, semipolar and non-polar GaN surfaces*, Journal of Applied Physics 119 (2016), pp. 105303.
[168] W. Gao and A. Kahn, *Electrical doping: the impact on interfaces of pi-conjugated molecular films*, Journal of Physics: Condensed Matter 15 (2003), pp. S2757.
[169] S. Das, M. Kim, J. Lee and W. Choi, *Synthesis, Properties, and Applications of 2-D Materials: A Comprehensive Review*, Critical Reviews in Solid State and Materials Sciences 39 (2014), pp. 231–252.

[170] Q.H. Wang, K. Kalantar-Zadeh, A. Kis, J.N. Coleman and M.S. Strano, *Electronics and optoelectronics of two-dimensional transition metal dichalcogenides*, Nature Nanotechnology 7 (2012), pp. 699.

[171] S. Manzeli, D. Ovchinnikov, D. Pasquier, O.V. Yazyev and A. Kis, *2D transition metal dichalcogenides*, Nature Reviews Materials 2 (2017), pp. 17033.

[172] Y. Ye, J. Xiao, H. Wang, Z. Ye, H. Zhu, M. Zhao et al., *Electrical generation and control of the valley carriers in a monolayer transition metal dichalcogenide*, Nature Nanotechnology 11 (2016), pp. 598–602.

[173] M.-H. Chiu, M.-Y. Li, W. Zhang, W.-T. Hsu, W.-H. Chang, M. Terrones et al., *Spectroscopic Signatures for Interlayer Coupling in MoS_2-WSe_2 van der Waals Stacking*, ACS Nano 8 (2014), pp. 9649–9656.

[174] Y.-C. Lin, C.-Y.S. Chang, R.K. Ghosh, J. Li, H. Zhu, R. Addou et al., *Atomically Thin Heterostructures Based on Single-Layer Tungsten Diselenide and Graphene*, Nano Letters 14 (2014), pp. 6936–6941.

[175] J. Fraxedas, S. García-Gil, S. Monturet, N. Lorente, I. Fernández-Torrente, K.J. Franke et al., *Modulation of Surface Charge Transfer through Competing Long-Range Repulsive versus Short-Range Attractive Interactions*, The Journal of Physical Chemistry C 115 (2011), pp. 18640–18648.

[176] C. Stadler, S. Hansen, I. Kroger, C. Kumpf and E. Umbach, *Tuning intermolecular interaction in long-range-ordered submonolayer organic films*, Nat Phys 5 (2009), pp. 153–158.

[177] A. Raja, A. Chaves, J. Yu, G. Arefe, H.M. Hill, A.F. Rigosi et al., *Coulomb engineering of the bandgap and excitons in two-dimensional materials*, Nature Communications 8 (2017), pp. 15251.

[178] R. Resta, *Thomas-Fermi dielectric screening in semiconductors*, Phys. Rev. B 16 (1977), pp. 2717–2722.

[179] S. Park, N. Mutz, T. Schultz, S. Blumstengel, A. Han, A. Aljarb et al., *Direct determination of monolayer MoS_2 and WSe_2 exciton binding energies on insulating and metallic substrates*, 2D Materials 5 (2018), pp. 025003.

[180] D. Le, A. Barinov, E. Preciado, M. Isarraraz, I. Tanabe, T. Komesu et al., *Spin-orbit coupling in the band structure of monolayer WSe2*, Journal of Physics: Condensed Matter 27 (2015), pp. 182201.

[181] Y. Smets, C.B. Stark, S. Lach, F. Schmitt, C.A. Wright, M. Wanke et al., *Charge-induced distortion and stabilization of surface transfer doped porphyrin films*, The Journal of Chemical Physics 139 (2013), pp. 044703.

[182] H.J. Weber and G.B. Arfken, *Essential Mathematical Methods for Physicists*, Academic Press, 2003.

Appendix

A) Derivation of the Potential Above a Bilinear Array

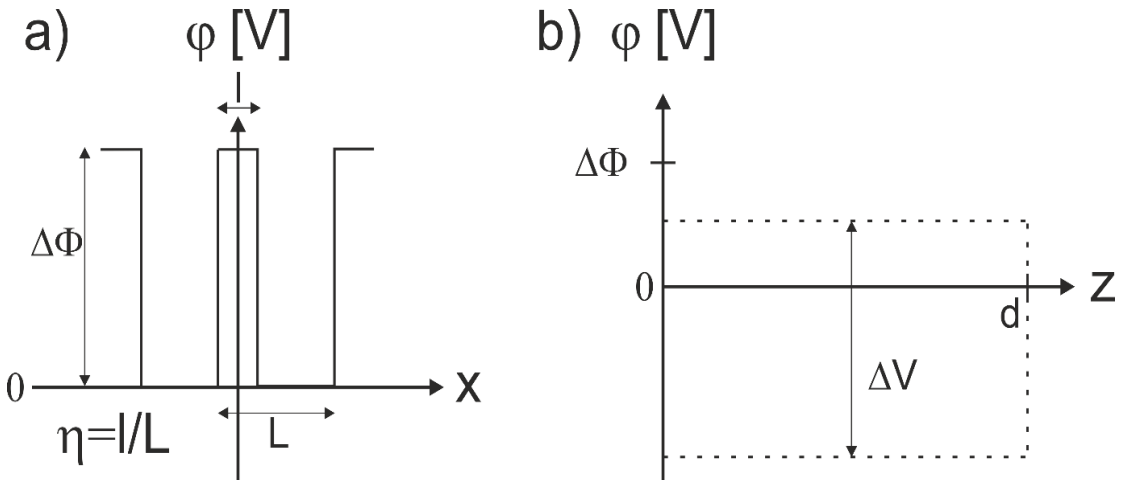

Fig. 1: Boundary conditions used for calculating the electrostatic potential φ(x,z). a) Potential at the surface of the sample (z=0). The stripes have a potential difference of ΔΦ and a periodicity of L. The area ratio η is given by l/L. b) The second boundary condition is given by the applied voltage ΔV between sample (z=0) and analyzer (z=d).

Derivation of equation (49)

The potential $\varphi(x,z)$ needs to fulfill the Laplace-equation

$$\Delta\varphi(x,z) = 0$$

with the boundary conditions

$$\lim_{z\to\infty} \frac{\partial\varphi(x,z)}{\partial z} = 0,$$

$$\varphi(x,0) = f(x) = f(x+L) = \text{pulse}_{L,\eta,\Delta\Phi}(x),$$

where $\text{pulse}_{L,\eta,\Delta\Phi}(x)$ is defined as

$$\text{pulse}_{L,\eta,\Delta\Phi}(x) = \begin{cases} \Delta\Phi, |x| \leq \frac{\eta}{2} \\ 0, |x| > \frac{\eta}{2} \end{cases}$$

L is the periodicity of the stripes, η is the area ratio of the FSH and ΔΦ ist he work function difference between the two SAMs. An illustration of the individual

parameters is given in Fig. 1 a). To solve the Laplace-equation the method of "separation of variables" is applied, where $\varphi(x,z)$ is assumed to be a product of two functions which are only dependent on one variable each:

$$\varphi(x,z) = X(x) \cdot Z(z)$$

$$\Delta\varphi(x,z) = X''Z + Z''X = 0$$

$$\frac{X''}{X} = -\frac{Z''}{Z}$$

X'' and Z'' denote the second derivative, respectively. Since the left side of the equation above depends only on x and the right side only on z, it follows

$$\frac{X''}{X} = -\frac{Z''}{Z} = -k^2.$$

This yields the two differential equations

$$X'' + k^2X = 0,$$

$$Z'' - k^2Z = 0$$

with solutions of the form

$$X = A\sin(kx) + B\cos(kx),$$

$$Z = Ce^{kz} + De^{-kz}.$$

The first boundary condition yields

$$\lim_{z\to\infty} \frac{\partial\varphi(x,z)}{\partial z} = \lim_{z\to\infty} Z' = \lim_{z\to\infty} (Cke^{kz} + Dke^{-kz}) = 0,$$

$$C = 0,$$

$$Z = De^{-kz}.$$

The periodicity of the boundary condition $f(x) = f(x+L)$ yields

$$k = \frac{2\pi n}{L}, n = 0,1,2 \ldots$$

With this the solution of $\varphi(x,z)$ is given by a superposition of all possible solutions for X and Z in the following way:

$$\varphi(x,z) = B_0 + \sum_{n=1}^{\infty} A_n \sin\left(2\pi n\frac{x}{L}\right) e^{-2\pi n\frac{z}{L}} + B_n \cos\left(2\pi n\frac{x}{L}\right) e^{-2\pi n\frac{z}{L}}.$$

The boundary condition $\varphi(x,0) = f(x)$ yields

$$\varphi(x,0) = B_0 + \sum_{n=1}^{\infty} A_n \sin\left(2\pi n\frac{x}{L}\right) + B_n \cos\left(2\pi n\frac{x}{L}\right) = f(x).$$

This can only be fulfilled if the coefficients A_n and B_n are equal to the Fourier coefficients of the Fourier expansion of $f(x)$, which is well known and given by [182]

$$f(x) = \Delta\Phi\eta + \sum_{n=1}^{\infty} \frac{2\Delta\Phi}{n\pi} \sin(n\pi\eta) \cos\left(2\pi n\frac{x}{L}\right).$$

Comparing both equations yields

$$B_0 = \Delta\Phi\eta,$$

$$A_n = 0,$$

$$B_n = \frac{2\Delta\Phi}{n\pi} \sin(n\pi\eta).$$

This finally results in equation (49):

$$\varphi(x,z) = \Delta\Phi\eta + \sum_{n=1}^{\infty} \frac{2\Delta\Phi}{n\pi} \cdot \sin(n\pi\eta) \cdot \cos\left(2\pi n\frac{x}{L}\right) \cdot e^{-2\pi n\frac{z}{L}}.$$

Derivation of equation (51)

Here the boundary condition $\lim_{z\to\infty} \frac{\partial\varphi(x,z)}{\partial z} = 0$ is changed to $\varphi(x,d) = \Delta V$. ΔV is the applied bias between the sample and the detector at distance d. With this the general solution for $\varphi(x,z)$ becomes

$$\varphi_g(x,z) = \Delta\Phi\eta + \sum_{n=1}^{\infty} \frac{2\Delta\Phi}{n\pi} \cdot \sin(n\pi\eta) \cdot \cos\left(2\pi n\frac{x}{L}\right) \cdot \left(C_n e^{-2\pi n\frac{z}{L}} + D_n e^{2\pi n\frac{z}{L}}\right).$$

Now applying the boundary condition $\varphi(x,d) = \Delta V$ yields

$$\varphi_g(x,d) = \Delta V = \Delta\Phi\eta + \sum_{n=1}^{\infty} \frac{2\Delta\Phi}{n\pi} \cdot \sin(n\pi\eta) \cdot \cos\left(2\pi n\frac{x}{L}\right) \cdot \left(C_n e^{-2\pi n\frac{d}{L}} + D_n e^{2\pi n\frac{d}{L}}\right).$$

As ΔV is constant, this further implies that the derivative with respect to x becomes zero at $z = d$:

$$\left.\frac{\partial \varphi}{\partial x}\right|_{z=d} = 0 = \sum_{n=1}^{\infty} -\frac{4\Delta\Phi}{L} \cdot \sin(n\pi\eta) \cdot \sin\left(2\pi n \frac{x}{L}\right) \cdot \left(C_n e^{-2\pi n \frac{d}{L}} + D_n e^{2\pi n \frac{d}{L}}\right).$$

Since this has to hold for all x it means that:

$$C_n e^{-2\pi n \frac{d}{L}} + D_n e^{2\pi n \frac{d}{L}} = 0,$$

$$C_n = -D_n e^{4\pi n \frac{d}{L}}.$$

Inserting this back into the general solution yields

$$\varphi_g(x,z) = \Delta\Phi\eta + \sum_{n=1}^{\infty} \frac{2\Delta\Phi}{n\pi} \cdot \sin(n\pi\eta) \cdot \cos\left(2\pi n \frac{x}{L}\right) \cdot \left(D_n e^{2\pi n \frac{z}{L}} - D_n e^{4\pi n \frac{d}{L}} e^{-2\pi n \frac{z}{L}}\right).$$

Factoring out $2e^{2\pi n \frac{d}{L}}$ results in

$$\varphi_g(x,z) = \Delta\Phi\eta + \sum_{n=1}^{\infty} \frac{2\Delta\Phi}{n\pi} \cdot \sin(n\pi\eta) \cdot \cos\left(2\pi n \frac{x}{L}\right) \cdot 2D_n e^{2\pi n \frac{d}{L}} \left(\frac{e^{2\pi n \frac{(z-d)}{L}} - e^{-2\pi n \frac{(z-d)}{L}}}{2}\right),$$

$$\varphi_g(x,z) = \Delta\Phi\eta + \sum_{n=1}^{\infty} \frac{2\Delta\Phi}{n\pi} \cdot \sin(n\pi\eta) \cdot \cos\left(2\pi n \frac{x}{L}\right) \cdot 2D_n e^{2\pi n \frac{d}{L}} \sinh\left(2\pi n \frac{(z-d)}{L}\right).$$

Applying again the boundary condition $\varphi(x,0) = f(x)$ and comparing it to the Fourier expansion of $f(x)$ yields

$$\varphi_g(x,0) = \Delta\Phi\eta + \sum_{n=1}^{\infty} \frac{2\Delta\Phi}{n\pi} \cdot \sin(n\pi\eta) \cdot \cos\left(2\pi n \frac{x}{L}\right) \cdot 2D_n e^{2\pi n \frac{d}{L}} \sinh\left(-2\pi n \frac{d}{L}\right),$$

$$1 = 2D_n e^{2\pi n \frac{d}{L}} \sinh\left(-2\pi n \frac{d}{L}\right)$$

$$D_n = \frac{e^{-2\pi n\frac{d}{L}}}{2\sinh\left(-2\pi n\frac{d}{L}\right)}.$$

So the general solution of $\varphi(x,z)$ is in this case given by

$$\varphi_g(x,z) = \Delta\Phi\eta + \sum_{n=1}^{\infty}\frac{2\Delta\Phi}{n\pi}\cdot\sin(n\pi\eta)\cdot\cos\left(2\pi n\frac{x}{L}\right)\cdot\frac{\sinh\left(2\pi n\frac{(z-d)}{L}\right)}{\sinh\left(2\pi n\frac{d}{L}\right)}.$$

To obtain the complete solution for the potential with the given boundary conditions, one needs beside the general solution also a particular solution φ_p that fulfils both $\varphi(x,d) = \Delta V$ and $\Delta\varphi(x,z)=0$. One such particular solution is e.g. given by

$$\varphi_p(x,z) = \alpha\cdot z.$$

Inserting this into the general solution and considering the boundary condition $\varphi(x,d) = \Delta V$ one obtains

$$\varphi_p(x,d) = \alpha\cdot d = \Delta V,$$

$$\alpha = \frac{\Delta V}{d}.$$

The solution to this boundary condition problem is finally given by the sum of the general solution $\varphi_g(x,z)$ and the particular solution $\varphi_p(x,z)$ and yields equation (51):

$$\varphi(x,z) = \varphi_g + \varphi_p$$

$$= \Delta\Phi\eta + \frac{\Delta V}{d}z + \sum_{n=1}^{\infty}\frac{2\Delta\Phi}{n\pi}\cdot\sin(n\pi\eta)\cdot\cos\left(2\pi n\frac{x}{L}\right)\cdot\frac{\sinh\left(2\pi n\frac{(z-d)}{L}\right)}{\sinh\left(2\pi n\frac{d}{L}\right)}.$$

B) Additional XPS and UPS Data

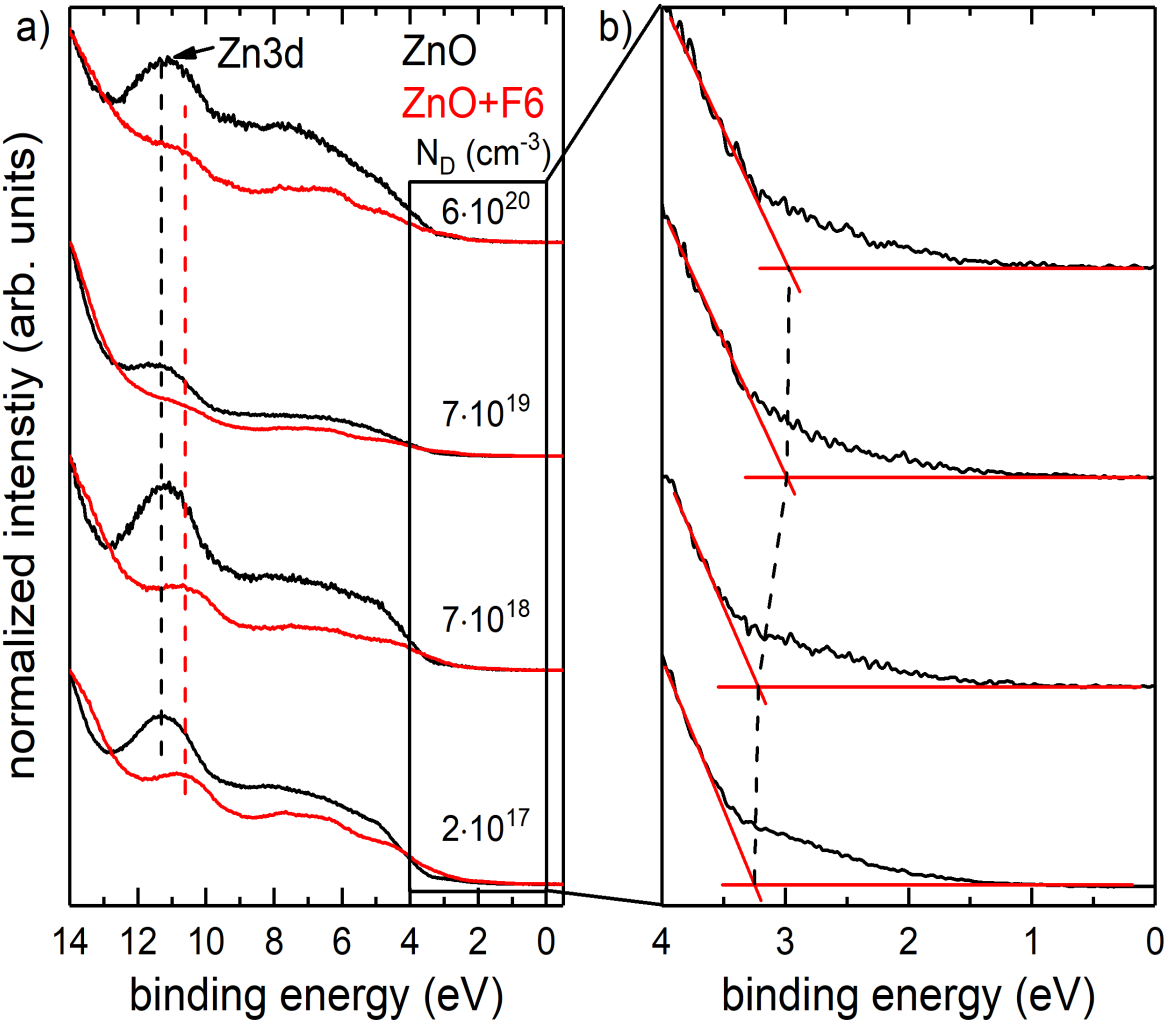

Fig. 2: a) Valence band spectra of differently doped ZnO ($000\bar{1}$) before (black) and after (red) deposition of 10 nm F6-TCNNQ. The Zn3d core level and its shift are indicated by dashed lines. b) Zoom into the region near the ZnO valence band, showing a shift of the ZnO VBM to lower binding energy for high doping concentrations, indicating an increased upward band bending already before F6-TCNNQ deposition.

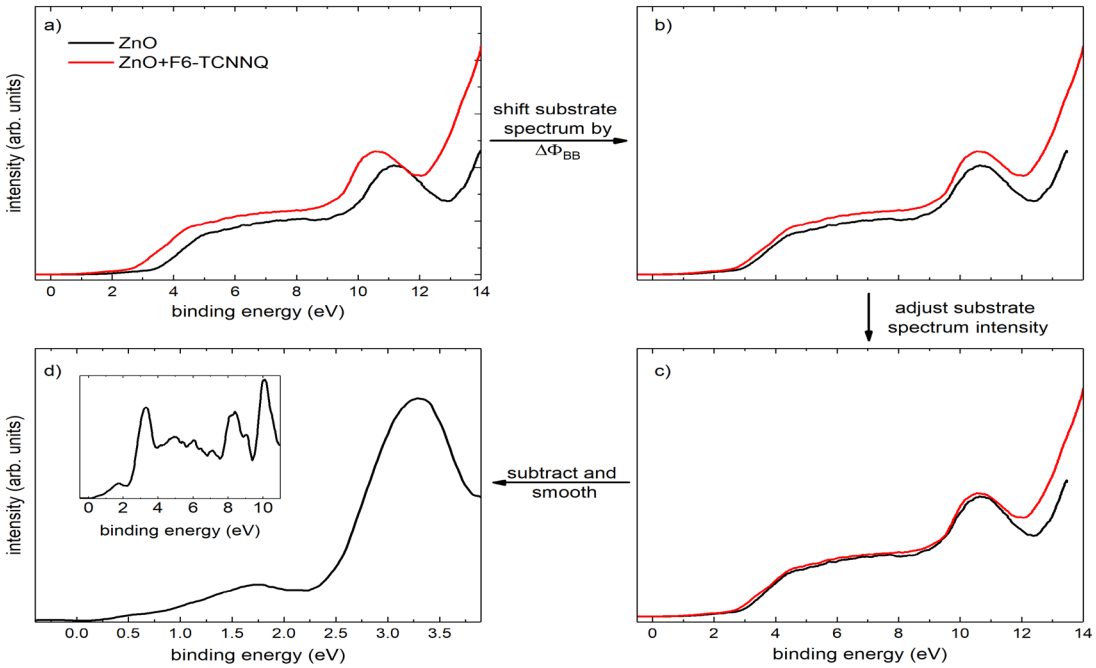

Fig. 3: Procedure to extract the F6-TCNNQ signal from the measured UPS data of a nominal monolayer of F6-TCNNQ on ZnO(000-1). a) Pristine spectra, it can be seen that the signal from F6-TCNNQ cannot be resolved directly. b) In the first step the substrate reference spectrum is shifted by the amount of band bending determined from the shift of the $Zn2p_{3/2}$ core level. c) Afterwards the intensity is adjusted, this step introduces some uncertainty, which hinders a quantitative analysis of the F6-TCCNQ contributions. d) Subtraction of the substrate reference spectrum from the UPS spectrum of F6-TCCNQ on ZnO and subsequent smoothing. The inset shows a large range spectrum of the obtained F6-TCNNQ contribution.

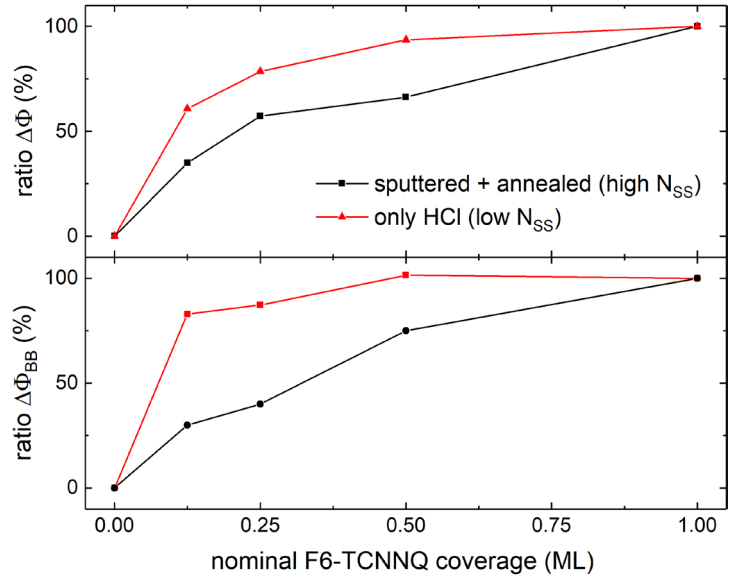

Fig. 4: Changes in work function $\Delta\Phi$ and band bending $\Delta\Phi_{BB}$ of differently prepared GaN (0001) as a function of nominal F6-TCNNQ coverage. The values are normalized with respect to the maximum change. The faster increase of the work function of only HCl treated samples due to the fast initial increase in upward band bending after coverage of only 1/8 of a monolayer is clearly seen in this representation.

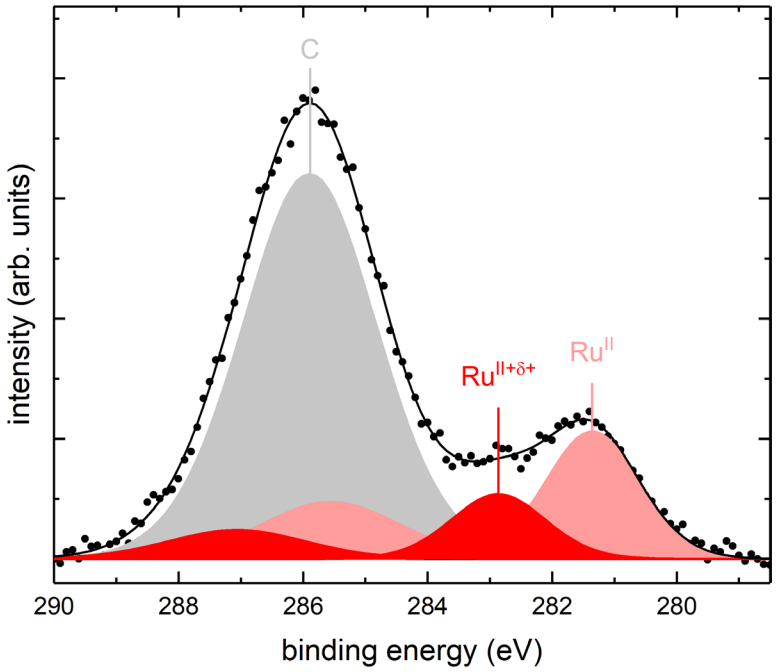

Fig. 5: XPS data of nominally 5 Å $[RuCp^*(mes)]_2$ deposited on undoped GaN (0001), after background subtraction. The spectrum was fitted with a C1s component (gray) and two Ru3d doublets (red and pink). The photoelectrons originating from the cationic $[RuCp^*(mes)]^+$ species $Ru^{II+\delta+}$ are less screened and therefore have higher binding energies compared to the neutral species.

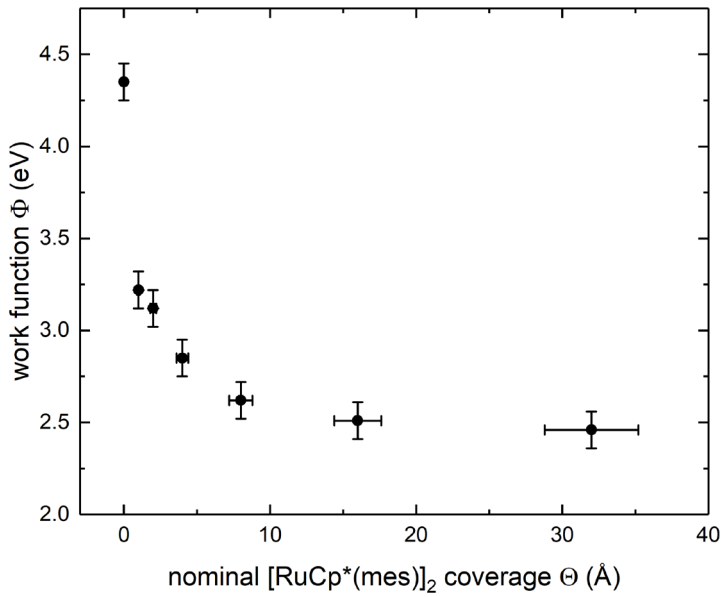

Fig. 6: Work function as a function of coverage for $[RuCp^*(mes)]_2$ on Si:H (111). A work function reduction down to 2.5 eV is achieved for ca. 1 nm coverage.

C) Additional STS Spectra for the Determination of L_{TF}

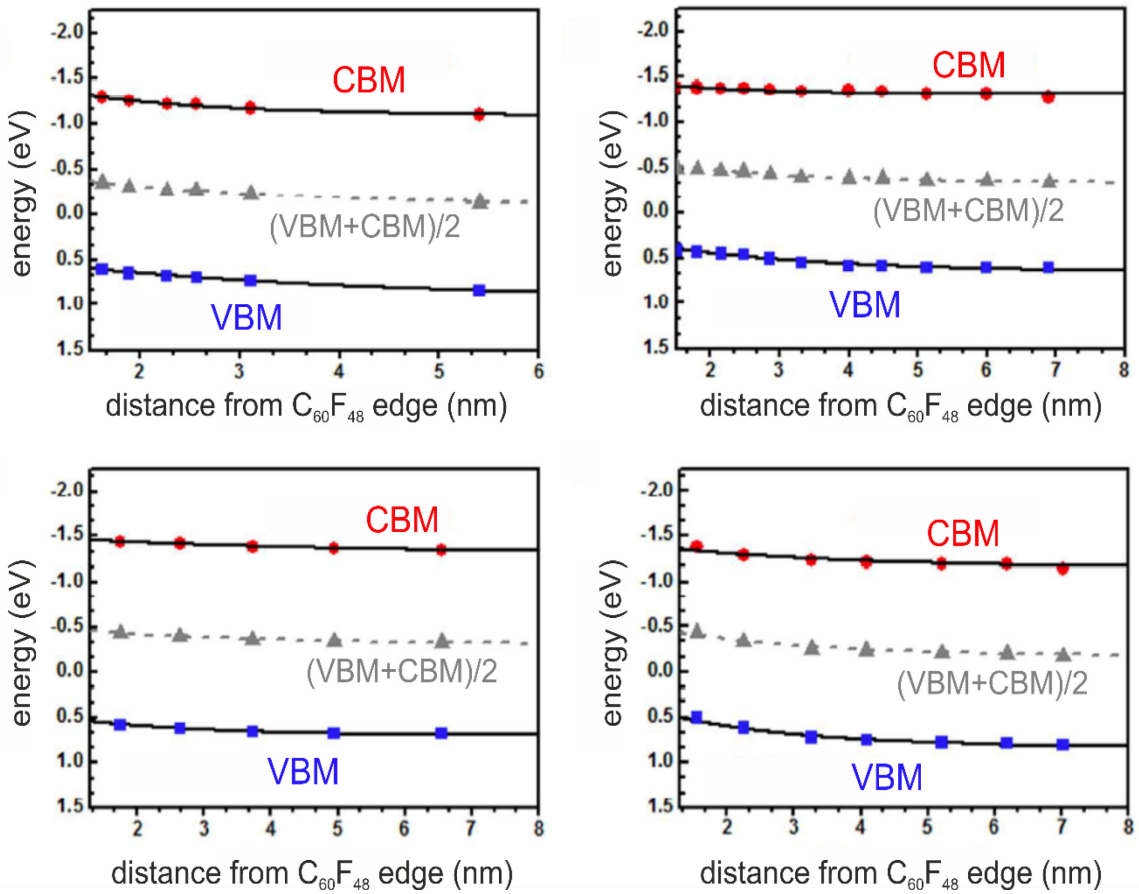

Fig. 7: VBM, CBM and (VBM+CBM)/2 of WSe_2, as obtained from STS measurements, at four different points at a transition region between p-doped WSe_2 ($C_{60}F_{48}$ covered) and intrinsic WSe_2. The fits are according to Thomas-Fermi theory $\Delta U \sim e^{-d/L_{\mathrm{TF}}}$ and yield a Thomas-Fermi length of $L_{\mathrm{TF}} = 2.3 \pm 0.7$ nm. Adapted from [105].

List of Publications

- **T.Schultz**, R. Schlesinger, J. Niederhausen, F. Henneberger, S. Sadovef, S. Blumstengel, A. Vollmer, F. Bussolotti, J.-P. Yang, S. Kera, K. Parvez, N. Ueno, K. Müllen and N. Koch, *„Tuning the work function of GaN with organic molecular acceptors“*, Phys. Rev. B **93**, 125309 (2016)
- **T. Schultz**, R. Schlesinger and N. Koch, „*Energy level tuning at inorganic/organic semiconductor heterojunctions*", Proc. SPIE **9923,** 99230E (2016)
- **T. Schultz**, T. Lenz, N. Kotadiya, G. Heimel, G. Glasser, R. Berger, P. W. M. Blom, P. Amsalem, D. M. de Leeuw and N. Koch, "*Reliable Work Function Determination of Multicomponent Surfaces and Interfaces: The Role of Electrostatic Potentials in Ultraviolet Photoelectron Spectroscopy*", Adv. Mater. Interfaces **4**, 1700324 (2017)
- **T. Schultz**, Z. Song, Z. Ding, B. Lei, C. Han, P. Amsalem, T. Lin, D. Chi, S.L. Wong, Y.J. Zheng, M.-Y. Li, L.-J. Li , W. Chen, N. Koch, Y. L. Huang and A. Thye Shen Wee, "*Electronic properties of a 1D intrinsic/p-doped heterojunction in a 2D transition metal dichalcogenide semiconductor*", ACS Nano **11**, 9128–9135 (2017)
- F. Zu, P. Amsalem, M. Ralaiarisoa, **T. Schultz**, R. Schlesinger, and N. Koch, *"Surface State Density Determines the Energy Level Alignment at Hybrid Perovskite / Electron Acceptors Interfaces"*, ACS Applied Materials & Interfaces **9**, 41546 (2017)
- S. Park, N. Mutz, **T. Schultz**, S. Blumstengel, A. Han, A. Aljarb, L.-J. Li, E. J. W. List-Kratochvil, P. Amsalem and N. Koch, *„Direct determination of monolayer MoS_2 and WSe_2 exciton binding energies on insulating and metallic substrates"*, 2D materials **5**, 025003 (2018)
- **T. Schultz**, S. Vogt, P. Schlupp, H. von Wenckstern, N. Koch, M. Grundmann, „*Influence of oxygen deficiency on the rectifying behavior of transparent-semiconducting-oxide–metal interfaces*", Phys. Rev. Applied **9,** 064001 (2018)
- **T. Schultz**, J. Niederhausen, R. Schlesinger, S. Sadofev and N. Koch, *„Impact of surface states and bulk doping level on hybrid inorganic/organic semiconductor interface energy levels"*, JAP **123**, 245501 (2018)
- A. Kyndiah, A. Ablat, S. Guyot-Reeb, **T. Schultz**, F. Zu, N. Koch, P. Amsalem, S. Chiodini, T. Y. Alic, Y. Topal, M. Kus, L. Hirsch, S. Fasquel, M. Abbas, "*A Multifunctional Interlayer for Solution Processed High Performance Indium Oxide Transistors*", scientific reports **8**, 10946 (2018)
- **T. Schultz**, X. Xu, Z. Qin, N. Severin, B. Haas, S. Shen, J. N. Kirchhof, A. Opitz, C. T. Koch, K. Bolotin, J. P. Rabe, G. Eda, N. Koch, „*Microstructure and Elastic Constants of Transition Metal Dichalcgenide Monolayers from Friction and Shear Force Microscopy*", Advanced Materials (2018)

Acknowledgments

First of all I would like to thank Prof. Koch for giving me the chance to do my dissertation in his group, for financial support through the IMPRS and the SFB951 and for fruitful discussions both scientifically and personally.

I'd like to thank all my colleagues for support on a daily basis.

Zhibo Song, Yu Li Huang, Zijing Ding and Prof. Andrew Wee supported me during the "TMDC/Organic interface" project, both professionally and also personally during my stays in Singapore.

I would also like to thank my parents and grandparents, for raising me and always supporting me.

Finally I would like to thank my girlfriend Theres, who always supported me during my thesis, pushed me when necessary and made this whole time a lot more fun.

Selbstständigkeitserklärung

Ich erkläre, dass ich die Dissertation selbständig und nur unter Verwendung der von mir gemäß § 7 Abs. 3 der Promotionsordnung der Mathematisch-Naturwissenschaftlichen Fakultät, veröffentlicht im Amtlichen Mitteilungsblatt der Humboldt-Universität zu Berlin Nr. 126/2014 am 18.11.2014, angegebenen Hilfsmittel angefertigt habe. Darüber hinaus versichere ich, mich nicht anderwärts um einen Doktorgrad beworben zu haben, oder einen entsprechenden Doktorgrad zu besitzen. Die dem Verfahren zu Grunde liegende Promotionsordnung der Mathematisch-Naturwissenschaftlichen Fakultät der Humboldt-Universität zu Berlin vom 18.11.2014 habe ich zur Kenntnis genommen.

Thorsten Schultz

Berlin, 01.09.2018